DISSERTATION

Searching for exoplanetary rings via transit photometry: methodology and its application to the Kepler data

:

Masataka Aizawa

A thesis submitted to
the graduate school of science,
the University of Tokyo
in partial fulfillment of
the requirements for the degree
of
Master of Science in Physics

January, 2017

Abstract

Since the first discovery of the exoplanet 51 Pegasi b in 1995, over 3500 exoplanets have been reported. Now, we know that planets are common outside the Solar System.

Similarly, we naturally expect that planetary rings are also common outside the Solar System. Their observational properties would also give a significant implication of the planetary physics. However, in spite of its importance, there has been only one research, which conducts a survey of exoplanetary rings. They could not find any evidence of rings, but more systematic surveys can achieve the first detection of planetary rings.

In this thesis, we discuss methods to detect rings, determine suitable targets for a ring search, and present our methodology and its application to the data.

First, we disucss the suitable method to find rings. Among several techniques in detecting exoplanets, the most effective method to detect rings is a *transit method*, which probes a planet via a photometrical observation of a stellar occultation. Fortunately, the transit method is not only the most sensitive to rings but also yields the largest number of the detection of the exoplanets. Especially, the *Kepler* spacecraft launched by NASA in 2009 conducted a 4-year observation of about 150,000 stars, and it have detected over 2300 planets until now. These plentiful data can yield the detection of planetary rings.

Second, we determine the suitable targets for a ring search. The most possible candidates, which harbor the detectable rings, are *long-period* planets. This is because around the long-period planets, the rings are unlikely to suffer from a strong stellar tide and radiation. Although the best targets for a ring search are long-period planets, their transit probability is very low, and there are only 37 planets, whose temperature is less than 200 K, in the official *Kepler* catalog. To increase the number of long-period planets, we also search for unreported long-period planets in the *Kepler* by ourselves, and we find 14 new planet candidates from the *Kepler* data. In addition to these planets, there are other planets reported by different groups, and, in total, 89 long-period planets remain.

Finally, we present our methodology of a systematic search for exoplanetary rings via transit photometry of long-period planets. The methodology relies on a precise integration scheme we develop to compute a transit light curve of a ringed planet. We apply the methodology to 89 long-period planet candidates from the *Kepler* data so as to estimate, and/or set upper limits on, the parameters of possible rings. While a majority of our samples do not have a sufficiently good signal-to-noise ratio for meaningful constraints on ring parameters, we find that six systems with a higher signal-to-noise ratio are inconsistent with the presence of a ring larger than 1.5 times the planetary radius assuming a grazing orbit and a tilted ring. Furthermore, we identify five preliminary candidate systems whose light curves exhibit ring-like features.

After removing four false positives due to the contamination from nearby stars, we identify KIC 10403228 as a tentative candidate of a ringed planet.

To characterize this tentative ringed planet, we first analyze it assuming that the transit is caused by a planetary transit. A systematic parameter fit of light curve of KIC 10403228 indicates two possible solutions with an orbital period $P = 450$ years; one implies a planet of radius $0.88R_J$ with a ring of $0.89R_J < R < 2.56R_J$ tilted by 59.4° with respect to the orbital plane, while the other implies a planet of radius $1.44R_J$ with a ring of $2.29R_J < R < 3.69R_J$ tilted by 12.3°. We also examine various possibilities other than the ring hypothesis on the assumption of the planetary transit, and we found the scenarios without the ring are unlikely to explain the data.

In the above, we assume that the transit is due to the planet. However, the transit might be caused by a circumstellar disk in the binary rather than the planetary ring. Hence, we compare the plausibilities of the eclipsing-binary scenario and planet scenario using the public code "VESPA". As a result, we find that we cannot exclude one of two in the sense that there still remain significant uncertainties in likelihoods and priors of both models. For the decisive confirmation of the system, a follow-up observation will be effective.

Although we find a tentative candidate of a ringed planet, we are still very far from answering "How common are planetary rings". Toward this goal, we plan to improve our methodology and conduct a thorough systematic search for exoplanetary rings in the future.

Contents

Chapter 1

Introduction

"Are planetary systems common in the world?". This fundamental question for the human beings had not been empirically tackled until 1995, when the first detected exoplanet around 51 Pegasi is reported (Mayor & Queloz 1995). Since the discovery of 51 Pegasi b, the number of the detected exoplanets has increased year by year as shown in Figure 1.1. As seen in the plot, almost all of planets are detected by *transit* method and *radial velocity* technique. The former *photometrically* observes periodic dimming of stars due to the occultation by planets.

In Figure 1.1. there is a clear increase in the number of transiting planets in the past several years. This is mainly due to the advent of the Kepler spacecraft launched by NASA in 2009 (Borucki et al. 2010). This game changer "Kepler" monitored over 100,000 stars for four years, and it has detected over 2300 confirmed planets and over 4600 planetary candidates called KOI until December 2016. Figure 1.2 shows the period-radius plot of these Kepler planets. One of prominent findings by Kepler is the detection of tremendous numbers of rocky planets as well as the potentially habitable planets (HZ) as seen in Figure 1.2. In total, it detected 21 potentially habitable confirmed planets whose sizes are less than twice Earth-size, and contributes to the estimation of the frequency of HZ terrestrial planets $\eta_\oplus$(e.g Catanzarite & Shao 2011),

In addition to the large amount of detections of planets, Kepler has also discovered interesting individual planets. The findings include the Kepler planets with their mass being revealed by TTV (Transit Timing Variations) (Holman et al. 2010), the non-transiting planetary systems revealed by TTV (Ballard et al. 2011; Nesvorný et al. 2012), the most compact planetary system (Lissauer et al. 2011), the first detected circumbinary planet (Doyle et al. 2011), the multi-planet Kepler-47 system (Orosz et al. 2012), and the first confirmed Earth-like habitable planet (Quintana et al. 2014). It also detected the unprecedented objects including the disintegrating Mercury-sized planet KIC 12557548b (Rappaport et al. 2012), KIC 8462852 that shows the extremely peculiar light variations with unknown origins (Boyajian et al. 2016), and KIC 2856960, whose light curves are hard to explain.

In this way, Kepler has largely contributed to the planetary science, and, now, we have no doubt that planets are common outside the Solar System. However, in spite of the success in detection of exoplanets, there is no report on exomoons and exoplanetary
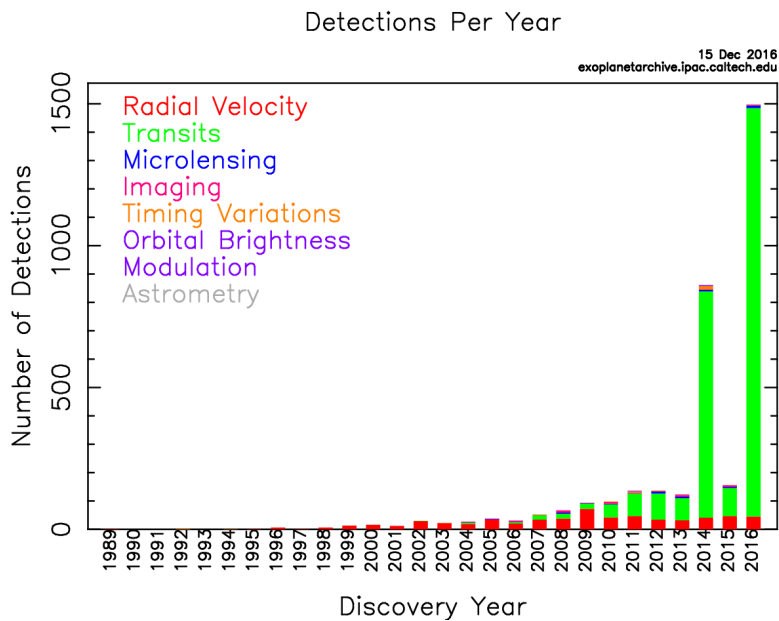
Figure 1.1: Number of exoplanets detected by several techniques until 2016. The plot is taken from http://exoplanetarchive.ipac.caltech.edu/exoplanetplots/.
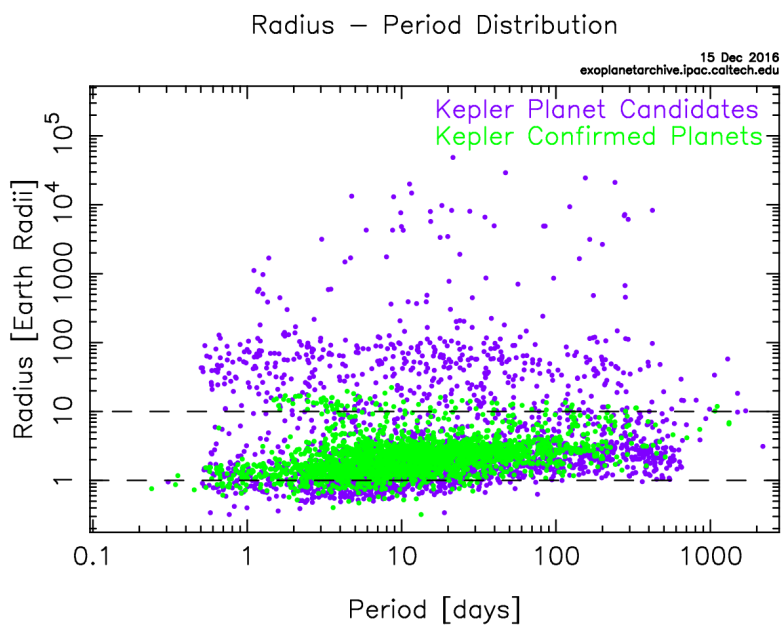
Figure 1.2: Radius-period plots of planets detected by Kepler. The plot is taken from http://exoplanetarchive.ipac.caltech.edu/exoplanetplots/.

rings, which are naturally expected to be common outside the Solar System. Thus, in the planetary science, the next big question to be solved is "Are planetary moons and rings common in the world?".

The searches for exomoons have been conducted by several groups, but none of them led to the decisive detection. The most systematic survey for exomoons is conducted in the project named "Hunt for Exomoons with Kepler (HEK)". They developed a unique methodology to search for the exomoons, and applied it to the Kepler data with their photo-dynamical codes for exomoons. Although HEK has published five related papers (Kipping et al. 2012, 2013a,b, 2014, 2015b) they have not found any sign of an exomoon. In the different context, Cabrera et al. (2013) discovered a possible signature of the exomoon around Kepler-90f, but it turned out to be false positive from the detailed pixel analysis (Kipping et al. 2015a). From another point of view, Heller (2014) found that the averaged feature of the exomoon in the phase folded data can also imply the exomoons. Using this method, Hippke (2015) superstacked light curves of 177 planets with periods 35 days $< P <$ 80 days, and they found a significant feature, which can be interpreted by the averaged feature of exomoons. This is not the decisive detection of exmoons, but this result greatly encourages the further search for exomoons. In summary, the methodologies to find exomoons are well investigated, and there are several applications of them to the data.

On the other hand, there has been only one systematic survey for exoplanetary rings (Heising et al. 2015). They conducted the search around the 21 short-period and hot planets (mostly with $P < 10$ days), but they could not find any evidence of rings. Indeed, their results are consistent with a simple expectation that detectable rings are not frequent around such short-period planets. At the current situation, the long-period planets, which can harbor detectable rings, are not investigated, and there remains much possibility that the Kepler has an unrevealed evidence of rings.

The plan of this is as follows. First, we introduce some necessary basics related to the tranist method and confirm our knowledge about the observed planetary rings. Then, we discuss methods to detect rings and determine suitable planets for a ring search. Finally, we explain our methodology to search for rings and apply it to the Kepler data.

In Chapter 2 and 3, we give a brief summary of Keplerian motion and the transit photometry, which will be the basis throughout the current thesis. In Chapter 4, we review (possible) planetary rings found in and outside the Solar System. In Chapter 5, we introduce several techniques to detect exoplanets, and consider the expected signals from rings. In Chapter 6, we discuss the stability and obliquity of planetary rings to determine the targets for the search for rings. In Chapter 7 and Appendix, we describe our methodology to search for rings, and applies it to the data of *long-period* planets revealed by Kepler. Finally, in Chapter 8, we summarize our findings and researches, and give the future prospects for the search for exoplanetary rings.

Chapter 2

Keplerian motion

In planetary systems, the stellar gravity is dominant. In such a case, each of the planetary orbits is well approximated by a two-body orbit composed of the planet and the star. If we assume two point masses, their orbits can be solved analytically, and the solution is called the Keplerian orbit. The Keplerian orbit describes precisely the (exo-)planetary motion, so it is a basis of the field of exo-planetary sciences. In this section, we derive the expression of the Keplerian orbit, give a relation between the Keplerian motion and time, and define an orbital plane in three-dimensional space. This section basically follows Murray & Correia (2010).

2.1 Derivation of Kepler motion

Let us consider the motions of two point masses m_1 and m_2 with being positioned at $\boldsymbol{r_1}$ and $\boldsymbol{r_2}$. We only consider the inverse square force, which arises from gravity between two bodies. When the gravitational force acts on the two masses, the equations of motion are

$$\boldsymbol{F_1} = G\frac{m_1 m_2}{r^3}\boldsymbol{r} = m_1\ddot{\boldsymbol{r}}_{\boldsymbol{1}}, \qquad \boldsymbol{F_2} = -G\frac{m_1 m_2}{r^3}\boldsymbol{r} = m_2\ddot{\boldsymbol{r}}_{\boldsymbol{2}}, \tag{2.1}$$

where $G = 6.67260 \times 10^{-11} \text{N m}^2 \text{ kg}^{-2}$ is the gravitational constant. Then, we have

$$m_1\ddot{\boldsymbol{r}}_{\boldsymbol{1}} + m_2\ddot{\boldsymbol{r}}_{\boldsymbol{2}} = 0. \tag{2.2}$$

By integrating the equation, we obtain

$$m_1\dot{\boldsymbol{r}}_{\boldsymbol{1}} + m_2\dot{\boldsymbol{r}}_{\boldsymbol{2}} = \boldsymbol{a}, \tag{2.3}$$

and by integrating it again, we get

$$m_1\boldsymbol{r_1} + m_2\boldsymbol{r_2} = \boldsymbol{a}t + \boldsymbol{b}, \tag{2.4}$$

Here, $\boldsymbol{a}$ and $\boldsymbol{b}$ are constant vectors. Let us assume $R = (m_1\boldsymbol{r_1} + m_2\boldsymbol{r_2})/(m_1 + m_2)$ denotes the position vector of the centre of mass. Then, the above equations are re-expressed as

$$\dot{\boldsymbol{R}} = \frac{\boldsymbol{a}}{m_1 + m_2}, \qquad \boldsymbol{R} = \frac{\boldsymbol{a}t + \boldsymbol{b}}{m_1 + m_2}. \tag{2.5}$$

These equations imply that the center of mass moves with a constant velocity.

Now we consider the relative vector $\boldsymbol{r}$.

$$\boldsymbol{r} = \boldsymbol{r_2} - \boldsymbol{r_1}. \tag{2.6}$$

The values of $\boldsymbol{r}$ and $\boldsymbol{R}$ determine the positions $\boldsymbol{r_1}$ and $\boldsymbol{r_2}$. The center of mass $\boldsymbol{R}$ is determined by the choice of inertial frame of reference, so we may solve r to characterize the motions of two objects. From Equation (2.1), EoM for $\boldsymbol{r}$ is expressed as

$$\frac{d^2\boldsymbol{r}}{dt^2} + \mu\frac{\boldsymbol{r}}{r^3} = 0 \quad (\ \mu \equiv G(m_1 + m_2)\ ), \tag{2.7}$$

By taking the product of $\boldsymbol{r}$ with Equation (2.7), we obtain $\boldsymbol{r} \times \ddot{\boldsymbol{r}} = 0$, and time integration of $\boldsymbol{r} \times \ddot{\boldsymbol{r}} = 0$ leads to

$$\boldsymbol{r} \times \dot{\boldsymbol{r}} = \boldsymbol{h} \quad \rightarrow \quad \boldsymbol{r} \cdot \boldsymbol{h} = 0, \ \ \dot{\boldsymbol{r}} \cdot \boldsymbol{h} = 0, \tag{2.8}$$

which implies that $\boldsymbol{r}$ and $\dot{\boldsymbol{r}}$ are on the same plane perpendicular to the vector $\boldsymbol{h}$. This also means $\boldsymbol{r}$ always stays on a fixed plane.

Since the two bodies are on the same plane, we may specify the positions in a polar coordinate (r, θ). If $\hat{\boldsymbol{r}}$ and $\hat{\boldsymbol{\theta}}$ denote the unit vectors corresponding to polar coordinates, we obtain

$$r = r\hat{\boldsymbol{r}}, \quad \dot{r} = \dot{r}\hat{\boldsymbol{r}} + r\dot{\theta}\hat{\boldsymbol{\theta}}, \quad \ddot{r} = (\ddot{r} - r\dot{\theta}^2)\hat{\boldsymbol{r}} + \left[\frac{1}{r}\frac{d}{dt}\left(r^2\theta\right)\right]\hat{\boldsymbol{\theta}}, \tag{2.9}$$

where we use $\dot{\hat{\boldsymbol{r}}} = \dot{\theta}\hat{\boldsymbol{\theta}}$ and $\dot{\hat{\boldsymbol{\theta}}} = -\dot{\theta}\hat{\boldsymbol{r}}$.

Expressing the constant vector $\boldsymbol{h}$ in Equation (2.8) with the polar coordinate, we obtain

$$\boldsymbol{h} = \boldsymbol{r} \times \dot{\boldsymbol{r}} = r^2\dot{\theta}(\hat{\boldsymbol{r}} \times \hat{\boldsymbol{\theta}}), \tag{2.10}$$

$$\frac{1}{2}h = \frac{1}{2}r^2\frac{d\theta}{dt} = \frac{dS}{dt}. \tag{2.11}$$

From the above expressions, we see that an areal velocity dS/dt of the orbital motion is always constant $(1/2)h$. This fact is called Kepler's second law.

Comparing the $\hat{\boldsymbol{r}}$ component of Equation (2.7) and Equation (2.9), we obtain

$$\ddot{r} - r\dot{\theta}^2 = -\frac{\mu}{r^2}. \tag{2.12}$$

Changing the variable from r to $u = 1/r$ and making use of the constant $h = r^2\dot{\theta}$, we transfrom Equation (2.12) to

$$\frac{d^2u}{d\theta^2} + u = \frac{\mu}{h^2}, \tag{2.13}$$

where we use the following relations

$$\dot{r} = -\frac{\dot{u}}{u^2} = -\frac{1}{u^2}\frac{d\theta}{dt}\frac{du}{\delta\theta} = -h\frac{du}{d\theta}, \tag{2.14}$$

$$\ddot{r} = -h\dot{\theta}\left(\frac{du}{\theta}\right)^2 = -h^2 u^2 \frac{d^2 u}{d\theta^2}. \tag{2.15}$$

Equation (2.13) is similar to the wave equation, and it can be solved as follows;

$$u = \frac{\mu}{h^2}\left[1 + e\cos(\theta - \bar{w})\right], \tag{2.16}$$

or

$$r = \frac{h^2/\mu}{1 + e\cos(\theta - \bar{w})}, \tag{2.17}$$

where Equation (2.17) indicates that the orbit is an ellipse with eccentricity e and a phase constant $\bar{w}$.

We introduce a semi-major axis a; $a(1 + e)$ is equal to the maximum value of r. Then, Equation (2.17) is written by

$$r = \frac{a(1 - e^2)}{1 + e\cos(\theta - \bar{w})} = \frac{a(1 - e^2)}{1 + e\cos f}, \tag{2.18}$$

where $f = \theta - \bar{w}$ is called the true anomaly. The coordinates (x, y) are expressed as

$$x = r\cos f, \quad y = r\sin f. \tag{2.19}$$

To derive the position of the objects at arbitrary time, we need to relate f and t, which we will do in the next section.

Finally, we derive Kepler's third law. From Kepler's second law, an areal velocity is constant $h/2$. On the other hand, the area swept by a orbit is equal to $\pi a^2\sqrt{1 - e^2}$ in a period P . By equating these two expressions and using $h^2 = \mu a(1 - e^2)$, we obtain

$$\frac{h}{2} = \frac{\sqrt{\mu a(1 - e^2)}}{2} = \frac{\pi a^2\sqrt{1 - e^2}}{P} \quad \rightarrow \quad P^2 = \frac{4\pi^2}{\mu}a^3. \tag{2.20}$$

This is Kepler's third law. Note that the period is independent of e for the same a.

2.2   Position of an object in the Keplerian orbit at a certain time

In this section, we relate a time and position of a object in the Keplerian orbit. First, we define a mean motion as

$$n = \frac{P}{2\pi}. \tag{2.21}$$

In this notation, Kepler's third law is rewritten as

$$\mu = n^2 a^3. \tag{2.22}$$

The mean motion n is different from true $\dot{f}$ if $e \neq 0$, but describes the averaged value of $\dot{f}$. Using n, we define the mean anomaly as

$$M = n(t - \tau), \tag{2.23}$$

where the constant τ is the time of pericentre passage. The value of M is, in a sense, the mean velocity of f. The parameter M has no geometrical interpretation, but M and f are equal at epochs of the pericentre and apocentre passages; $M = f = 0$ at $t = \tau$ and $M = f = \pi$ at $t = \tau + P/2$.

As the Keplerian orbit is an ellipse, if we take the origin O to be the center of the ellipse, the coordinates $(\bar{x}, \bar{y})$ are represented by

$$\bar{x} = a \cos E, \quad \bar{y} = b \cos E, \tag{2.24}$$

where $b = a\sqrt{1 - e^2}$ and E is the eccentric anomaly. In this coordinate, the distance r is written by

$$r = a(1 - e \cos E), \tag{2.25}$$

and the phase is

$$\cos f = \frac{\cos E - e}{1 - e \cos E}. \tag{2.26}$$

The eccentric anomaly E has a geometrical interpretation as shown in Figure 2.1. Let us consider a point A on an elliptic orbit. We can draw a circle with a radius a, and we take the center of the circle to be at the same as the ellipse. Then, if we draw a line from A parallel to the y-axis, there will be the intersection point B (there are two intersections at most, and B is a nearer one to A). Then, E is equal to the angle between O-B and the x-axis.

The left task is to relate E and M. For this purpose, we derive an equation in the form of $\dot{r} = f(r)$. The squared velocity is represented in a polar coordinate as follows;

$$v^2 = \dot{r}^2 + r^2 \dot{f}^2. \tag{2.27}$$

Using the expression for r, we obtain $\dot{r}$ and $r\dot{f}$;

$$\dot{r} = \frac{na}{\sqrt{1 - e^2}} e \sin f, \tag{2.28}$$

$$r\dot{f}(= h/r) = \frac{na}{\sqrt{1 - e^2}}(1 + e \cos f) = \frac{na^2\sqrt{1 - e^2}}{r}. \tag{2.29}$$

From Equation (2.28) and Equation (2.29), we obtain

$$\begin{aligned} v^2 &= \frac{n^2 a^2}{1 - e^2} e^2 \sin^2 f + \frac{n^2 a^2}{1 - e^2}(1 + 2e \cos f + e^2 \cos^2 f) \\ &= \frac{n^2 a^2}{1 - e^2}(1 + e^2) + \frac{2n^2 a^2}{1 - e^2}\left(\frac{a(1 - e^2)}{r} - 1\right) = \mu\left(\frac{2}{r} - \frac{1}{a}\right). \end{aligned} \tag{2.30}$$
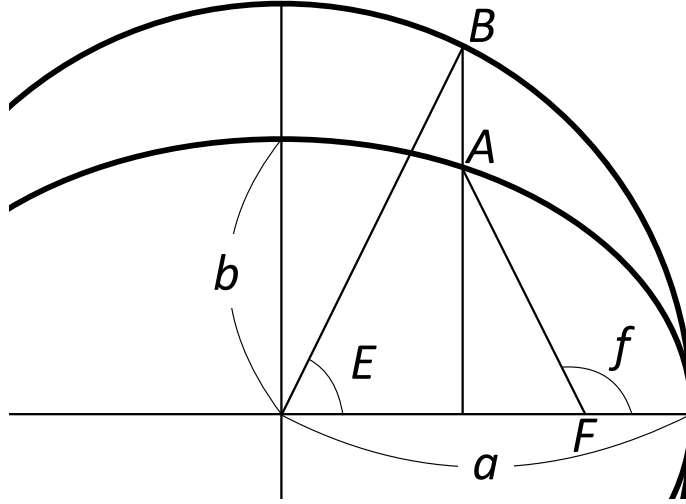
Figure 2.1: Schematic illustration of f and E. The definitions of them are described in the text. In the figure, we assume that the star is at F, and the planet is at A.

To derive an equation $\dot{r} = f(r)$, we insert Equation (2.29) and Equation (2.30) into Equation (2.27) and obtain

$$\dot{r}^2 = v^2 - r^2\dot{f}^2 = \mu\left(\frac{2}{r} - \frac{1}{a}\right) - \frac{n^2a^4(1-e^2)}{r^2} = \frac{n^2a^2}{r^2}[a^2e^2 - (r-a)^2]. \qquad (2.31)$$

By substituting E in Equation (2.25) into Equation (2.31), we get

$$\dot{E} = \frac{n}{1 - e\cos E}, \qquad (2.32)$$

which reduces to

$$n(t - \tau) = M = E - e\sin E. \qquad (2.33)$$

Equation(2.33) is called Kepler's equation. Once we relate t with E using this equation, we obtain the position ($\bar{x} = a\cos E, \quad \bar{y} = b\cos E$) in Equation (2.24). It remains to solve the E as a function of t.

Equation (2.33) cannot be solved analytically for $E = E(t)$, so we solve it using techniques of a series expansion or a numerical calculation. A series solution can be derived iteratively as

$$E_{i+1} = M + e\sin E_i, \quad \text{assuming that } e < 0.662347... . \qquad (2.34)$$

As the zeroth order, we take $E_0 = M$. Starting from this expression, we can obtain the arbitrary order for E using Equation ation (2.34). We show some examples of

these in the following

$$E_1 = M + e \sin M, \tag{2.35}$$

$$E_2 = M + e \sin E_1 \simeq M + e \sin M + \frac{1}{2} e^2 \sin 2M, \tag{2.36}$$

$$E_3 = M + e \sin E_2 \simeq M + \left(e - \frac{1}{8} e^3 \right) \sin M + \frac{1}{2} e^2 \sin 2M + \frac{3}{8} e^3 \sin 3M. \tag{2.37}$$

At the i-th step E_i, we stop the expansion at i-th order of e. In this way, we obtain the equation

$$E = M + \sum_{s=1}^{\infty} b_s(e) \sin sM, \tag{2.38}$$

where $b_s(e) = \mathcal{O}(e^s)$.

Equation (2.38) becomes divergent for $e > 0.6627434$, and one has to resort to a numerical method. Here, we introduce one simple numerical scheme. Let us define $g(E)$ as

$$g(E) = E - e \sin E - M. \tag{2.39}$$

The exact expression for E must satisfy $g(E) = 0$, and we can use the Newton-Raphson method to find the solution for $g(E) = 0$. The detailed scheme is

$$E_{i+1} = E_i - \frac{f(E_i)}{f'(E_i)} = E_i - \frac{E_i - e \sin E_i - M}{1 - e \cos E_i}. \tag{2.40}$$

Starting from $E_0 = M$, we can find $E(M)$ for an arbitrary e by iterating the above scheme.

2.3   Orbital motion in three-dimension space

So far, we have considered only an orbit in two dimension, but in general, we have to trace it in three dimension. For this purpose, we introduce additional three angles (i, ω, Ω) and related two coordinates (X, Y, Z) and (x, y, z) in Fig 2.2.

The orbital plane is on the (x, y)-plane, and the z-axis is taken to be perpendicular to the plane. The x-axis is taken to be in parallel with the direction of the periapse from the center of the orbit. Here, the term "periapse" refers to the nearest position of the body to the secondary object. The y-axis is taken to form (x, y, z) as a right-handed triad. The other coordinate system (X, Y, Z) is a reference frame for (x, y, z). The choice of (X, Y, Z) is arbitrary, and we usually take it for the line of sight to be one of three axes.

Two coordinates (X, Y, Z) and (x, y, z) are related through (i, ω, Ω). First, the inclination angle i is defined to be the angle between the orbital plane ($x - y$ plane) and the $X - Y$ plane. The longitude of the ascending node Ω is the angle between the reference line (X axis) and the line that is drawn from the origin to the ascending node. Finally, the argument of periapse ω represents the angle between two vectors
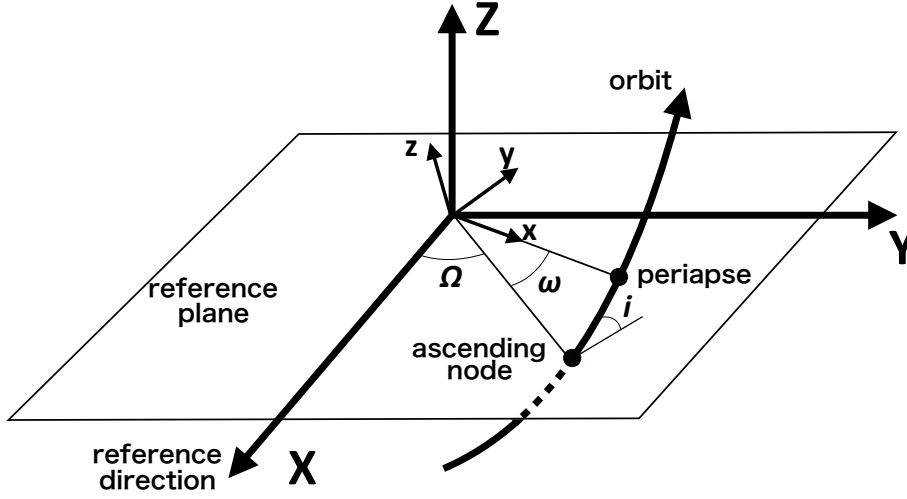
Figure 2.2: Schematic illustration of orbital motion. The coordinate systems (x, y, z) and (X, Y, Z) are related by (i, ω, Ω).

starting from the origin; one is to the ascending node and the other is to the perirapse. In case of multi bodies, we can specify the motion of the m-th object by assigning the coordinates $(x^{(m)}, y^{(m)}, z^{(m)})$ or $(i^{(m)}, \omega^{(m)}, \Omega^{(m)})$ to it with reference to (X, Y, Z).

We usually use a variable $\bar{\omega}$;

$$\bar{\omega} = \Omega + \omega, \tag{2.41}$$

which corresponds to the value of $\bar{\omega}$ in two dimension when $i = 0$. To complete the useful set of angles, we introduce the mean longitude;

$$\lambda = M + \bar{\omega}. \tag{2.42}$$

Finally, using three angles (i, ω, Ω), we derive a relation of coordinate values between (x, y, z) and (X, Y, Z); see Figure 2.2. Let us call $P_i(\theta)$ a rotation matrix, with which we turn the coordinate values θ radians around the i-th axis. For example, $P_X(\theta)$ have elements

$$P_X(\theta) = \begin{pmatrix} 1 & 0 & 0 \\ 0 & \cos\theta & -\sin\theta \\ 0 & \sin\theta & \cos\theta \end{pmatrix}. \tag{2.43}$$

With the help of this matrix, (x, y, z) and (X, Y, Z) are related in the following way;

$$\begin{pmatrix} X \\ Y \\ Z \end{pmatrix} = P_Z(\Omega) P_X(i) P_Z(\omega) \begin{pmatrix} x \\ y \\ z \end{pmatrix}. \tag{2.44}$$

Using the expression $x = r \cos f$ and $y = r \sin f$, we obtain

$$X = r(\cos\Omega\cos(\omega + f) - \sin\Omega\sin(\omega + f)\cos i), \tag{2.45}$$

$$Y = r(\sin\Omega\cos(\omega + f) + \cos\Omega\sin(\omega + f)\cos i), \tag{2.46}$$

$$Z = r\sin(\omega + f)\sin i. \tag{2.47}$$

From the observer in the direction of Z-axis, the choice of Ω is completely free, and we take $\Omega = 180°$ in this thesis.

Chapter 3

Transit photometry

An eclipse is an astronomical event that occurs when a celestial object covers another object. Eclipse is observed not only in a star-star system but also in a star-planet system, and it enables us to detect the planet. This technique, called transit photometry, is one of the most successful methods for detecting exoplanets. In this section, we review the transit phenomenon following Winn (2010).

3.1 Terminology

In general, a term "transit" refers to the eclipse, during which the smaller object passes in front of the larger one. On contrary, terms "occultation" and "secondary eclipse" are often used when the smaller object passes behind the larger one. For example, let us consider a system composed of a star and a small planet. When the planet passes the star, it is called "transit". In this case, the blocked light of the star is substantial. On the other hand, when the planet is behind the star, it is called "occultation". In this case, the decrement in the total flux is small because the planet emits much less light than the star.

3.2 Condition for transits and their probabilities

In this subsection, we will derive the condition for transits to occur. The schematic illustration of the transit is shown in Figure 3.1. Let us suppose that a planet with a radius R_p and mass M_p orbits around a star with a radius $R_\star$ and mass $M_\star$. From Equations (2.45) and (2.46), the distance from the star to the planet is given by

$$r_{\text{sky}} = \sqrt{X^2 + Y^2} = \frac{a(1-e^2)}{1 + e\cos f}\sqrt{1 - \sin^2(\omega + f)\sin^2 i}, \qquad (3.1)$$

where we assume the observer is along the direction of Z. The value of r_{sky} determines the geometric configuration, which has the three following possibilities.

- Out of transit: $R_\star + R_p \leq r_{\text{sky}}$

- On the limb: $R_\star - R_p \leq r_{\text{sky}} \leq R_\star + R_p$

- In transit: $0 \leq r_{\text{sky}} \leq R_\star - R_p$
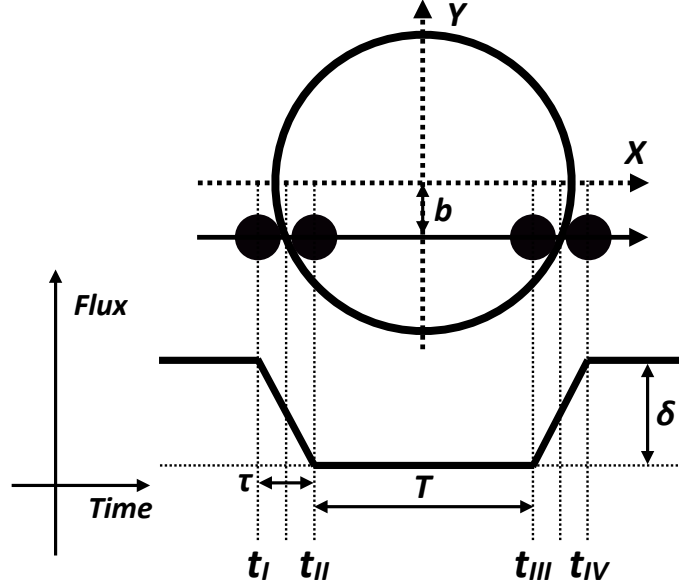
Figure 3.1: Schematic illustration of a transit.

Because the semi major axis a in Equation (3.1) is generally much larger than $R_\star$, the value in the square root in Equation (3.1) should be sufficiently small for the transit to occur. Thus, in general the following condition should satisfy during the transit

$$\sin i \simeq 1.0 \quad \sin^2(\omega + f) \simeq 1.0 \tag{3.2}$$

In this approximation, we obtain approximately the central time of the transit

$$f_{\text{tra}} = \frac{\pi}{2} - \omega, \tag{3.3}$$

which corresponds to the condition $\sin^2(\omega + f) = 1$. While the central time of the transit is given by Equation (3.3), the central time of the occultation is given by

$$f_{\text{occ}} = -\frac{\pi}{2} - \omega, \tag{3.4}$$

In the following, we only consider the values for the transit f_{tra}, but the corresponding values for f_{occ} are obtained just changing $\omega \to -\omega$ of values for f_{tra}.

Approximating the central time of the transit with f_{tra}, we define the dimensionless impact parameter of the transit b:

$$b = \frac{r_{\text{sky}}(f_{\text{tra}})}{R_\star} = \frac{a \cos i}{R_\star} \frac{1 - e^2}{1 + e \sin \omega}, \tag{3.5}$$

which corresponds to the distance at $f = f_{\rm tra}$ normalized by the stellar radius. The necessary condition that the eclipses including a grazing transit is $|b| < 1 + R_{\rm p}/R_\star$. Here grazing transit refers to the transit during which the planet is always on the limb of the star. The condition $|b| < 1 + R_{\rm p}/R_\star$ is transformed into

$$|\cos i| < \frac{R_\star + R_p}{a} \frac{1 + e \sin \omega}{1 - e^2} \equiv \cos i_0. \tag{3.6}$$

Then, the probability of the transit for a random observer is given by

$$p_{\rm tra} = \int_{i_0}^{\pi/2} \sin i \, di = \cos i_0 = \frac{R_p + R_\star}{a} \frac{1 + e \sin \omega}{1 - e^2}. \tag{3.7}$$

The above expression Equation (3.7) leads to the following form in the limit of $R_p \ll R_\star$ and $e = 0$;

$$p_{\rm tra} = \frac{R_\star}{a} = 0.005 \frac{R_\star}{R_\odot} \left(\frac{a}{1 {\rm AU}} \right)^{-1}, \tag{3.8}$$

where $R_\odot$ is Sun's radius. The probability $p_{\rm tra}$ only considers whether the observer is on the region where see the transit can be observed. To calculate the expected number of the transits in the observation, we also need to take into account additional factor $T_{\rm obs,dur}/P$, where $T_{\rm obs,dur}$ is the observational duration and P is the orbital period.

3.3   Transit duration in circular and eccentric orbits

In this section, we will derive a transit duration for a planet. If $|b| < 1 - k$, the stellar and planetary disks have four contact points during the eclipse. We denote the time of these four contacts by $t_I \sim t_{IV}$ as shown in Figure 3.1, which can be obtained by solving the following equation;

$$r_{\rm sky}(f) = \frac{a(1 - e^2)}{1 + e \cos f} \sqrt{1 - \sin^2(\omega + f) \sin^2 i} = R_\star \pm R_{\rm p}. \tag{3.9}$$

3.3.1   Circular case

When $e = 0$, Equation (3.9) has analytical solutions. If we take the transit center to satisfy $t = 0$, we have

$$t_I = -\frac{P}{2\pi} \sin^{-1} \left[\frac{R_\star}{a} \frac{\sqrt{(1 + k)^2 - b^2}}{\sin i} \right], \quad t_{II} = -\frac{P}{2\pi} \sin^{-1} \left[\frac{R_\star}{a} \frac{\sqrt{(1 - k)^2 - b^2}}{\sin i} \right],$$

$$t_{III} = \frac{P}{2\pi} \sin^{-1} \left[\frac{R_\star}{a} \frac{\sqrt{(1 - k)^2 - b^2}}{\sin i} \right], \quad t_{IV} = \frac{P}{2\pi} \sin^{-1} \left[\frac{R_\star}{a} \frac{\sqrt{(1 + k)^2 - b^2}}{\sin i} \right].$$

$$\tag{3.10}$$

The total duration $T_{\text{tot}} = t_{IV} - t_I$ and the full duration $T_{full} = t_{III} - t_{II}$ are given by

$$T_{\text{tot}} = \frac{P}{\pi} \sin^{-1} \left[\frac{R_\star}{a} \frac{\sqrt{(1+k)^2 - b^2}}{\sin i} \right], \quad T_{\text{full}} = \frac{P}{\pi} \sin^{-1} \left[\frac{R_\star}{a} \frac{\sqrt{(1-k)^2 - b^2}}{\sin i} \right].$$
(3.11)

If we take the limit $R_p \ll R_\star$, $b < 1 - k$, and $R_\star/a \ll 1$, we obtain

$$T \simeq \frac{R_\star P}{\pi a}(= T_0)\sqrt{1 - b^2}, \quad \tau = \frac{T_0}{\sqrt{1 - b^2}} \frac{R_p}{R_\star},$$
(3.12)

where T_0 is a typical timescale

$$T_0 = \frac{R_\star P}{\pi a} \simeq 13\text{h} \left(\frac{P}{1\text{yr}} \right)^{1/3} \left(\frac{\rho_\star}{\rho_\odot} \right)^{-1/3},$$
(3.13)

where ρ is the stellar density of Sun. Equation (3.13) implies that one can estimate the stellar density $\rho_\star$ for the two observables T_0 and P alone.

3.3.2   Eccentric orbit

In the case of $e \neq 0$, the expressions of the above values are slightly different. In this section, we calculate this connection. Although we only derive the expression to the orders of e^2 and $(R_\star/a)$, we can expand it to the arbitrary orders.

The duration between t_β and t_α is given in terms of the integration over the true anomaly:

$$t_\beta - t_\alpha = \int_{t_\alpha}^{t_\beta} dt = \int_{f_\alpha}^{f_\beta} \left(\frac{df}{dt} \right)^{-1} df = \frac{P(1 - e^2)^{3/2}}{2\pi} \int_{f_\alpha}^{f_\beta} \frac{1}{(1 + e\cos f)^2} df, \quad (3.14)$$

where we assume $\alpha = I, II$ and $\beta = III, IV$. The edge phases f_α and f_β are obtained from the solutions of Equation (3.9). Equation (3.9) and Equation (3.14) cannot be solved analytically, so we solve them using approximations instead. We rewrite Equation (3.9) using the term $f = (\pi/2 - \omega) + \Delta f$ ($\Delta f \sim R_\star/a$ when $e = 0$):

$$(1 \pm (R_p/R_\star))^2 = (a/R_\star)^2 \frac{(1 - e^2)^2}{(1 + e\sin\omega + e\Delta f \cos\omega)^2}(\cos^2 i + (\Delta f)^2 \sin^2 i). \quad (3.15)$$

The above equation yields

$$(\Delta f)^2 = \frac{1}{\sin i^2} \left[(R_\star/a)^2 (1 \pm (R_p/R_\star))^2 \frac{(1 + e\sin\omega + e\Delta f \cos\omega)^2}{(1 - e)^2} - \cos^2 i \right] \quad (3.16)$$

$$\simeq \frac{1}{\sin^2 i} \left(\frac{R_\star}{a} \right)^2 \frac{(1 + e\sin\omega)^2}{(1 - e^2)^2} \left((1 \pm (R_p/R_\star))^2 - b^2 \right), \quad (3.17)$$

where we neglect $[e\Delta f \sim (eR_\star/a)]$ terms in the last expression. Finally, we obtain

$$\Delta f = \pm\frac{1}{\sin i} \frac{R_\star}{a} \frac{1 + e\sin\omega}{1 - e^2} \sqrt{(1 \pm (R_p/R_\star))^2 - b^2}. \quad (3.18)$$

Equations (3.14) and (3.18) give the time duration T_{tot} and T_{full}:

$$T_{\text{tot}} = \frac{P}{\pi} \frac{R_\star}{a} \frac{\sqrt{(1 + R_{\text{p}}/R_\star)^2 - b^2}}{\sin i} \left(\frac{\sqrt{1 - e^2}}{1 + e \sin \omega} \right),$$

$$T_{\text{full}} = \frac{P}{\pi} \frac{R_\star}{a} \frac{\sqrt{(1 - R_{\text{p}}/R_\star)^2 - b^2}}{\sin i} \left(\frac{\sqrt{1 - e^2}}{1 + e \sin \omega} \right). \tag{3.19}$$

In the derivations of Equation (3.19), the term $1/(1 + e \cos f)^2$ in Equation (3.14) is replaced by $1/(1 + e \sin \omega)^2$ in the current order. We note that the duration in a eccentric orbit Equation (3.19) is obtained by just multiplying $\sqrt{1 - e^2}/(1 + e \sin \omega)$ with the duration in a circular orbit Equation (3.11). According to Winn (2010), the difference between $\tau_{\text{ing}} = t_{II} - t_I$ and $\tau_{\text{egr}} = t_{IV} - t_{III}$ to the leading order is given by

$$\frac{\tau_{\text{egr}} - \tau_{\text{ing}}}{\tau_{\text{egr}} + \tau_{\text{ing}}} = e \cos \omega \left(\frac{R_\star}{a} \right)^3 (1 - b^2)^{3/2}. \tag{3.20}$$

This quantity is less than $10^{-2}e$ even for a close-in planet, so we may ignore the difference in τ_{egr} and τ_{ing} in practice.

3.4   Observables in transit photometry

The main observables in transit include δ, τ, T, and P (the value of $\tau_{\text{egr}} - \tau_{\text{ing}}$ is much small, so we may neglect it). These observables are directly related to three physical parameters ($R_{\text{p}}/R_\star$, $a/R_\star$, b) if a circular orbit is assumed. Especially, under the assumption of $R_{\text{p}} \ll R_\star$, $b < 1 - R_{\text{p}}/R_\star$, and $R_\star/a \ll 1$, we obtain

$$\frac{R_{\text{p}}}{R_\star} = \sqrt{\delta}, \quad b^2 \simeq 1 - \frac{T}{\tau} \sqrt{\delta}, \quad \frac{R_\star}{a} \simeq \frac{\pi}{\delta^{1/4}} \frac{\sqrt{\tau T}}{P}, \tag{3.21}$$

where we assume that the stellar brightness is constant and the planetary flux is negligible.

In reality, the value of $a/R_\star$ in Equation (3.21) differs from the true $a/R_\star$ due to an eccentricity, and this would lead to the wrong estimation of $\rho_\star$ in Equation (3.13) (Kipping 2014). However, $\rho_\star$ can be measured by other probes, and the comparison of $\rho_\star$ in Equation (3.21) and that derived from other methods will reveal the true $a/R_\star$ and e of the system.

If we can observe the occultation, we can also constrain e and ω. First, the period between the transit and the occultation to the order of e is related to $e \cos \omega$ in the following:

$$t_{\text{tra}} - t_{\text{occ}} = \frac{P(1 - e^2)^{3/2}}{2\pi} \int_{f_\alpha}^{f_\beta} \frac{1}{(1 + e \cos f)^2} df \tag{3.22}$$

$$\simeq \frac{P}{2\pi} \int_{-\pi/2 - \omega}^{\pi/2 - \omega} 1 - 2e \cos f \, df \tag{3.23}$$

$$= \frac{P}{2} \left(1 - \frac{4e \cos \omega}{\pi} \right). \tag{3.24}$$

On the other hand, the ratio of transit duration T_{tra} in Equation (3.19) and T_{occ} ($\omega \to -\omega$ in Equation (3.19)) is related to $e\cos\omega$;

$$\frac{T_{\mathrm{tra}}}{T_{\mathrm{occ}}} \simeq \frac{1 - e\sin\omega}{1 + e\sin\omega} \simeq 1 - 2e\sin\omega. \tag{3.25}$$

Thus, the duration and timing of the occultation can give the constraint on $(e\sin\omega, e\cos\omega)$ or (e, ω), and it also enables the correct estimate of $a/R_\star$.

Chapter 4

A Review on previously reported planetary rings and ring candidates

In the Solar system, giant planets all have planetary rings. In addition, the possible planetary rings have been also discovered outside the Solar system. The properties of these rings would be very suggestive for a ring search. In this section, we summarize our knowledge of observed planetary rings looking ahead a search for exoplanetary rings.

4.1 In the Solar system

In this subsection, we will review planetary rings in the Solar system. In each subsection, we first review their histories of characterizations, and then we discuss their properties. The basic parameters of the rings are summarized in Table 4.1.

4.1.1 Saturn rings

Saturn rings were discovered by Galileo Galilei with his own telescope in 1610. When Galileo first looked at Saturn for the first time, it looked like the planet was surrounded by two satellites. However, after long observations of Saturn, Christiaan Huygens realized that the orbiting objects are not satellites but rings instead. Subsequently, Giovanni Cassini discovered the Cassini Division that resides between A ring and B ring.

In the 20th century, spacecrafts started to be sent to planets in the Solar System to directly observe them. The first visitor to Saturn is the spacecraft named Pioneer 11. It did a flyby in 1979, and it revealed the prominent features of Saturn including the detailed thickness of rings and the existence of very narrow rings "F ring" (Gehrels et al. 1980). Now, F ring is considered to be confined by Saturn's satellite(s) and a tidal force arising from Saturn (e.g. Cuzzi et al. 2014). After the arrival by Pioneer

Table 4.1: Basic parameters of planetary rings in Solar system.
The data are taken from http://nssdc.gsfc.nasa.gov/planetary/factsheet/.

	Location(km)	Optical depth	Albedo	Width(km)
		Saturn Rings		
Saturn Equator	60,268			
D ring	66,900-74,510	10^{-5}		
C inner edge	74,658	0.05-0.35	0.12 - 0.30	
C outer edge	91,975	0.05-0.35	0.2	
B inner edge	91,975	0.4-2.5	0.4-0.6	
B outer edge	117,507	0.4-2.5		
Cassini division	117,507-122,340	0-0.1	0.2-0.4	
A ring	122,340-136,780	0.4-1.0	0.4-0.6	
F ring	139,826	0.1	0.6	50
G ring	166,000-173,000	10^{-6}	10^5	
E ring	180,000 - 480,000	10^{-6}	10^7	
		Jupiter Rings		
Jupiter Equator	71,492			
Halo	89,400-123,000	3×10^{-6}		
Main Ring	123,000-128,940	5×10^{-6}	0.015	
Amalthea Ring	128,940-181,350	1×10^{-7}		
Thebe Ring	181,350-211,900	1×10^{-7}		
Thebe Extension	221,900-280,000	1×10^{-7}		
	Location (km)	Optical depth	Albedo ($\times 10^{-3}$)	Width (km)
		Uranus Rings		
Uranus equator	25,559			
6	41,837	0.3	15	1.5
5	42,234	0.5	15	2
4	42,571	0.3	15	2
α	44,718	0.4	15	4-10
β	45,661	0.3	15	5-11
η	47,176	0.4	15	1.6
γ	47,627	0.3	15	1-4
δ	48,300	0.5	15	3-7
λ	50,024	0.1	15	2
ϵ	51,149	0.5-2.3	18	29-96
		Neptune Rings		
Neptune equator	24,766			
Galle	41,900	10^{-4}	15	2000
LeVerrier	53,200	0.01	15	100
Lassell	53,200	10^{-4}	15	4000
Adams	62,933	0.01-0.1	15	15

Figure 4.1: Picture of Saturn rings taken by the Cassini spacecraft. Credit: NASA.

11, the subsequent spacecrafts Voyager 1 and 2 conducted the flyby in 1980 and 1981. Through the flybys, they revealed the surface structure of Saturnian moons, evidence of dynamical changes in rings, and the property of Saturn's atmosphere via radar. After dozens of years, Cassini-Huygens arrived at Saturn in 2004. The most distinct point of the visit by Cassini-Huygens is that they orbit around Saturn (over 100 times until now) while past three spacecrafts just did the flybys. Moreover, beyond just orbit motions around Saturn, Huygens separated from Cassini-Huygens in 2005 and landed at Saturn's moon Titan. In fact, this was the first landing for human being in Outer Solar System. The finding of Cassini-Huygens is reviewed in Dougherty et al. (2009).

Saturn's rings are very optically thick, and the photometric effect is very significant. This is also seen in Figure 4.1 taken by Cassini. The rings are mainly composed of ice, and the size of ring particles in the main rings range from 1cm to 10 m. While rings have large photometric effect, their mass is very small; rings are 10^8 lighter than the body of Saturn. Therefore, it is difficult to see the dynamical effect of the rings on the planet. Instead, we can observe the dynamical effect on the rings by the gravity from the planet. From the above simple discussions, we had better use the photometric observation rather than other ways depending on mass of rings to probe exoplanetary rings.

4.1.2   Jupiter rings

Jupiter rings were first discovered through the long-exposure image taken by Voyager 1 (Owen et al. 1979). Actually, this discovery was achieved observation because of the implications from the data of Pioneer 11 with charged particles detectors (e.g. Fillius et al. 1975). Jupiter's rings were too faint to be observed from the ground in the past, and they are only rings that were discovered by the spacecraft. After several flybys of these spacecrafts, the first spacecraft orbiting Jupiter named "Galileo" arrived at the planet in 1995, and revealed many aspects including the fact that the ring systems are formed from the dust emitted by moons during the impact. In 2007, New horizons also encountered Jupiter.

As already mentioned, Jupiter rings are very faint and optically thin ($\tau \sim 10^{-6}$). Therefore even if an exoplanet possesses the Jupiter-like ring, it is very difficult to confirm it from Earth. In addition, the ring particles have very small size $\sim \mu$ m, so they are easy to lose their orbital velocity due to the radiation. Indeed, the lifetime of ring particles are considered to be 10^5 years. In case of Jupiter, however, the rings can maintain their structure due to the supply of particles from the Jupiter satellites.

4.1.3   Uranus rings

Uranus rings were first discovered by James L. Elliot, Edward W. Dunham, and Jessica Mink in 1977 (Elliot et al. 1977). The method they used is the observation of occultations of the background star blocked by the Uranus rings. The rings were thoroughly investigated by Voyager 2 during the flyby around Uranus. Voyager 2 gave the estimate of the phase function and albedo of rings through the long observations of forward scattering, back-scattering, and side-scattering.

Uranus rings have 10 main narrow rings ranging from 1.64 to 2.0 R_{J}(Esposito 2002). The width of ringlets is at most several tens of kilometers. While rings are so narrow, their opacity is enough to cover the light from the background star. The rings are mostly composed of large bodies $0.2 - 20$ m while they also contain small amount of dust. They are made of dark materials, and their observed geometrical albedo is less than 6%. The rings are packed together very much due to some mechanism, and if such mechanisms suddenly turn off, the rings will vanish in 1 million years.

4.1.4   Neptune rings

The rings of Neptune first discovered by Patrice Bouchet in 1984. The first detailed investigation was conducted by Voyager 2 during the flyby, and Voyager 2 revealed a lot of aspects of Neptunian rings in the same fashion as Uranus. So far, Voyager 2 is the only satellite which directly contacted Neptune.

Neptune's rings are mainly composed of four faint rings and five bright arcs called Adams arcs. The width of the faint rings is about a few thousands of kilometers, and their optical depth ranges from $10^{-2} \sim 10^{-4}$ (Esposito 2002). In contrast, Adams arcs are very narrow with the width of 10 km while they are comparatively optically thick ($\tau \sim 10^{-1}$). In both kinds of rings, the dust fraction is several tens of percent, and the geometrical albedo is very low. There has been no clear observation about the composition of rings, but at least they are not mainly composed of ice due to low albedo.

4.2   Outside the Solar system

There have been three reports on the possible signals of the planetary rings around J1407b, 51 Pegasi b, and Formalhaut b. Actually, J1407b and Formalhaut b are young planets($\sim$ 10 Myr), and their rings are considered to be circumplanetary rings

unlike Saturn rings even if they exist. In addition, as discussed in the following, the hypothetical ring around 51 Pegasi b is unlikely to exist. Nevertheless, it would be very important to summarize these researches for the future finding of the ringed planet like Saturn.

4.2.1   J1407b

Very peculiar light curves of K5 pre-MS 16 Myr-old star J1407 were discovered during the SuperWASP surveys (e.g. Butters et al. 2010), and the field was also covered by the All Sky Automated Survey (e.g. Pojmanski 2002). In both observations, the light curves show long (~ 50 days), deep, and complicated features, which cannot be explained by a ordinary planetary transit. Instead, these light curves can be interpreted by the transit of the planet with giant rings with a typical size $\sim AU$ (Mamajek et al. 2012). In the following, we summarize constrains of this system and their implications.

First, let us summarize the constrains on this significant system from several viewpoints. Kepler's law gives one constrain among P, a, $R_{\rm p}$, $R_\star$. The observed transit duration gives another constrain among P, a, e, $R_{\rm disk}$. In addition, the slope of the light curves during the transit provides the minimum relative velocity $v = 33$km s^{-1} with the stellar radius $R_\star = 0.99 \pm 0.11 R_\odot$ (van Werkhoven et al. 2014), where $R_\star$ is estimated from the combination of $T_{\rm eq}$ and the stellar luminosity $L_\star$ (Kenworthy et al. 2015). Furthermore, the system was investigated by several measurements including direct imaging, radial velocity measurement, and the photometric observations (Kenworthy et al. 2015). These observations give constraints on the relation between mass and angular separation, the period, and the radial velocity. Theoretically, the value of $R_{\rm disk}$ should not exceed the Hill radius $R_{\rm Hill} = a(M_{\rm p}/M_\star)^{1/3}$ because of dynamical stability.

Combining these constraints, Kenworthy et al. (2015) calculated the allowed region of mass and period. For example, in a circular orbit, they estimated probable mass and period as $M = 17.1 M_{\rm jup}$ $P = 10.2$ yrs assuming $v > 12$kms^{-1} and $R_{\rm disk} < 0.4 R_{\rm Hill}$. However, if one takes into the account the additional constraint $v > 33$km/s, there are no solutions on the assumption of the circular orbits. In fact, this high orbital velocity can be consistent with the eccentric orbits because the maximum orbital velocity increases by the factor of $(1+e)^{1/2}/(1-e)^{1/2}$. Assuming the eccentric orbits, Kenworthy et al. (2015) recalculated the allowed region of mass and period, and they found that the systems needs high eccentricity $e > 0.7$ to satisfy $v > 33$km/s^{-1}. Assuming $0.7 < e < 0.8$, they obtained $P = 13.3$yrs and $M = 23.8 M_{\rm Jup}$ for the J1407b.

Adapting these values $P = 13.3$yrs and $M = 23.8 M_{\rm Jup}$, Kenworthy & Mamajek (2015) estimated $R_{\rm disk} = 0.6$ AU. This radius is two orders of magnitude larger than the Roche limit for the mass of J1407b. This radial excess possibly means that the rings are formed together with the planet, and they may be proto-circumplanetary disks.

Interestingly, the solution in Kenworthy & Mamajek (2015) also implies 36 gap structure, which can be interpreted as exomoons. Assuming the gap width corresponds

to the Hill radius of the moons, Kenworthy & Mamajek (2015) found the upper limit of satellite's mass:

$$m_{\mathrm{sat,up}} = 0.8 M_{\oplus} \left(\frac{M_{\mathrm{J1407b}}}{23.8 M_{\mathrm{Jup}}} \right). \tag{4.1}$$

From the different point of view, Rieder & Kenworthy (2016) investigated the stability of this ring system. They performed an N-body simulation, which only includes a gravitational interaction, and they found that the orbit should be retrograde for the system to survive for at least 10^4 orbits. If this cirucumplanetary ring was formed form the protoplanetary disk, their orbital motions should be naturally aligned with the planetary orbit. This unexpected reverse orbital motions might be resolved by theories including planet-planet scattering and Kozai mechanism, which are applicable to retrograde planetary systems outside the Solar system.

4.2.2   51 Pegasi b

Recent observations have shown a large reflected light and a high velocity components in the spectrum of 51 Pegasi b, and one explanation of these anomalies is a reflection by a ringed planet. In this section, we summarize these observations and an interpretation with a ringed planet.

First, we summarize the recent observations of this system. 51 Pegasi b is considered to be a hot Jupiter with $P = 4.23$ days, $a = 0.0527$ AU, and $M_{\mathrm{p}} \sin i = 0.472 M_{\mathrm{J}}$. Martins et al. (2015) explored the reflected light spectrum using the cross correlation function, and they found evidence of the reflected light, whose relative flux is $6.0 \pm 0.4 \times 10^{-5}$. This large reflected light can be interpreted by an inflated hot Jupiter with $R_{\mathrm{p}} = 1.9 \pm 0.3 R_{\mathrm{J}}$ on the assumption of albedo of 0.5. Furthermore, they also detected an line broadening in the planetary spectrum, and their results imply a very rapid rotation $v \sim 18$km s^{-1}. Surprisingly, this velocity is much higher than the expected velocity for the synchronous orbital motion of the planet.

To explain this anomalously high velocity, Santos et al. (2015) considered the possibility that the ring orbiting around the planet reflected the light and produced the large line broadening. Assuming that the star, the planet, and Earth are on the same line, they consider the reflected light $F_{\mathrm{planet+ring}}$ in a simple manner:

$$\frac{F_{\mathrm{planet+ring}}}{F_{\star}} = A_{\mathrm{g}} \left(\frac{R_{\mathrm{p}}}{a} \right)^2 + A_{\mathrm{g}}^{\mathrm{r}} g_{\mathrm{ring}}(\phi) \left[\left(\frac{r_o}{a} \right)^2 - \left(\frac{r_i}{a} \right)^2 \right], \tag{4.2}$$

where $g_{\mathrm{ring}}(\phi)$ is the phase function of the ring, r_o is the radius of the outer ring, r_i is the radius of the inner ring, and A_{g} and $A_{\mathrm{g}}^{\mathrm{r}}$ are the albedo of the planet and rings respectively. They compare this phase function with the observed reflection light, and give the constrain between ϕ and $A_{\mathrm{g}}^{\mathrm{r}}$. In analysis, they assume the planetary albedo $A_{\mathrm{g}} = 0.3$, the outer radius of ring $r_o = 3 R_{\mathrm{Jup}}$, the inner radius of ring $r_{\mathrm{i}} = R_{\mathrm{Jup}}$, and the planetary radius $R_{\mathrm{p}} = R_{\mathrm{Jup}}$. Assuming the Kepler motion and the planetary mass $M_{\mathrm{p}} = 0.46 M_{\mathrm{Jup}}$, they obtained the velocity $v = 17$km s^{-1} at $r = r_o$ and $v = 30$km s^{-1}

at $r = r_i$. These values are consistent with the observed line broadening found in Santos et al. (2015).

Their ring model can explain the data well, but their solutions need the unnecessary tilted ring system with $\phi > 40°$. In fact, the planetary obliquity near the host star is known to be damped within the timescale (e.g. Correia & Laskar 2009):

$$\tau = \left(\frac{a}{R_\mathrm{p}}\right)^3 \frac{P_\mathrm{orb} Q M_\mathrm{p}}{9\pi k_2 M_\mathrm{s}}, \tag{4.3}$$

where k_2 is the Love number, and Q is the dissipation quality factor. Adapting $Q/k_2 = 10^5$, they obtained $\tau \sim 10^5$ yr, which is clearly inconsistent with the tilted ring system because the age of the planet is order of Gyr. They also estimated the received flux by the non-tilted ring from the star as 2 % of the maximal flux that the ring can get, and they concluded that the signal from the non-tiled ring is too small to explain the data.

Although they concluded that the non-ringed configuration is favored, their methodology and discussion would be very suggestive for the future detection of the exoplanetary rings.

4.2.3   Formalhaut b

Formalhaut b is a planet that was detected via direct imaging technique for the first time (Kalas et al. 2008). The spectrum of Formalhaut b shows an excess in the visible band. This excess can be explained by a large reflection at a position of the planet. To achieve the large reflection, a very spatially extended configuration is needed. Among several possibilities explaining the large reflection, hypotheses assuming "a planet with a ring" or "a dust cloud" are the most likely. In this subsection, we summarize discussions for and against these two possibilities in the following.

The first possibility is that the planet with a large ring significantly reflects the light from the host star. Kalas et al. (2008) calculated the spectrum of the scatter starlight, and they found that the planet surrounded by the disk with the radius $20R_\mathrm{Jup}$ and the albedo $A_o^r = 0.4$ can explain the observed data well. Even though the visible light can be explained the ring, there are several evidence against this planetary hypothesis. First, there is no infrared flux corresponding to that of the planet (Janson et al. 2012a), so there is no direct evidence of a planet. Moreover, Kalas et al. (2013) found the eccentricity e of Formalhaut b to be 0.8 ± 0.1. In fact, this high eccentricity is inconsistent with the low-eccentric belt around the Fomalhaut if we assume that the Formalhaut b sculpts the belt. This high eccentricity problem might be resolved by considering another planet (Faramaz 2015), but there has been no report on this hypothetical planet. In summary, there are a lot possibilities, but there are no direct evidence of a planet, so the validity of the planetary scenario is still uncertain.

The second possibility is that a dust cloud without a planet largely reflects the light from the star (Kalas et al. 2008). Similarly, there are several discussions against this scenario. In Currie et al. (2012), who reanalyzed this system with the follow-up

observations, found no signs of $0.7 \sim 0.8$ mag variabilities, which are expected for the dust cloud. Currie et al. (2012) concluded that the observed light from the object would mostly come from the small dust while the the upper limit of planetary mass $M < 2M_{\rm J}$, and this doesn't exclude the planetary hypothesis. Moreover, the dust cloud hypothesis has four difficulties in its model (Kalas et al. 2013): (1) observing a rare and short-lived event is unlikely. (2) planetesimal collisions are unlikely far from the star where dynamical timescales are much long ($P \sim 800$ yr). (3) modeling the dimming of the dust cloud requires a fine tuning of the model such that small-grains are quickly depleted from the cloud just as the observations are conducted, and (4) the simulated dust cloud predicts optical colors that do not agree with the observed color. With these observations and discussions, it is difficult to insist on the superiority of the dust cloud hypothesis.

To determine the specific model, the observation of mass of Formalhaut b is crucially important because the dust model expects the very low mass. The mass is considered to be estimated from the observation of the clash of Formalhaut b into the belt in 2032, and it would help us to select one model.

In summary, the discussion about whether Formalhaut b is a planet or not has continues until now, and it is difficult to say Formalhaut b is a ringed planet at current stage.

Chapter 5

Detection methods for exoplanets and expected signals of exoplanetary rings

In this section, we introduce several techniques to detect exoplanets, and discuss the expected signals of the ring for each method. We first consider the techniques applicable to non-transiting planets, and then we discuss the detectability of the ring for transiting planets. In conclusion, the transit photomtery is the most promising method, and the planetary reflection can be another path to the detection of rings around hot planets.

5.1 Around non-transiting planets

In this section, we consider signals of rings around non-transiting planets. The methods include radial velocity techniques, astrometry, gravitational microlensing, and a photometric observation of planetary reflection.

5.1.1 Radial-velocity and astrometric signals of rings

In a planetary system, the planet pulls on the star, so the star also has the orbital velocity. This stellar orbital (radial) velocity appears as the Doppler shift in the stellar spectrum, and the observations of this shift has lead to the detection of over 600 exoplanets as of December 2016.

The semi-amplitude of a radial velocity of a star with a planet is given by

$$K_\star = \frac{28.43229 \text{ ms}^{-1}}{\sqrt{1 - e^2}} \frac{M_\mathrm{p} \sin i}{M_\mathrm{Jup}} \left(\frac{M_\mathrm{p} + M_\star}{M_\odot} \right)^{-1/2} \left(\frac{a}{1\mathrm{AU}} \right)^{-1/2}. \tag{5.1}$$

At first, we cannot expect M_ring to contribute to M_p because the mass of rings M_ring is much smaller than M_p (e.g. $M_\mathrm{ring}/M_\mathrm{p} \sim 10^{-8}$ in case of Saturn). In principle, Keplerian motion assumed in Equation (5.1) can be modulated by the torque from

a ring, and this modulation would show up as an anomaly in the radial velocity. However, these deviations will be much small because even the binary of Jupiter and Jupiter orbiting at 1 AU gives only $10^{-6} \sim 10^{-5}$ ms^{-1} (Morais & Correia 2008). With the typical observed noise in the radial velocity being (~ 1 ms^{-1}), we may conclude that it is unfeasible to probe rings via the radial velocity techniques.

The astrometric motion of the star can be disturbed by the planet, and the typical signal is

$$\alpha = \left(\frac{M_{\mathrm{p}}}{M_{\star}}\right)\frac{a}{d} = 3\mu as \; \frac{m_p}{M_{\oplus}} \left(\frac{M_{\star}}{M_{\odot}}\right)^{-2/3} \left(\frac{P}{1\mathrm{yr}}\right)^{2/3} \left(\frac{d}{\mathrm{pc}}\right)^{-1}. \tag{5.2}$$

For the same reason as that discussed in the radial velocity techniques, the dynamical effect of rings is much tiny, so it is unfeasible to detect rings via astrometry.

5.1.2 Gravitational microlensing signals of rings

A gravitational lens is a matter distribution between a source object and an observer. When the light is emitted from the source, the light is bended by the lens before it reaches the observer, and the image of the source is deformed. Figure 5.1 is the schematic illustration of the gravitational lensing. When a source and lensing object can be approximated by point masses, the overall light curve looks like a symmetric mountain. In addition to the above configuration, if the lensing object has another point mass, the light curve will have an additional feature. Conversely, the anomalous feature in the light curve might imply the point mass, which can be a planet around the star. Thus, the detailed analysis of the light curve will yield the detection of planets. The first planet detected in this method is OGLE 2003-BLG-235/MOA 2003-BLG-53 (Bond et al. 2004), and 52 exoplanets have been detected through this technique as of Dec 2016.

A basic equation of the gravitational lensing is as follows. The bending angle α is given by

$$\alpha(\xi) = \frac{4G}{c^2} \int \Sigma(\xi)\frac{\xi - \xi'}{|\xi - \xi'|^2}\mathrm{d}\xi', \tag{5.3}$$

where $\Sigma(\xi)$ is the surface density at a lens plane, ξ and ξ' are the coordinate values on the lens plane. The value of α relates the original position of the source β with the lensed position θ in the lens equation

$$\beta = \theta - \frac{D_{\mathrm{ds}}}{D_{\mathrm{s}}}\alpha(D_{\mathrm{d}}\theta), \tag{5.4}$$

where D_{ds} and D_{s} are distances from the source to the lens plane and the observer, respectively.

Finally, we consider signals of rings during the microlensing event. As inferred from Equation (5.3), the signals of rings will be very small due to their small mass ($M_{\mathrm{ring}}/M_{\mathrm{p}} \sim 10^{-8}$), so it is unrealistic to expect the lensing effect of rings. Instead, it would be more realistic to expect the photometric effect caused by the gravitational microlensing. For example, if the lensing planet has rings, they will block the light
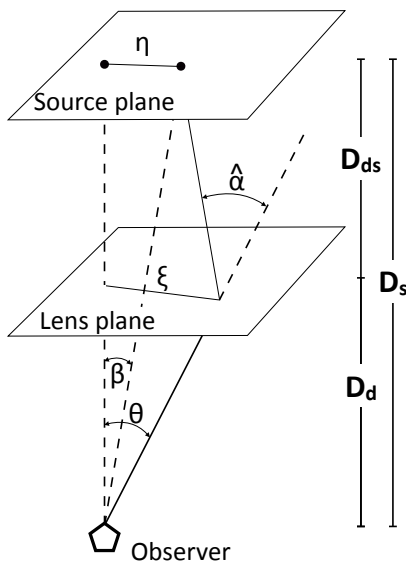
Figure 5.1: Schematic illustration of the gravitational lensing.

of the source image on the lens plane, and the light curve would be disturbed. The similar phenomenon is discussed in Hundertmark et al. (2009) that deals with the lensing effect and the occultation of the circumstellar disk. For another example, if the planet around the source star has rings, the reflection light of rings might be increased to the detectable level with very large aperture (>30m) (Gaudi et al. 2003). In both cases, the expected signal is very low, so it is difficult to probe the rings via the lensing at the current status.

5.1.3 Reflected light from rings

Reflected light from a planet is another probe to characterize the system. It appears in out-of-transit light curves, so called "phase curve", and are potentially found in even non-transiting planets. In addition to the light from the planet, the ring can also contribute to the phase curve.

Arnold & Schneider (2004); Dyudina et al. (2005) investigated the behavior of the reflection of ringed planets systematically. When a planet has a ring, the maximum reflection becomes several times larger than that of a planet alone, and the overall shape of the phase curve also tends to be asymmetric. These features in the real light curve may indicate the rings around the planet.

The amplitude of the reflection of the planet alone is roughly equal to $(R_{\mathrm{p}}/a)^2$ multiplied by the albedo A. For Jupiter-like planets with $R_{\mathrm{p}} = R_{\mathrm{J}}$, the amplitude of reflection is given by $(R_{\mathrm{p}}/a)^2 = 5.7 \times 10^{-4}$ for $a = 0.02$ AU $(R_{\mathrm{p}}/a)^2 = 2.2 \times 10^{-5}$ for a = 0.1 AU, and $(R_{\mathrm{p}}/a)^2 = 9.1 \times 10^{-7}$ for $a = 0.5$ AU. For earth-like planets, the signals

would be smaller that of Jupiter-like planets by two orders of magnitude. Thus, the reasonable targets for the reflection are hot or warm Jupiters. We note that if the planet has a ring, the values of $R_{\rm p}$ and A would effectively increase, so the the total amount of reflection and the observability would be also enhanced.

Around hot or warm Jupiters, the temperature is so high that we naturally expect the rocky rings with low albedo rather than icy rings with high albedo. Specifically, the rocky rings may be several times darker than icy rings. However, the rocky rings can leave the strong signals in back-scattering (Dyudina et al. 2005), and we do not need to exclude the hot planets for the survey of rings.

Naturally, the most promising targets for detecting rings are the planets with their planetary reflection being deteced. To date, using *Kepler* data, Esteves et al. (2015) conducted a comprehensive analysis on planets with $P < 10$ days, and they found 14 planets with significant detections of reflection. On the other hand, Millholland et al. (2016) develops a method to detect the non-transiting planets, and they found one possible candidate around *Kepler* star 5124667. With these samples of the planets, one would search for the rings with the planetary reflection.

In a real analysis, the phase curve includes not only the reflected light but also two other signals; Doppler boosting, and ellipsoidal variations. Thus, to extract planetary reflections alone, we also need to model all of the signals simultaneously.

In conclusion, a reflection from a ring is negligible in most cases although it would be significant around very short-period planets. Although the number of planets with their reflection being detected is small (~ 20 planets), the search for evidence of ring around them such short-period planets might lead to the detection of a planetary ring.

5.2 Around transiting planets

5.2.1 Signals of transiting ringed planet

When a planet has a ring, the apparent size of the system becomes larger, so the depth and the duration of the transit would increase. In a real analysis, however, we do not know to what extent the light curve changes or whether the rings exist or not. Thus, the planetary radius would be overestimated if we interpret the transit of the ringed planet by that of the planet alone. To distinguish between the large planet and the ringed planet, we may focus on the detailed feature in the light curve. Specifically, the residuals from fitting with a ringless model might indicate the signs of rings; if the system has no ring, the fitting will be good, and if the system has a ring, the fitting will be bad. So, the anomalous residuals are the possible signs of rings.

Characters of signals of transiting rings were investigated in several works (Barnes & Fortney 2004; Heising et al. 2015; Ohta et al. 2009). They simulated light curves of ringed planets with various parameters, and fit the ringless model to these simulated data. In their simple model, the rings are characterized by five parameters; two for the size, two for the obliquity, and one for the transparency of the ring. Barnes & Fortney (2004) found that the Saturn-like rings typically gives the residuals larger than 10^{-4},

which is the typical noise level of *Kepler*. This result greatly encourages the search for rings with *Kepler* data.

In addition, there is a general relation between the obliquity and signals of rings. When the rings are edge-on, there are no signals of rings. As another limit, when the rings are face-on, it tends to give the small signals. Instead, when the the obliquities are in the intermediate regime, the signals of the ring are large. This is because in such regime, the ring is tilted well, so the apparent form of the ringed planet clearly deviates from a circle expected for a ringless planet. Thus, the tilted ring like Saturnian rings are easy to detect while the small tilted ring expected around the hot planets are difficult to observe. However, the above discussion talks about a tendency, and, in reality, Heising et al. (2015) found that the ringed planet with small obliquity has a potential to give the small but observable signals. In addition, even if the planet is near the star, the obliquity can be high thanks to Cassini state. Thus, in reality, we do not need to exclude the hot planets from the targets of the search for rings.

Given the detectability of rings and the large number of transiting planets revealed by *Kepler*, the transit photometry would be the most promising path to finding a first exoplanetary ring. Especially, in addition to cold planets like Saturn, hot planets can be the possible targets for the ring-search. So far, Heising et al. (2015) conduced a search for rings among 21 hot planets. They found no evidence of rings, and their results are consistent with the simple expectation that the rings are difficult to observe around hot planets. For the further understanding of the frequency of exoplaentary rings, we would need a systematical survey exploiting all the existing data.

Finally, we note that unlike the reflected light, the signals of the ring in a transit method are irrelevant to the distance from the star to the planet. Thus, in principle, it is possible to detect any ring systems around any distant planets.

5.2.2   Spectroscopic observation of ringed planet during transit

Spectroscopic observations give another independent and complimentary evidence of rings detected by the photometric observation. Since these two methods use different instruments, they would suffer from the different noises and systematics. In this sense, the spectroscopic observation would play a role in increasing the reliability of the detection of rings.

When we observe a star spectroscopically, we would obtain broad and symmetric line profiles due to the stellar spin. In addition to the stellar spin, if there also occurs a planetary transit, the symmetric stellar line profile would be distorted during the transit. This distorted effect is called Rossiter effect, which gives a important parameter characterizing the architecture of the planetary system; a projected spin-orbit angle λ (e.g. McLaughlin 1924; Ohta et al. 2005; Rossiter 1924). The extent of the distortion totally depends on the occulting object, and this is the reason why we can distinguish between the ringless object and the ringed object.

The radial velocity anomaly due to the Rossiter effect is given by

$$\Delta v_s = -\Omega_s \sin I_s \frac{\int\int x I_s(x,y) D(x,y) dx dy}{\int\int I_s(x,y) D(x,y) dx dy},$$ (5.5)

where $D(x,y)$ is the transmission fraction of light coming from the location of the stellar disk (x,y), I_s is the stellar intensity model, Ω_σ is the spin angular velocity, and $\sin I_s$ is the inclination angle between angle between the stellar spin axis and the line of sight. The distortion of the line profile is determined by the occulting object in the form of $D(x,y)$. In case of a transit of a ringless planet. Ohta et al. (2005) gave the analytical formula for Equation (5.5). In case of a ringed planet, Ohta et al. (2009) gave the analytical formula for only the face-on rings, but there has been no analytical formula for any obliquity.

Ohta et al. (2009) discussed the spectroscopic signals of rings in a realistic situation. Indeed, they found that the spectroscopic signature of Saturnian ring is a little below the detection threshold under the noise $v = 1$ m/s. However, the signature would increase as the number of the data increases, and the spectroscopic signals are completely complement to the photometric signals of rings, so it will enhance the reliability of the detection of rings. Moreover, the precision of the radial velocity is expected to improve in the future. Thus, in the future, the spectroscopy would play an important role in following-up the detected ringed object.

5.2.3 Statistical way of detecting rings in transit photometry

Zuluaga et al. (2015) proposed a way to statistically detect rings via transit photomtery, and we summarize their discussion here.

First, they gave the analytical expression of the transit depth and transit duration for the ringed planet. They estimated the total area of the ringed planet A_{Rp}:

$$A_{\mathrm{Rp}} = \pi R_{\mathrm{p}}^2 + \pi[r^2(f_e) - r^2(f_i)]R_{\mathrm{p}}^2,$$ (5.6)

where r is the effective ring radius and is given by

$$r^2(f) = \begin{cases} (1 - e^{-\tau/\cos i_{\mathrm{R}}})(f^2 \cos i_{\mathrm{R}} - 1) & (f\cos i_{\mathrm{R}} > 1), \\ \frac{\pi(1-e^{-\tau/\cos i_{\mathrm{R}})}}{2}\left[(f^2 \cos i_{\mathrm{R}} \arcsin\left(\frac{\sqrt{f^2-1}}{f\sin i_{\mathrm{R}}}\right) - \arcsin\left(\frac{\cos i_{\mathrm{R}}\sqrt{f^2-1}}{\sin i_{\mathrm{R}}}\right)\right] & (\text{otherwise}). \end{cases}$$

Here, i_{R} is the projected ring inclination, $y = \sqrt{f^2-1}/(f\sin i_{\mathrm{R}})$, and the outer ring radius and inner ring radius are given by $R_{\mathrm{out}} = f_e R_{\mathrm{p}}$ and $R_{\mathrm{out}} = f_i R_{\mathrm{p}}$ respectively. On the assumption of the the constant stellar surface brightness, the transit depth δ is given by

$$\delta = \frac{A_{\mathrm{Rp}}}{\pi R_\star^2}.$$ (5.7)

When a planet has a ring, the transit depth is enhanced due to the ring, so the observed normalized planetary radius $p_{\mathrm{obs}} = R_{\mathrm{p,obs}}/R_\star = \sqrt{\delta}$ differs from the real

radius $p = R_{\rm p}/R_\star$. In the same way, the transit durations $T_{\rm tot}$ and $T_{\rm full}$ are biased due to the rings. To evaluate this anomaly quantitatively, they approximately gave the anlalytical expressions of $T_{\rm tot}$ and $T_{\rm full}$ for the ringed planet.

For the fiducial case, Zuluaga et al. (2015) considered the ringed planet with $R_{\rm p} = 0.0836R_\odot$, $f_{\rm i} = 1.58$, and $f_{\rm e} = 2.35$. In calculation, they assumed that the planetary orbit is circular, and the plant is at $a = 1$ AU. For ring axes, they considered two probability distributions of obliquities. One is a uniform and random distribution, and the other is fisher distribution with $\kappa \sim 8$ and 2σ obliquity dispersion of $\sim 30°$, which predominantly makes low obliquities.

First, they consider the bias onto $p_{\rm obs}/p$. The distribution of uniform random obliquities gives the broad range of $p_{\rm obs}/p$, and more than 50 % configurations give $p_{\rm obs} > 1.5p$. In case of the distribution of the low obliquities, the most of the configurations ($\sim 80\%$) give $p_{\rm obs} > 1.2p$ while the distribution concentrates around $p_{\rm obs}/p = 1$. In both distributions, the value of p is significantly biased due to the ring. Given this result, one viable strategy of detecting rings is to reanalyze the light curves of eclipsing binaries because they might be just misclassified as the binary due to the bias of the ring.

The overestimation of the planetary radius due to the ring would lead to the underestimation of the planetary density. Actually, there are anomalously low density planets (e.g. in Kepler 51 (Masuda 2014)) characterized by TTV (Transit Timing Variations) observations. While these low density planets are considered to be explained by the planetary formation theories as stated in Masuda (2014), we may note that these anomalous plants might be explained by the ring around the planet.

Next, we consider the anomaly in $\rho_\star/\rho_{\rm obs}$ due to the rings. For this purpose, let us recall the relation (Seager & Mallen-Ornelas 2003, e.g.) in a circular orbit:

$$\left[\frac{a}{R_\star}\right]_{\rm obs} \sim \frac{P}{2\pi} \frac{\delta^{1/4}}{(T_{\rm tot}^2 - T_{\rm full}^2)^{1/2}}. \tag{5.8}$$

When the planetary mass is negligible, the Kepler's third law gives

$$\rho_{\star,{\rm obs}} = \frac{3\pi}{G} \frac{(a/R_\star)_{\rm obs}^3}{P^2}. \tag{5.9}$$

When the planet has rings, the estimated stellar density in Equation (5.9) will be deviated from the true values because δ, $T_{\rm tot}$, and $T_{\rm full}$ are changed due to rings. In the same way as in $p_{\rm obs}/p$, Zuluaga et al. (2015) investigated the observational effect of the ring onto $\rho_{\rm obs}/\rho_\star$ for two distributions of obliquities. The $\rho_{\rm obs}/\rho_\star$ distribution of the random obliquity distribution is peaked around $\log_{10} \rho_{\rm obs}/\rho_\star \sim -0.2$. On the other hand, the $\rho_{\rm obs}/\rho_\star$ distribution derived from the edge-on concentrated distribution has the peak of $\log_{10} \rho_{\rm obs}/\rho_\star \sim -0.5$. Thus, in both distributions, the observed stellar density potentially changes significantly. The anomaly in the stellar density might be revealed by the comparison of the stellar density from transit photometry and that estimated from other techniques (asteroseismology and stellar models). Indeed, however, the estimated $\rho_\star$ from transit photometry also depends on e individually.

Thus, to discuss the ring from the stellar density, we need to solve the degeneracy of e and the rings. The increase in e increases $\rho_{\star,\mathrm{obs}}$ while the additional transit of the ring decreases $\rho_{\star,\mathrm{obs}}$. Therefore, the negative value of $\rho_{\star,\mathrm{obs}}$ would be the sign of the ring.

Chapter 6

Stability and obliquity of rings and their implications of search for rings

Stability and obliquity of rings depend on planetary environment. For example, if a planet orbits close to a central star, the rings composed of ice would disappear. In this section, we consider these effects, and determine our targets for a survey of rings. The materials in this section basically follow Schlichting & Chang (2011).

6.1 Melting temperature

High temperature leads to the depletion of rings. This melting temperature depends on the materials; icy materials are unstable if $T > 170$ K, and SiO2 materials are unstable if $T > 1700$ K. Equating these melting temperatures with the effective temperature of planets, we obtain the the critical semi-major axes, over which the rings would disappear;

$$a = \left(\frac{L_\star}{16\pi\sigma T_{\text{sub}}^2} \right) = 2.7 AU \left(\frac{L_\star}{L_\oplus} \right) \left(\frac{170\text{K}}{T_{\text{sub}}} \right)^2 = 0.027 AU \left(\frac{L_\star}{L_\oplus} \right) \left(\frac{1700\text{K}}{T_{\text{sub}}} \right)^2, \quad (6.1)$$

where we assume sublimation of ice in the middle, and that of silicate in the last. These values imply that most of the transiting planets are able to have silicated rings while they are unlikely to have icy rings. Quantitatively, *Kepler* catalog on 12/12/2016 lists 4381 transiting planet candidates with the effective temperatures $T_{\text{eff}} < 1700$ K, and 16 planets with $T_{\text{eff}} < 170$ K.

6.2   Poynting-Robertson Drag

6.2.1   Effect on ring

Small particles are significantly affected by radiation. In the context of rings, the main effect caused by radiation is "Poynting-Robertson Drag". Let us assume the particles orbits around the hot object (star or planet in our mind). In the meantime, the particle is always radiated by the central object, and they reemit the received energy at the same time. During the emission, they release the light anisotropically due to its relativistic motion, and this anisotropy causes the anisotropic back-reaction to the particle. This back-reaction loses the angular momentum of the particle as well as the semi-major axis, and it behaves like "Drag". This is why this process is called Poynting-Robertson "Drag".

The timescale for an orbital decay due to Poynting-Robertson Drag is given by

$$t_{\mathrm{PR}} \simeq \frac{8\rho s c^2}{3(L/4\pi a^2)Q_{PR}(5+\cos^2 i)}, \tag{6.2}$$

where c is the speed of light, L is the stellar luminosity, i is the inclination of the ring plane with respect to the orbital plane, Q_{PR} is the efficiency factor of the radiation pressure, s is the diameter of a particle, and ρ is the density of the particle (Burns et al. 1979). In case of rings of Jupiters, $t_{\mathrm{PR}} \simeq 10^5 s$ years, where s is in unit of μ (Burns et al. 1999). This short timescale is not inconsistent with the existence of Jovian rings because Jovian satellite constantly supply their ejected particles to its ring system.

Equation (6.2) describes Poynting-Robertson Drag for one particle. On the other hand, when the rings are optically thick, t_{PR} is modified because light strikes only part of rings. Schlichting & Chang (2011) derived t_{PR} for optically thick rings in the form of

$$t_{\mathrm{PR}} \simeq \frac{\pi c^2 \Sigma}{\sin i (L/4\pi a^2)Q_{PR}(5+\cos^2 i)}, \tag{6.3}$$

where Σ is the mass surface density for the ring. Σ, so even if each particle has short lifetime in Equation (6.2), they can survive against the radiation if they collectively make the optically thick ring.

6.2.2   Derivation of time scale of Poynting-Robertson Drag

In this section we derive Equation (6.2) following the heuristic derivation in Burns et al. (1979). Let us consider a particles with mass m and a geometrical corss-section A orbiting around a star at a velocity $\boldsymbol{v}$. We assume that the star gives the flux $\boldsymbol{S}$ to the particle. The effective flux $\boldsymbol{S'}$ received by the particle differs from $\boldsymbol{S}$:

$$\boldsymbol{S'} \simeq \boldsymbol{S}(1 - \dot{r}/c), \tag{6.4}$$

where we use the radial velocity $\dot{r} = \boldsymbol{v} \cdot \boldsymbol{S}$. Once the particles receives the energy, it will emit the same amount of energy $S'A$ via photon emission. In the rest frame of

the particle, it will emit the energy $S'A$ or the effective mass $S'A/c^2$ isotropically. In the rest frame of the star, this mass loss $S'A/c^2$ leads to the loss of the momentum $(S'A/c^2)\boldsymbol{v}$ of the particles. In total, EoM for the particle is given by

$$m\dot{\boldsymbol{v}} \simeq (S'A/c)\hat{\boldsymbol{S}} - (S'A/c^2)\boldsymbol{v} \simeq (SA/c)[(1 - \dot{r}/c)\hat{\boldsymbol{S}} - \boldsymbol{v}/c], \qquad (6.5)$$

where $\hat{\boldsymbol{S}}$ is the corresponding unit vector of $\boldsymbol{S}$. In fact, there is another derivation of the effect of the back reaction in Equation (6.5). Let us see the received flux as the mass loading $\Delta m = S'A/c^2$ onto the particle. Then, the velocity of the particle is decreased to $\boldsymbol{v} + \Delta\boldsymbol{v}$. To conserve the momentum, one obtains the relation $\Delta m\boldsymbol{v} = -m\Delta\boldsymbol{v}$. Therefore, the loss of the momentum is

$$\Delta p = m\Delta\boldsymbol{v} = -(S'A/c^2)\boldsymbol{v}. \qquad (6.6)$$

In the expression of Equation (6.5), we implicitly assumes the perfectly absorbing particles. In reality, however, the particle not only absorb but also scatters the light. Specifically, the particle will scatter an amount of light effectively received by the area AQ_{sca}, and absorb that received by AQ_{abs}. Here, Q_{sca} and Q_{abs} are defined as scattering and absorption coefficients, respectively. Actually, these values depend on the wavelength, but we consider the averaged values of them over the considered spectrum. Using these values, we define the radiation pressure coefficient as

$$Q_{\mathrm{pr}} = Q_{\mathrm{abs}} + Q_{\mathrm{sca}}(1 - <\cos\alpha>), \qquad (6.7)$$

where α is the angle between the $\boldsymbol{S}$ and $\boldsymbol{v}$, and $<\cos\alpha>$ is the average value of $\cos\alpha$ in the distribution of the reemitted light, which describes the extent of an anisotropy. The scattering modifies EoM of the particle in Equation (6.5) into the following:

$$m\dot{\boldsymbol{v}} \simeq (SA/c)Q_{\mathrm{pr}}[(1 - \dot{r}/c)\boldsymbol{S} - \boldsymbol{v}/c], \qquad (6.8)$$

where the difference from Equation (6.5) is the factor of Q_{pr}.

To calculate $\dot{a}$, we consider the works by the drag in Equation (6.8) on the planetocentric particle. Let us define $\hat{\boldsymbol{a}}$ as the unit vector from a planetary center to a pericenter and a unit vector $\hat{\boldsymbol{b}}$ as the vector that lies on a orbital plane and is perpendicular to $\hat{\boldsymbol{a}}$. We also define $\boldsymbol{a} = a\hat{\boldsymbol{a}}$ and $\boldsymbol{b} = a\sqrt{1 - e^2}\hat{\boldsymbol{b}}$. In this notation, the position of the particle is given by $\boldsymbol{r} = \boldsymbol{a}(\cos f - e) + \boldsymbol{b}\sin f$, and its velocity is given by

$$\boldsymbol{v} = \dot{f}(-\boldsymbol{a}\sin f + \boldsymbol{b}\cos f). \qquad (6.9)$$

In Equation (6.8), the terms including $\boldsymbol{v}$ only contributes the total work. The rate of change of the orbital energy of the particle is given by

$$\dot{E} = -(SA/c)Q_{\mathrm{pr}}((\boldsymbol{v}\cdot\hat{\boldsymbol{S}})^2 + \boldsymbol{v}\cdot\boldsymbol{v}) \qquad (6.10)$$

$$= -(SA/c)Q_{\mathrm{pr}}\dot{f}^2[(\boldsymbol{a}\cdot\hat{\boldsymbol{S}})^2\sin^2 f + (\boldsymbol{b}\cdot\hat{\boldsymbol{S}})^2\cos^2 f \qquad (6.11)$$

$$- 2(\boldsymbol{a}\cdot\hat{\boldsymbol{S}})(\boldsymbol{b}\cdot\hat{\boldsymbol{S}})\sin f\cos f + a^2(1 - e^2\cos^2 f)]. \qquad (6.12)$$

By averaging Ω, ω, and f, we obtain

$$<\dot{E}> = -(SA\mu/4ac^2)Q_{\text{pr}}(5 + \cos^2 i). \qquad (6.13)$$

With Equation (6.13) and the relation $<\dot{a}> = 2a^2<\dot{E}>/\mu m$, we obtain

$$<a\dot{a}> = -(3S_0/8R^2c^2)(Q_{\text{pr}}/\rho s)(5 + \cos^2 i). \qquad (6.14)$$

By integrating Equation (6.14) to obtain the decay time $a \to 0$, we finally obtain Equation (6.2).

6.3 Obliquity damping

6.3.1 Effect on ring

Tides raised on an exoplanet by a host star diminishes a planetary obliquity $\theta_\star$ and the detectability of rings. Here, we define the planetary obliquity $\theta_\star$ as an angle between an orbital axis and a planetary spin axis. From the tidal theory, this damping time scale is given by

$$t_{\text{damp}} = \theta_\star \frac{dt}{d\theta_\star} = \frac{2\alpha_p Q_p}{3k_p} \left(\frac{M_p}{M_\star}\right) \left(\frac{a}{R_p}\right)^3 \Omega^{-1}, \qquad (6.15)$$

where k_p is the Love number, Q_p is the tidal dissipation function. $M_\star$, M_p, R_p, and a are the stellar mass, the planetary mass, the planetary radius, and the semi major axis. We also define a new parameter $\alpha_p = I_p/M_p R_p^2$, where I_p is the planet's moment of inertia and Ω is the orbital period.

Let us assume that we observe the ringed planet via transit photometry. If the axis of this planetary ring is aligned with the orbital axis due to damping of the obliquity, the inclination of the planetary rings should be nearly perpendicular to the line of sight because an orbital inclination of the transiting planet should be nearly equal to $90°$. In such a case, the apparent size of the planetary rings becomes very small, and the signals of them would be small. Thus, the ringed planet with a tidal damping obliquity would be difficult to show its signal of the rings.

The value of t_{damp} crucially depends on the tidal dissipation function Q. Gas giant planets like Jupiter have large $Q \simeq 10^6$ while rocky planets have relatively small $Q \simeq 10^2$. This means that the tidal dissipation efficiently occurs around the rocky planets, and it is not the case for the gas giant planets. This fact is is also consistent with the tilted ring of Saturn. For the typical value, assuming $Q \simeq 10^{6.5}$ and $k_p \sim 3/2$, we obtain $t_{\text{damp}} \sim 10^8$ and $t_{\text{damp}} \sim 10^9$ for $a = 0.1$ AU and $a = 0.2$ AU, respectively.

Even if the timescale of a tidal damping is short, the rings can have a enough obliquity to be detected via transit photometry. For example, it is known that the planet with the initial high obliquity potentially settles into the Cassini state, where the planetary spin axis remains tiled. Moreover, even if the planetary obliquity is damping, the ring axis can be tilted enough when the transiting planet is very close to its host star (Heising et al. 2015). For example, Brown et al. (2001) succeeded in

giving the upper limit to the ring to the hot Jupiter HD 209458 assuming its ring axis to be alined with the orbital axis.

In summary, we may ignore the tidal damping for the distant gas giant planets. In addition, even if t_{damp} is very short compared with the age of the system, there also exits possibility we can observe the rings via transit photometry.

6.3.2   Derivation of tidal damping time scale

In this section, we explains the derivation of Equation (6.15). Based on the "viscous" approach of the equilibrium tide theory (Levrard et al. 2007), the secular evolutions of the planetary spin are given by

$$\frac{d\omega}{dt} = -\frac{K}{Cn}\left[(1+x^2)\Omega(e)\frac{\omega}{n} - 2xN(e)\right], \tag{6.16}$$

$$\frac{d\epsilon}{dt} = \sin\epsilon\frac{K}{C\omega n}\left[x\Omega(e)\frac{\omega}{n} - 2N(e)\right], \tag{6.17}$$

with

$$\Omega(e) = \frac{1 + 3e^2 + (3/8)e^4}{(1-e^2)^{9/2}}, \quad N(e) = \frac{1 + (15/2)e^2 + (45/8)e^4 + (5/16)e^6}{(1-e^2)^6}, \tag{6.18}$$

where ω is the planet's rotation rate, ϵ is the obliquity (the angle between the orbital planet and the equilateral plane), $x = \cos\epsilon$, C is the polar moment of inertial, and K is defined as

$$K = \frac{3}{2}\frac{k_2}{Q}\left(\frac{GM_p^2}{R_p}\right)\left(\frac{M_\star}{M_p}\right)^2\left(\frac{R_p}{a}\right)^6 n. \tag{6.19}$$

To the order of e and ϵ, Equations (6.16) and (6.17) are reduced to

$$\frac{d(\omega - n)}{dt} \simeq -\frac{2K(\omega - n)}{Cn^2}, \tag{6.20}$$

$$\frac{d\epsilon}{dt} \simeq \epsilon\frac{K}{C\omega n}\left[\frac{\omega - 2n}{n}\right]. \tag{6.21}$$

From Equation (6.20), the damping timescale for $\omega \to n$ is given by

$$t_\omega = \left|\frac{\omega - n}{\frac{d(\omega - n)}{dt}}\right| = \frac{Cn^2}{2K}. \tag{6.22}$$

Assuming $t_\epsilon \simeq t_\omega$, we obtain Equation (6.15) combining $t_\omega = Cn^2/2K$ and Kepler's law $n^2 \simeq (GM_\star/a^3)$;

$$t_\epsilon \simeq \frac{Cn^2}{2K} \simeq C\frac{GM_\star}{a^3}\frac{2}{3}\frac{Q}{k_2}\left(\frac{R_p}{GM_p^2}\right)\left(\frac{M_p}{M_\star}\right)^2\left(\frac{a}{R_p}\right)^6\frac{1}{n} \tag{6.23}$$

$$= \frac{2\alpha_p Q}{3k_2}\left(\frac{M_p}{M_\star}\right)\left(\frac{a}{R_p}\right)^3\frac{1}{n}. \tag{6.24}$$

The damping timescale for $\epsilon \to 0$ depends on the value of ω. First, let us assume that several times of t_ω already passes. Then, ω becomes nearly equal to n, and Equation (6.21) is reduced to

$$\frac{d\epsilon}{dt} \simeq -\epsilon \frac{K}{Cn^2}, \tag{6.25}$$

Thus, the damping timescale of the ϵ is equal to $2t_\omega$. Second, if we initially assume $\omega \ll n$, Equation (6.21) is reduced to

$$\frac{d\epsilon}{dt} \simeq -\epsilon \frac{2K}{Cn\omega} = -\epsilon \left(\frac{2n}{\omega} \right) \left(\frac{Cn^2}{K} \right). \tag{6.26}$$

Thus, in the limit of $\omega \ll n$, t_ϵ becomes $\omega/2n$ smaller than that in $\omega \simeq n$.

6.4 Roche radius and Hill radius

Within the region with the radius being Roche radius R_{roche}, the satellite cannot retain its form. This leads to the tidal disruption and formation of the ring. Thus, R_{roche} is important information about the size of the ring.

In a case of a rigid satellite, R_{roche} is given by

$$\frac{R_{\mathrm{roche}}}{R_p} = 1.26 \left(\frac{\rho_p}{\rho} \right)^{1/3}, \tag{6.27}$$

where ρ_{p} is the planetary density and ρ is the density of the satellite. In a case of a fluid dynamics, the factor in the equation is a little modified in the following way:

$$\frac{R_{\mathrm{roche}}}{R_p} = 2.45 \left(\frac{\rho_p}{\rho} \right)^{1/3}. \tag{6.28}$$

For example, Saturnian rings are mainly composed of ice with the average density $\rho = 0.5 \sim 0.9$ gcm^{-3}, and its planetary density is $\rho_{\mathrm{p}} \simeq 0.7$ gcm^{-3}, thus we expect $1.75 R_{\mathrm{p}} < R_{\mathrm{roche}} < 3.15 R_{\mathrm{p}}$. This range of R_{roche} is consistent with the size of Saturnian ring $1.5 R_{\mathrm{p}} \sim 2.0 R_{\mathrm{p}}$. In the context of exoplanetary rings, we do not know ρ_{p} and ρ a priori, so we cannot use R_{roche} to reduce the realistic parameter space. Instead, we can use it for constraining ρ_{p}/ρ from the observed ring system.

For an object orbiting around a planet, it should be within Hill radius R_{Hill}:

$$R_{\mathrm{Hill}} = a \left(\frac{M_{\mathrm{p}}}{M_\star} \right)^{1/3}. \tag{6.29}$$

The radius R_{Hill} determines the region, where the object stably orbits around the planet. Thus, large R_{Hill} leads to the large number of captured objects and the large possibility of ring formations. In addition, when $R_{\mathrm{Hill}} < R_{\mathrm{roche}}$, rings can be unbound to the planet even if the rings are formed.

In fact, the radius, which determines the stable orbits, is two to three times smaller than R_{Hill}. In detail, a prograde motion gives the factor of the three, and the retrograde motion gives the factor of two, so the retrograde object has a stabler orbit. This is one reason why the giant ring candidate around J1407b favors the retrograde orbit (Rieder & Kenworthy 2016).

Finally, We derive Equation (6.27). We take a system to be composed of a planet with mass M_{p} and a satellite with mass M_{s} and radius r at a distant of a from the planet. In addition, we consider a small object with mass u on the satellite surface at the opposite side of the planet. The force onto the mass u from a satellite gravity is given by $GM_{\mathrm{s}}u/r^2$. The mass u is also affected by the tidal force $2GM_{\mathrm{p}}ur/a^3$ to the leading order. While the satellite gravity moves the object toward the satellite center, the tidal force tends to pull it apart. By equating the these two forces, we obtain the critical radius, over which the object with u is no longer stable;

$$GM_{\mathrm{s}}u/r^2 = 2GM_{\mathrm{p}}ur/a^3 \;\;\rightarrow\;\; a^3 = 2R_{\mathrm{p}}\frac{\rho_{\mathrm{p}}}{\rho}, \tag{6.30}$$

where a is equal to R_{roche} in Equation (6.27). The value of R_{Hill} in Equation (6.29) is derived in the same way as the above.

6.5 Laplace radius

An axis of Saturnian rings is aligned with the planetary spin axis. This is because the tide from the planetary oblateness is dominant. However, when the planet is near its host star, the stellar tide can be dominant far from the planet, and the rings far from the planet would be on the orbital plane of the planet. Thus, the direction of the ring axis is determined by the balance of the tidal force of the planetary oblateness and the stellar tides.

The strength of the quadrupole potential due to the planetary oblateness is

$$\Phi_{\mathrm{p}} = \frac{GM_{\mathrm{p}}J_2R_{\mathrm{p}}^2}{r^3}P_2(\cos\theta), \tag{6.31}$$

where θ is the angle between the planetary spin axis and the ring axis, J_2 is the quadrupole gravitational harmonic, and P_2 is a Legendre Polynomial. The quadrupole potential due to the stellar tides is given by

$$\Phi_{\star} = \frac{GM_{\star}r^2}{2a^3(1-e)^{3/2}}P_2(\cos\theta_{\star}), \tag{6.32}$$

where $\theta_{\star}$ is the angle between the orbital axis and the ring axis. The balance of the tidal forces is determined by the ratio of the potentials in Equations (6.31) and (6.32),

and Laplace radius R_{L} is defined as r satisfying $\Phi_{\mathrm{p}} = \Phi_{\star}$;

$$R_{\mathrm{L}} = \left(2 J_2 R_{\mathrm{p}}^2 a^3 (1-e)^{3/2} \frac{M_{\mathrm{p}}}{M_{\star}} \right)^{1/5} \tag{6.33}$$

$$= R_{\mathrm{p}} \left(\frac{a/4\ \mathrm{AU}}{R_{\mathrm{p}}/R_{\oplus}} \right)^{3/5} \left(\frac{J_2}{0.001} \right) \left(\frac{M_{\mathrm{p}}/M_{\star}}{3 \times 10^{-6}} \right)^{1/5} (1-e)^{3/10} \quad (\text{Earth}), \tag{6.34}$$

$$= R_{\mathrm{p}} \left(\frac{a/0.017\ \mathrm{AU}}{R_{\mathrm{p}}/R_{\mathrm{J}}} \right)^{3/5} \left(\frac{J_2}{0.01} \right) \left(\frac{M_{\mathrm{p}}/M_{\star}}{0.001} \right)^{1/5} (1-e)^{3/10} \quad (\text{Jupiter}), \tag{6.35}$$

where $J_2 = 0.01$ is the typical value for Saturn and Jupiter, and $J_2 = 0.001$ for Earth and Mars.

Roughly speaking, the ring axis will be aligned with the planetary spin axis when $r < R_{\mathrm{L}}$, and aligned with the orbital axis $r > R_{\mathrm{L}}$. This fact is seen in rings of Saturn. Indeed, almost all of Saturnian rings are on the equatorial plane. However, Phoebe ring at a distant of 200 R_{p} from the center is on the orbital plane of the planet rather than its equatorial plane (Verbiscer et al. 2009).

The rings in $r > R_{\mathrm{L}}$ are hard to detect transiting planets due to the low obliquities. Actually, in case of exo-Earth in Equation (6.34), all of the rings would be on the orbital plane unless it has $a > 4$AU. This means even if the exo-Earth with $a < 4$ AU has a giant ring, they leave little signals on the observation because they are nearly edge-on. On the other hand, in case of Jupiter in Equation (6.35), R_{L} is larger than R_{p} in almost all cases. Thus, the rings around the gas giant are more likely to be probed than those around the rocky planets. Incidentally, after the time t_{damp} in Equation (6.15), the obliquity is ultimately damped, so the rings with $r < R_{\mathrm{L}}$ also become difficult to detect.

We note that the above discussions only consider equilibrium states of rings. In fact these discussions cannot be applied when the rings are in a transitional phase like J1407b. Thus, we do not need to mind the value of R_{L} when we search for transitional rings.

6.6   Target selection for ring search

Summarizing the contents in this section, rings are likely detectable when the following conditions are satisfied; T is low enough, t_{PR} is long enough, t_{damp} is long enough, R_{Hill} and R_{roche} are large enough, and R_{L} is large enough. To satisfy all these conditions, the planets should be distant from the host stars and have large J_2. Thus, the distant gas giants are the best targets for a survey.

In Chapter 5, we show that the best method to detect rings is a transit method. Therefore, we select the transiting distant planets as targets objects for our ring search. Especially, in this thesis, we focus on the planets detected by *Kepler* because it gives the largest sample of planets. Considering that the temperature of the snow line is 170 K (Hayashi 1981), we choose 37 KOIs whose equilibrium temperatures are less than 200 K. In addition, we selected planet candidates reported by recent transit surveys;

41 candidates from a search by Wang et al. (2015) and 28 candidates from our group (Uehara et al. 2016). In Table 6.1, the numbers of planetary candidates in three groups are listed with the number of transits.

We exclude several systems, which are not suited for our search. For KOI-5574.01 in KOIs and KIC 2158850 in Wang et al. (2015), we cannot find the transit signal among the noisy light curves. For KOI-959.01 in KOIs with $P = 10$ days and KIC 8540376 in Wang et al. (2015) with $P = 31.8$ days, we cannot neglect the binning effect due to the short transit duration. After removing these systems, 89 planet candidates are left in total for our search. Tables 6.1 summarizes the number of targets, and Figure 6.1 shows the overlapped objects among KOIs, Wang et al. (2015), and Uehara et al. (2016)

Table 6.1: Number of planet candidates in three groups.

Group	Number of systems			Total number of candidates
	One transit	Two transits	more than two transits	
KOIs ($T_{eq} \leq 200$ K)	5	2	30	37
Wang et al. (2015)	17	14	10	41
Uehara et al. (2016)	28	0	0	28
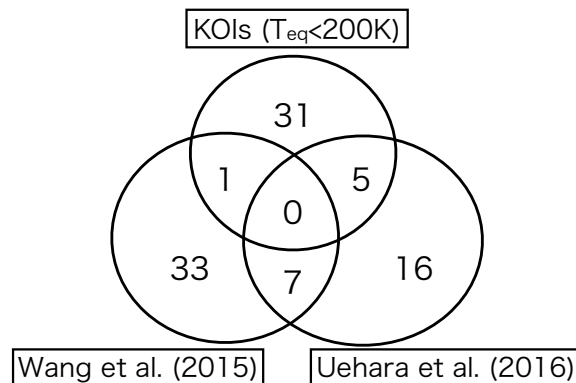
Figure 6.1: Venn diagram for target objects corresponding to Table 6.1.

Although we consider only the long-period planets in this thesis, we note that there also exists possibility that silicate rings can be detected around short-period plants. Quantitatively, Schlichting & Chang (2011) finds no compelling reason against the detection of rings around the planets within 0.1 AU from Solar-like stars. In the future, we plan to conduct a search around such short-period planets.

Chapter 7

Towards detection of exoplanetary rings via transit photometry: methodology and a possible candidate

7.1 Summary of previous chapters and introduction to this chapter

As is the case of the Solar system, moons and planetary rings are believed to exist in exoplanetary systems as well. Their detection, however, has not yet been successful, and remains as one of the most attractive, albeit challenging, goals in exoplanetary sciences. A notable exception includes a system of giant circumplanetary rings of J1407b (e.g. Kenworthy & Mamajek 2015) discussed in Section 4.2.1, but the inferred radius ~ 1 AU implies that it is very different from Saturnian rings that we focus on in the present thesis.

In addition to the obvious importance of the ring discovery itself, its detection offers an interesting method to determine the direction of the planetary spin because the ring axis is supposed to be aligned with the planetary spin as in the case of Saturn. Thus the detection of ring parameters yield a fairly complete set of dynamical architecture of transiting planetary systems; the stellar spin via asteroseismology (e.g. Benomar et al. 2014; Huber et al. 2013) and gravity darkening (e.g. Barnes et al. 2011; Masuda 2015), the planetary orbit via transiting photometry and the Rossiter-McLaughlin effect (e.g. Ohta et al. 2005; Queloz et al. 2000), and the planetary spin through the ring detection as discussed here.

The direct detection of planetary spin is very difficult, and so far only four possible signals related to planetary spins have been reported: the periodic flux variations of 2M1207b (Zhou et al. 2016), and a rotational broadening and/or distortion of the line profile of β Pictoris b (Snellen et al. 2014), HD 189733b (Brogi et al. 2016), and GQ Lupi b (Schwarz et al. 2016). These interesting planets are very young and have

sufficiently high temperature (> 1600 K) for their spin to be detected. In contrast, the same technique is not easily applicable for mature and cold planets like Saturn. Thus the detection of the ring axis provides a complementary methodology to determine the spin of more typical planets with low temperature.

Since the total mass of planetary rings is small, they do not exhibit any observable signature on the dynamics of the system. Instead, high-precision photometry and spectroscopy offer a promising approach towards their detection, and, observations of reflected light and transit are especially useful for this purpose as discussed in Section 5.

Possible signatures in reflected light due to the planetary rings include the higher brightness, the characteristic phase function, distinctive spectral variations, temporary extinction of the planet, and discrepancy between reflection and thermal radiation intensities (e.g. Arnold & Schneider 2004; Dyudina et al. 2005) (also discussed in Section 5.1.3). For instance, as discussed in Section 4.2.2, Santos et al. (2015) attempted to explain the line broadening of the reflected light of 51 Peg b with a ringed planet model, and they conclude that it is not due to the ring. This is because their solution requires a non-coplanar configuration, which would be unlikely for short-period planets. As we see in Section 5.1.3, searches for rings through the light reflection of the host star can be made for non-transiting planets even though their signals are typically small. Therefore, while we focus on the transiting photometry in the rest of this thesis, the reflected-light method is indeed useful and complementary as well.

Schneider (1999) is the first to propose the transit photometry as a tool for the ring detection. Brown et al. (2001) derived the upper limit on the radius of a possible ring around HD 209458 b. Barnes & Fortney (2004) improved the model of Brown et al. (2001) by incorporating the influence of diffraction on the light curves. They claimed that the Saturn-like ring system can be detected with the photometric precision of the *Kepler* mission. Ohta et al. (2009) pointed out that the combination of the transit photometry and the spectroscopic Rossiter-McLaughin effect increases the detection efficiency and the credibility of the signal (see Section 5.2.2). Zuluaga et al. (2015) proposed that an anomalously large planet radius indicated from transit photometry can be used to select candidates for ringed planets (see Section 5.2.3). They also proposed that the anomalous stellar density estimated from the transit may be used as a probe of a ring.

In addition to the above methodology papers, a systematic search for ring systems using real data was conducted by Heising et al. (2015). They analyzed 21 short-period planets ($P \leq 50$ days) in the *Kepler* photometric data, and found no appreciable signatures of rings around the systems. This is an interesting attempt, but their null detection is not surprising because the ring tends to be unstable as the planet gets closer to the central star. In addition, Schlichting & Chang (2011) demonstrated that it is hard to detect the ring at below 0.1 AU in the case of solar-like stars. We discussed this topic in Section 6.

Instead, we attempt here a systematic search for rings around long-period planet candidates, selected in Section 6.6, that exhibit single or a few transit-like signals

in the *Kepler* photometric data. Since rings around those planets, if exist, should be dynamically stable, even a null detection would eventually put an interesting constraint on the formation efficiency and properties of icy rings for those planetary environments.

The purposes of the this chapter are three-fold; to establish a methodology of ring search procedure, to apply the methodology to a catalog of long-period planet candidates in Section 6.6, and to detect and/or constrain the possible ringed planets. Section 7.2 presents our simple model of a ringed planet, and describes the expected transit signal. In Section 7.3, we explain how to select target objects for our search, and classify them into four groups according to the amplitude and nature of the signal-to-noise ratio of their light curves relative to the expected signature by possible ringed planets. In Section 7.4, we place upper limits on ring parameters for seven systems with a good signal-to-noise ratio. In Section 7.5, we select five tentative ringed-planet candidates from the high signal candidates classified in Section 7.3. While four out of the five are likely to be false positives, one system, KIC 10403228, passes all the selection criteria that we impose. Therefore we attempt a systematic parameter survey for the possible ring around KIC 10403228 in Section 7.6. Also we examine and discuss various other possibilities that may explain the observed ring-like anomaly. Chapter 8 is devoted to conclusion and future prospects.

7.2 A simple model for a ringed planet

7.2.1 Basic parameters that characterize a ringed planet system

Our simple model of a ringed planet adopted in this thesis basically follows Ohta et al. (2009). The ring is circular, and has a constant optical depth τ everywhere between the inner and outer radii of $R_{\rm in}$ and $R_{\rm out}$. We denote the radii of the star and planet by $R_\star$ and $R_{\rm p}$.

The configuration of planet and ring during transit is illustrated in Figure 7.1. The X-axis is approximately aligned with the projected orbit of the planet on the stellar disk, and the Z-axis is towards the observer. This completes the (X, Y, Z) coordinate frame centered at the origin of the ringed planet (left panel in Figure 7.1). The normal vector of the ring plane is characterized by the two angles θ and ϕ in a spherical coordinate (right panel in Figure 7.1).

We also set up another coordinate system (x, y, z) centered at the origin of the star in such a way that the major and minor axes of the projected ring are defined to be parallel with x- and y-axes, respectively, with z-axis being towards the observer.

The ring is assumed to move along the planetary orbit with constant obliquity angles (θ, ϕ), and the planet is assumed to move on a Keplerian orbit around the star. The left panel in Figure 7.1 illustrates the transit of the ringed planet, whose impact parameter is b.

We assume a thin uniform ring with a constant optical depth τ for the light from the direction normal to the ring plane. Thus the fraction of the background stellar
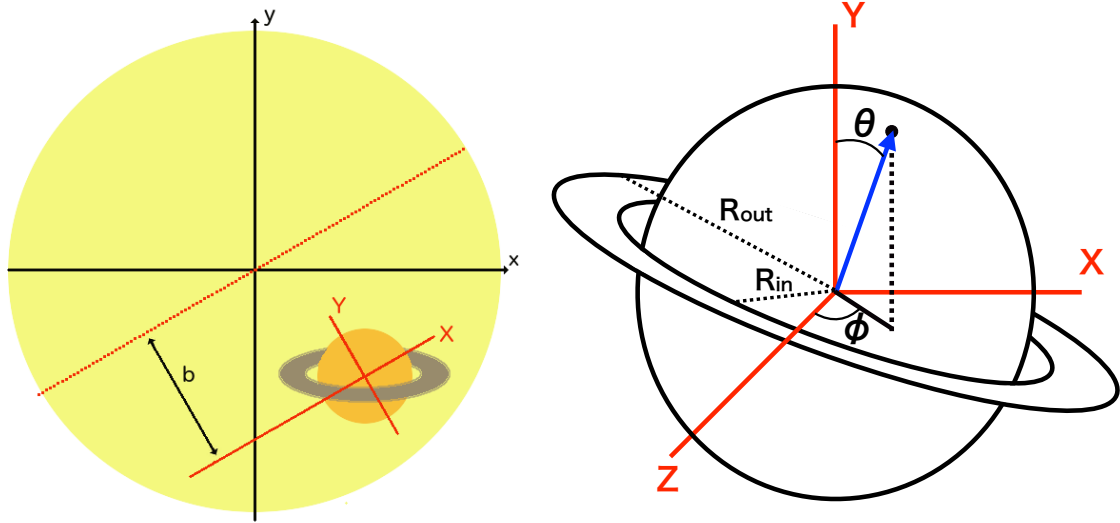
Figure 7.1: (Left) Schematic illustration of a transit of a planet with a ring. The origin of (X, Y) is shifted from the center of the planet to that of the star. The radius of the star is $R_\star$, the radius of the planet is R_p and the impact parameter of the planet is b. The z-axis and the Z-axis are toward the observer. (Right) Enlarged view of the planet with the ring. R_{in} and R_{out} are the inner and outer radii of the ring respectively. The obliquity angle θ and azimuthal angle ϕ are defined with respect to (X, Y, Z)-coordinate.

light transmitted through the inclined ring is given by $\exp(-\tau(\sin\theta\cos\phi)^{-1})$, and we define the shading parameter T as $1 - \exp(-\tau(\sin\theta\cos\phi)^{-1})$. In our simple ring model, the value of T, instead of τ, fully specifies the effective optical transparency of the ring.

In summary, our simple ring model is characterized by five parameters; four $(R_{in}, R_{out}, \theta, \phi)$ specify the geometry of the ring, the other is a shading parameter T. Instead of R_{in} and R_{out}, we use dimensionless parameters in fitting,:

$$r_{in/p} \equiv \frac{R_{in}}{R_p}, \qquad r_{out/in} \equiv \frac{R_{out}}{R_{in}}. \tag{7.1}$$

7.2.2   Transit signal of a ringed planet

The stellar intensity profile $I(x, y)$ under the assumption of the quadratic limb darkening law is expressed in terms of two parameters u_1 and u_2:

$$\frac{I(x, y)}{I_0} = \left[1 - u_1(1 - \mu) - u_2(1 - \mu)^2\right] \left(\mu \equiv \sqrt{1 - \frac{x^2 + y^2}{R_\star^2}}\right), \tag{7.2}$$

where I_0 is the intensity at the center of the star. The physical conditions on the profile require the following complex constraints on u_1 and u_2:

$$u_1 + u_2 < 1, \ u_1 > 0, \ u_1 + 2u_2 > 0. \tag{7.3}$$

In this thesis, we adopt $q_1 = (u_1 + u_2)^2$ and $q_2 = u_1/(2(u_1 + u_2))$ instead of (u_1, u_2) following Kipping (2013). Then, Equations (7.2) and (7.3) are rewritten as

$$\frac{I(x, y)}{I_0} = \left[1 - 2q_2\sqrt{q_1}(1 - \mu) - \sqrt{q_1}(1 - 2q_2)(1 - \mu)^2\right], \tag{7.4}$$

$$\text{with} \quad 0 < q_1 < 1,\ 0 < q_2 < 1. \tag{7.5}$$

In this parametrization, q_1 and q_2 vary independently between 0 and 1. This is useful in finding best-fit parameters (Kipping 2013). For reference, the Sun has $q_1 = 0.49$ and $q_2 = 0.34$ ($u_1 = 0.47$ and $u_2 = 0.23$) (Cox 2000).

Let $D(x, y, t)$ be the transmission fraction of light coming from the location on the stellar disk (x, y). Due to the motion of the planet during transit, $D(x, y, t)$ is time-dependent and given as

$$D(x, y, t) = \begin{cases} 1 & : \text{if } (x, y) \text{ is within the planetary disk} \\ T & : \text{if } (x, y) \text{ is within the ring disk, but out of the planetary disk} \\ 0 & : \text{otherwise.} \end{cases}$$
$$\tag{7.6}$$

Then the normalized flux from the the system is given by

$$F(t) = 1 - \frac{\int_{\text{stellar disk}} I(x, y)D(x, y, t)dxdy}{I_{\text{all}}}, \tag{7.7}$$

where the second term indicates the fraction of light blocked by a transiting ringed planet, and the total flux is

$$I_{\text{all}} = \int_{\text{stellar disk}} I(x, y)dxdy = \pi I_0 R_\star^2 \left[1 - \frac{2\sqrt{q_1}q_2}{3} - \frac{\sqrt{q_1}(1 - 2q_2)}{6}\right]. \tag{7.8}$$

We develop a reliable numerical integration method that solves the boundary lines of $D(x, y, t)$ as described in Appendix A. Our method achieves the numerical error less than 10^{-7} in relative flux, and this is much smaller than a typical noise of the *Kepler* photometric data.

7.2.3   Effects that are neglected in our model

We briefly comment on three effects that we neglect in the analysis below; finite binning during exposure time, planetary precession, and forward-scattering of the ring. While all of them are negligible for the Saturnian ringed planet with a long period, they may become important in other situations.

For the precise comparison of our light-curve predictions against the *Kepler* long cadence, we may have to take account of the finite exposure time (29.4 min) properly. In fact, the binning effect is shown to bias the transit parameter estimate in the case of short-period planets (Kipping 2010). For most of long-period planets that we focus on here, however, the transit duration is sufficiently longer than the finite exposure

time. Thus the binning effect is not important. In the case of the transit of Saturn in front of the Sun, for instance, the fractional difference of the relative flux is typically an order of 10^{-5} between models with and without the binning effect. This value is an order-of-magnitude smaller than the expected noise in the *Kepler* photometric data. Thus we can safely neglect the binning effect in the present analysis. In Appendix E, we discuss this material in detail.

The precession of a planetary spin would generate observable seasonal effects on the transit shape of a ringed planet (Carter & Winn 2010; Heising et al. 2015). Since our current target systems are extracted from those with a single transit, however, we can ignore the effect either; the period of the precession is proportional to the square of the orbital period, and thus the precession effect during a transit is entirely negligible. Nevertheless, we note here that this could be an interesting probe of the dynamics of short-period ringed planetary systems that exhibit multiple transits.

In the present analysis, we consider the effect of light-blocking alone due to the ring during its transit. In reality, forward scattering (diffraction by the ring particles) may increase the flux of the background light. Let us consider light from the star to the observer through the ring particle with diameter d. First, light is emitted from the disk of the star, and arrives at the ring particles. The angular radius of the star viewed from the ring particles is about $R_\star/a_\mathrm{p}$, where a_p is the semi-major axis of the relative orbit, and $R_\star$ is the stellar radius. Next, the light is diffracted by the ring particles, and the extent of the diffraction is described by the phase function (Barnes & Fortney 2004); the rough diffraction angle can be estimated from the first zero of the phase function $\theta \simeq 0.61\lambda/d$, where λ is wavelength of light. In particular, the effect of the diffraction becomes significant when the viewing angle $R_\star/a_\mathrm{p}$ is comparable to the diffraction angle. Let us define the critical particle size d_crit by equating $R_\star/a_\mathrm{p}$ with $\theta = 0.61\lambda/d$;

$$d_\mathrm{crit} = 0.61\,\frac{a_\mathrm{p}\lambda}{R_\star} = 0.63\,\mathrm{mm}\left(\frac{a_\mathrm{p}/R_\star}{2060}\right)\left(\frac{\lambda}{500\mathrm{nm}}\right). \tag{7.9}$$

Barnes & Fortney (2004) discussed the effect of diffraction using d_crit. When $d \geq 10d_\mathrm{crit}$, the diffraction angle is small, and light just behind the ring particles is diffracted to the observer. In this case, the diffraction does not affect the direction of light, and we may express the extinction due to absorption with a single parameter T.

When $d \leq d_\mathrm{crit}/10$, the diffraction angle is large, and the ring particles diffract light to wider directions. Then, the amount of light, which reaches the observer, significantly decreases, and we may model the extinction in terms of T.

In both cases, $d \geq 10d_\mathrm{crit}$ and $d \leq d_\mathrm{crit}/10$, the extinction can be modeled with a single parameter T. In the case of Saturn with the typical particle diameter $d = 1$ cm, for instance, $d_\mathrm{crit} \simeq 0.63$ mm from Equation (7.9) satisfies $d > 10d_\mathrm{crit}$, so our model can be used to calculate the light curves of Saturn observed far from the Solar System.

We should note that when the typical size of particles satisfies $d_\mathrm{crit}/10 \leq d \leq 10d_\mathrm{crit}$, the forward scattering induces the rise in the light curve before the ingress and after the egress, and this effect can become the key to identify the signatures of the rings out of other physical signals. Incorporating the diffraction into the model, however,

requires intensive computation, and this is beyond the scope.

7.3 Classification

7.3.1 Overview of classification

In what follows, we present our methodology to search for planetary rings in the real data. Figure 7.2 shows the flow chart of the analysis procedure and its application. Methods in each step of the chart are described along with the results of analysis in the following sections. For our current search, we consider the transiting long-period
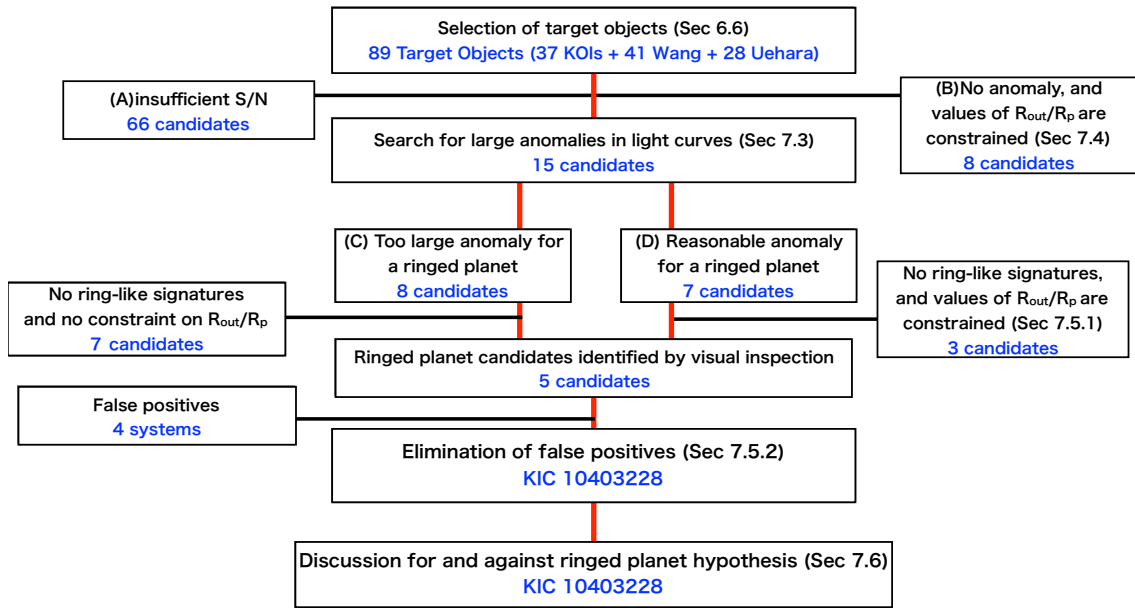
Figure 7.2: Flow chart of our strategy of ringed-planet search. Procedure and the number of remaining candidates are described in each step. The details of each procedure are described in the corresponding sections. For classification into (A)$\sim$(D), model I is adopted in Table 7.1.

planets selected in Section 6.6. We classify them into four categories depending on the observed anomalies in the light curves. The details of classification procedure are found in Appendices B and C.

7.3.2 Classification of target objects

Inevitably a signature of a possible ring around a planet is very tiny. Long-period planet candidates exhibit a small number of transits (Table 6.1), and the precision of the transit light curves is not improved so much by folding the multiple events. Therefore the search for a possible ring signature crucially relies on the quality of the few transiting light curves for individual systems.

According to the automated procedures described in Appendices B and C, we classify the long-period planet candidates into the following four categories.

(A) insufficient S/N to constrain ring parameters:

Since the anomalous feature due to the ring is very subtle, one cannot constrain the ring parameters at all if the intrinsic light-curve variation of the host is too large to be explained by any ring model. Thus we exclude those systems that exhibit a noisy light curve out-of-transit. The exclusion criteria depend on the adopted ring model to some extent, but are determined largely by the threshold signal-to-noise ratio (S/N) that we set as $S/N = 10$. For definiteness, we consider 4 different ring models (Table 7.1), and the details of the procedure are described in Appendices B and C.

(B) sufficient S/N and no significant anomaly:

A fraction of the systems has a sufficiently good S/N and exhibits no significant anomaly. In such a case, we can put physically meaningful constraints on the possible ring parameters (Section 7.4).

(C) too large anomaly for a ringed planet:

In contrast to (B), some systems exhibit a large anomaly in the transiting light curve that exceeds the prediction in the adopted ring models. Nevertheless, different ring models may be able to explain the anomaly, and we still continue to search for ringed planets in this category (Section 7.5).

(D) reasonable anomaly for a ringed planet

Finally a small number of systems with a good S/N indeed exhibit a possible signature that could be explained in the ring model. We perform additional analysis to test the validity of the ring hypothesis in a more quantitative fashion (Section 7.5 and 7.6).

The above classification is done on the basis of observed anomalies, which are derived by fitting a planet model to light curves. The data are taken form the Mikulski Archive for Space Telescopes (MAST), and we use the Simple Aperture Photometry (SAP) data taken in the long-cadence mode (29.4 min). In fitting, we use only the first transit in the light curve for each candidate in deriving the observed anomaly for simplicity. After fitting the planet model to data, the long-period planet candidates are automatically classified into the above categories (A)∼(D). Table 7.1 summarizes the results of classification for four models. In a later section, we use the classification according to model I, which contains more candidates in categories (B)∼(D) than the other three.

As candidates in (A) have insufficient S/N for further analysis, we do not consider them in the following analysis. In Section 7.4, we obtain upper limits on $R_{\mathrm{out}}/R_{\mathrm{p}}$ for candidates in (B). In Section chap:sec6, we first search for the ringed planets in categories (C) and (D) by visual inspection, and later examine the reliability of transits more quantitatively. In Section 7.6, we interpret the possible ringed planet candidate.

7.4   Upper limits of $R_{\mathrm{out}}/R_{\mathrm{p}}$ for candidates in (B)

Upper limits on $R_{\mathrm{out}}/R_{\mathrm{p}}$ are given for candidates in (B) as a result of classification. Figure 7.3 shows the light curves and fitted curves of eight candidates classified to (B)

Table 7.1: Parameters and classification.

Parameters	Meaning				
P(day)	Period	10759			
$a/R_\star$	Scaled semi-major axis	2059.67			
q_1	Limb darkening parameter	0.49			
q_2	Limb darkening parameter	0.34			
t_0(day)	Time of a transit center of a planet	0			
T	Shading coefficient	1.0			
$r_{\mathrm{in/p}}$	Ratio of R_{in} to R_{p}	1.0			
$r_{\mathrm{out/in}}$	Ratio of R_{out} to R_{in}	.			
$R_{\mathrm{p}}/R_\star$	Planet to star radius ratio	.			
		model I (Fiducial)	model II	model III	model IV
b	Impact parameter	0.8	0.5	0.8	0.5
θ(deg)	Angle between Y-axis and axis of the ring	45	45	arcsin(0.1)	arcsin(0.1)
ϕ(deg)	Angle between Z-axis and ring-axis projected onto (Z,X)-plane	45	45	0	0
r_{eq}	Boundary value, above which the sky-projected ring is larger than the planetary disk (see Appendix B.3 for detailed explanation)	2.0	2.0	10.0	10.0
	Classification	Number of classified systems			
	(A) insufficient S/N	66	82	80	82
	(B) sufficient S/N to $R_{\mathrm{out}}/R_{\mathrm{p}}$	8	1	2	1
	(C) too strong anomaly	8	3	4	4
	(D) possible candidate	7	3	3	2

in model I. They show no appreciable anomalies in the residual relative to the single planet model. For these candidates, we could detect the ring signature if exists. Thus in turn, we can derive the upper limits on $R_{\mathrm{out}}/R_{\mathrm{p}}$. This is done by simply comparing the expected anomaly in model I and the observed anomaly in the light curve. The details of the method to place upper limits on $R_{\mathrm{out}}/R_{\mathrm{p}}$ are described in Appendix B and C, and the results are summarized in Table 7.2.

7.5 Search for ringed planets

In this section, we search for ringed planets in categories (C) and (D), extract the tentative ringed planet candidates, and examine whether the transits are not false positive.

7.5.1 Tentative selection of possible ringed planets

Figures 7.4 and 7.5 show the light curves of candidates in categories (C) and (D), respectively. Candidates in (C), where the observed anomaly exceeds the prediction of model I, may be consistent with other ringed planets in different configurations. Thus, we search for ringed planets not only in (D) but also (C).

We extract ringed planet candidates by visual inspection of their light curves on the basis of following properties expected for ringed planets:

- Transit duration at ingress and/or egress is long.
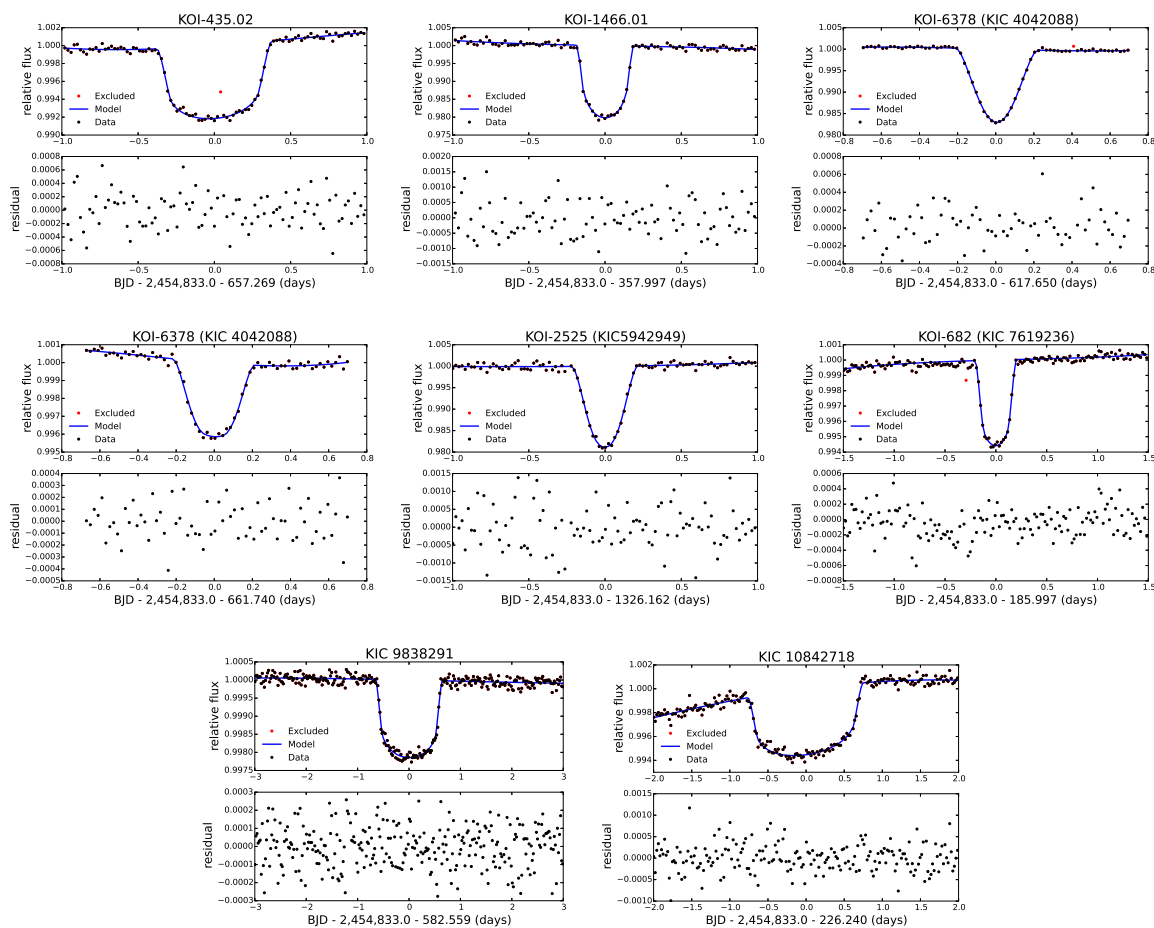
Figure 7.3: Candidates in (B) with sufficient S/N to constrain $R_{\mathrm{out}}/R_{\mathrm{p}}$. The light curves (black circles) are shown with the best-fit planet models (blue lines). The red points are excluded in fitting. The horizontal axis shows time in BKJD = BJD - 2454833.0 (the Barycentric Kepler Julian Date) offset by the central time of the transit.

Table 7.2: Upper limits of radii of outer rings.

Name	Upper limits of $R_{\mathrm{out}}/R_{\mathrm{p}}$ in model I	$R_{\mathrm{p}}(R_J)$	$a_p(\mathrm{AU})$	Transit Epoch (BKJD)
Candidates in (B)				
KOI-435.02	1.5	0.66	1.28	657.269
KOI-1466.01	1.5	1.13	1.14	357.997
KIC 4042088	1.2	2.94	0.78	617.65
KIC 4042088	1.95	0.85	1.41	661.74
KIC 5942949	1.5	1.18	1.13	1326.162
KIC 7619236	1.7	0.71	1.35	185.997
KIC 9838291	1.9	0.42	14.3	582.559
KIC 10842718	1.6	0.75	7.60	226.300
Candidates in (D)				
KOI-490.02	1.2	1.16	2.53	492.772
KOI-868.01	1.2	0.76	0.74	208.401
KIC 8012732	1.8	0.67	0.68	391.807
KIC 8410697	1.8	0.77	3.19	542.122

- Transit shape is asymmetric due to the non-zero ϕ.

As a result, we identify five systems KOI-771(D), KOI-1032(C), KOI-1192(D), KOI-3145(D), and KIC 10403228(D) as tentative ringed planets. For the other four candidates in (D), which show no visible ring-like feature in the light curves, we obtain the upper limits on $R_{\mathrm{out}}/R_{\mathrm{p}}$ in the same method as in the previous section (Table 7.2). In total, we obtain the upper limits on $R_{\mathrm{out}}/R_{\mathrm{p}}$ for 12 candidates, and the six of them have $R_{\mathrm{out}}/R_{\mathrm{p}} \leq 1.5$.

For six candidates in (C) with no ring-like features, we cannot set the upper limits of ring parameters, and we conclude that the signals are not due to rings, but are due to the temporal stellar activities.

7.5.2 Elimination of false positives

We examine the reliability of transit signals for the five preliminary candidates. As a result, we find that four are false positives, and KIC 10403228 still passes all criteria. More specifically, we regard a target as a false positive if one of the following criteria is satisfied (Coughlin et al. 2016).

Criterion 1: The target object exhibits a significant secondary eclipse, which is expected for an eclipsing binary.

- *Results*: None of our candidates exhibits the secondary eclipse.

Criterion 2: The signal originates from the other nearby stars or instrumental noise.

- *Results*: Inspecting Target Pixel Files, we found that the dips in the light curves of KOI-1032.01, KOI-1192.01, and KOI-3145 do not come from the target stars. Figure 7.6 shows an example of KOI-1192.01. Community Follow-up Observing Program (CFOP) classifies KOI-1032.01 as a false positive
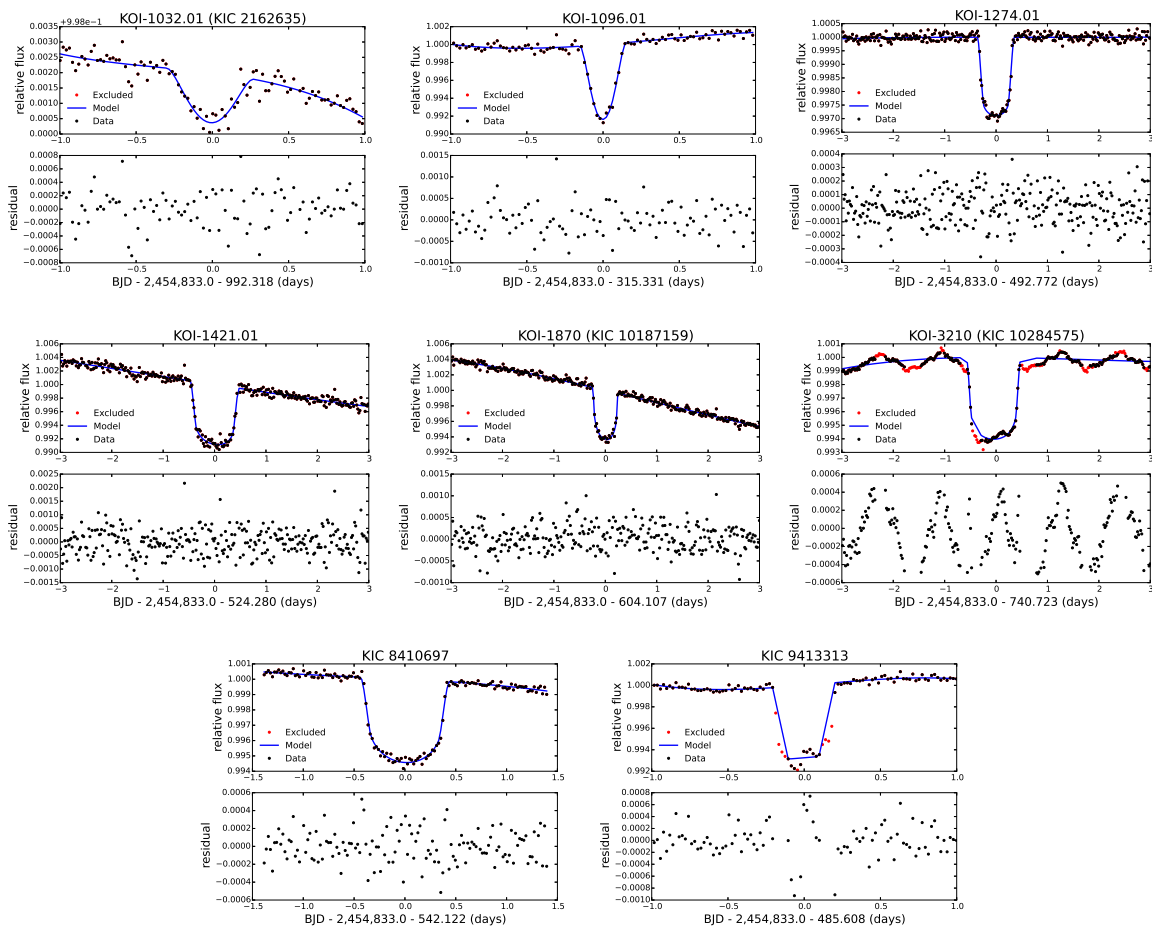
Figure 7.4: Candidates in (C) with too large anomaly for a ringed planet. The format of the figure is the same as Figure 7.3.
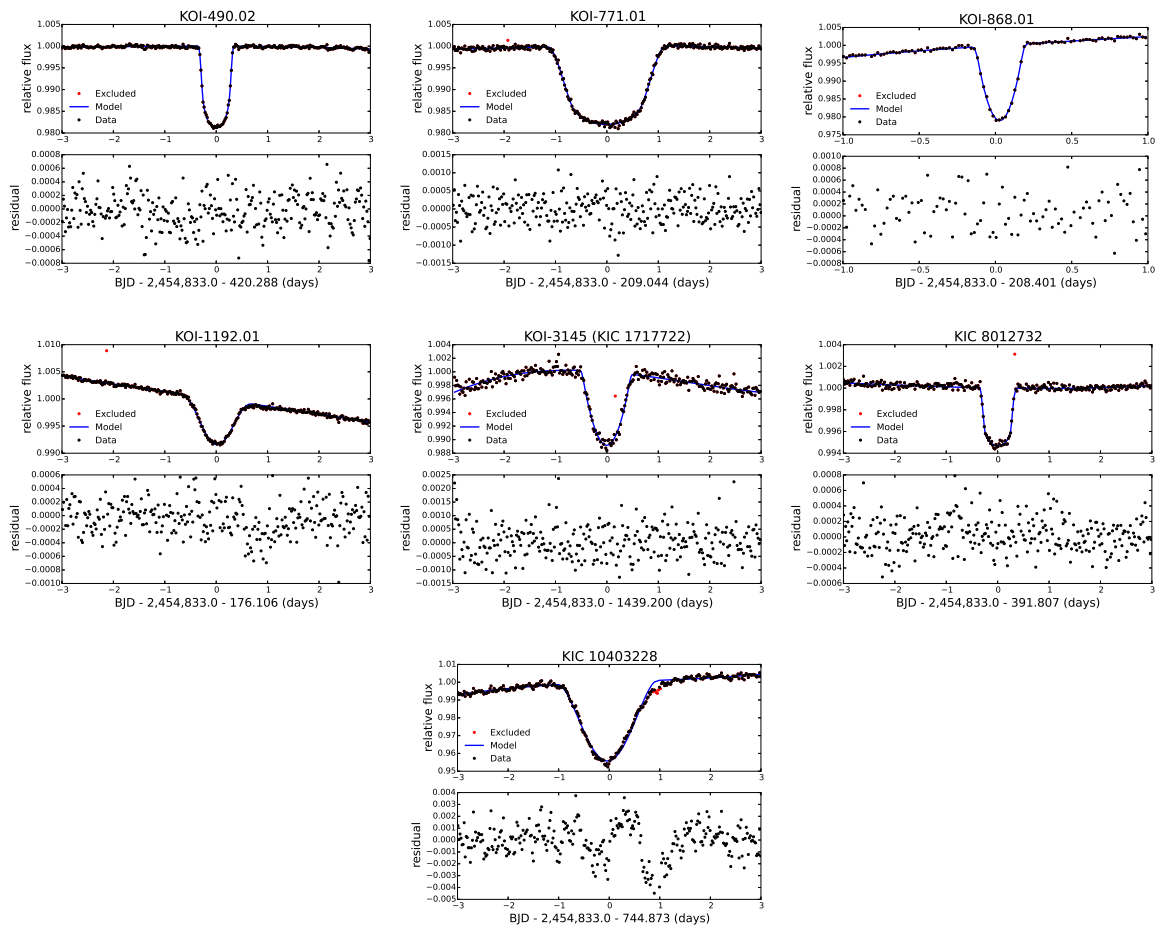
Figure 7.5: Candidates in (D) with moderate anomaly for a ringed planet. The format of the figure is the same as Figure 7.3.

(Uehara et al. 2016). Wang et al. (2015) and Uehara et al. (2016) also indicate that KOI-1192.01 and KOI-3145 are false positivities. Moreover, we find that the transit depths in the light curves of KOI 771.01 differ in many pixels, and the contaminations from the non-target stars are very strong. Wang et al. (2015) also pointed out that this system is false positive. For KIC 10403228, the transit depths differ in only two pixels, while it is constant in the other pixels, so we conclude that the signal is originated from the target star. The more detailed discussion of KIC 10403228 is presented in a later section.

Criterion 3: The transit simultaneously occurs at different stars in different pixels. This indicates that the signal does not originate from the target but from the instrumental noise.

  - *Results*: The transit events of KOI-1032.01 and KOI-1192.01 are located at the same time. This result is consistent with that of the Criterion 2.

Criterion 4: The shape of the light curve is inconsistent with that of a transiting object.

  - *Results*: From Figures 7.4 and 7.5, all signals fit well to transit-like features.

KIC 10403228 is the single system that passes all the criteria. Thus, we move on to the detailed pixel-based analysis next.
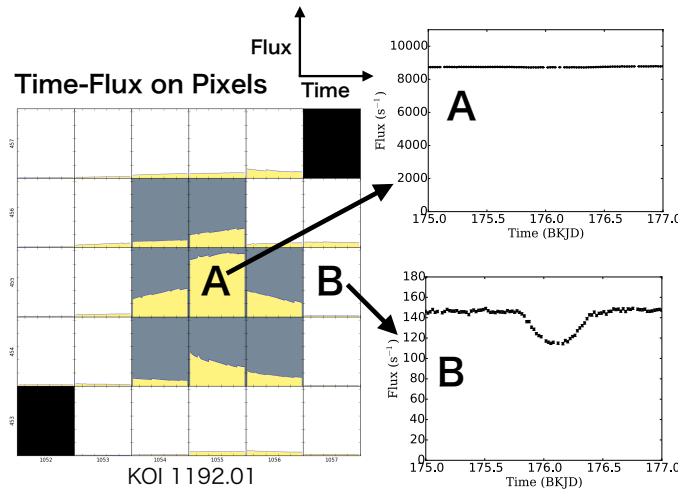
Figure 7.6: Indication that KOI-1192.01 is a false positive. The light curves of the pixels labeled as A and B are shown in the right panels. The pixel located at A receives the largest amount of light among pixels of the target star, and the pixel located at B receives the small amount of light. The very different relative depths in the two pixels indicate that the signal does not originate from the target star at the center.

7.5.3   Detailed pixel analysis on KIC 10403228

KIC 10403228 is considered to be an M dwarf and has a nearby star separated by about 3 arcsec (Rappaport et al. 2014). According to the data taken by United Kingdom Infrared Telescope (UKIRT), the nearby star is located at (RA, Dec) = $(19^h\, 24^m\, 54.25^s,\ +47° 32'\, 57.5'')$ and its J-band flux is about 1/5 of KIC 10403228. Here we examine the possibility that the transit is associated with this nearby star rather than KIC 10403228.

   Figure 7.7 shows the light curve and fractional depth of the transit event in each of the pixels around KIC 10403228. The small transit depths in pixels A and B suggest that the source of the transit is not the nearby star shown by a red filled star, because otherwise the transit depths should be larger in those pixels close to the nearby star. To evaluate this fact in a more quantitative way, we also calculate the centroid offset using the pixel-level light curves. As a result, we find that the flux centroid moves towards the nearby star during the transit and that the displacement is comparable to the value expected from the observed transit depth (5%) and the flux ratio in J-band (5 : 1). The variation of the transit depth and the centroid displacement consistently indicate that the transit is not due to the nearby star. While we may be able to evaluate the contamination on the light curve from this nearby star more quantitatively, it does not change our conclusion in any case, and we do not perform the detailed analysis for simplicity.

   We note that the transit signal is clearly modulated with a short-periodic component (panel B in Figure 7.7). Since the modulation is not visible at panel C, it is most likely due to the nearby star. Actually, there is another long-period modulation with $P \simeq 35$ days in the light curve, which may come from the target star. If these periods are related to the stellar spins, the nearby star is a fast rotating star, and the target star is a slow rotator. Thus, we may ignore the effect of gravity darkening of the target star.

7.6   Detailed analysis of a possible ringed planet KIC 10403228

Although the candidate KIC 10403228 is identified from model I, we survey a wider parameter space for the possible ring beyond model I. Then, we discuss the reliability of the ring hypothesis.

7.6.1   Fit of a ringed planet model to the observed light curve

We fit various models with and without the ring to the light curve of KIC 10403228 by minimizing the value of χ^2 defined in Equation (B.4). In practice, we use ± 3.09 days-time window to trim 300 data points centered around $T_0 = 744.773$ day (BKJD [= BJD-2454833 day]). To remove the long-term flux variations in the light curve,
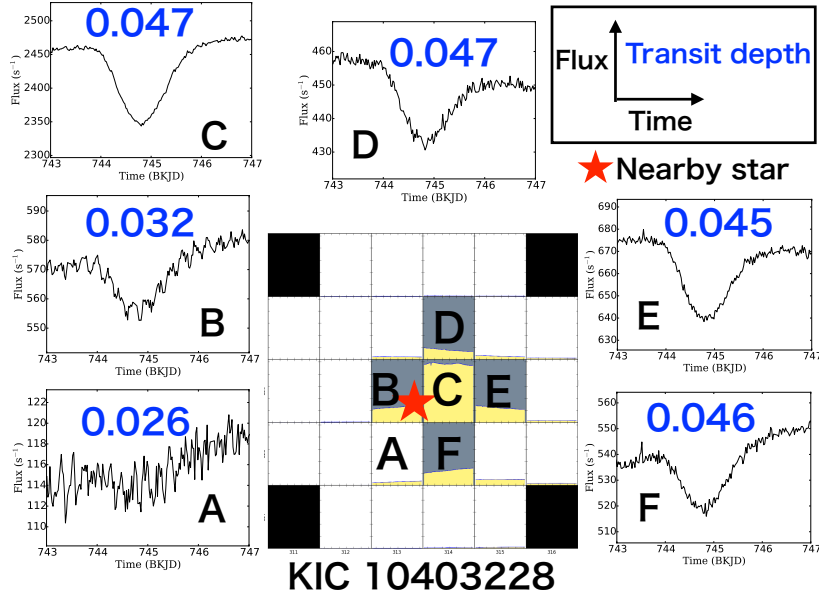
Figure 7.7: Light curves on pixels are shown along with the approximate depth of the transit. A red star expresses the position of the nearby star. The depth is shallow in the left side of the region, where the contamination from the nearby star is large.

we adopt the model in Equation (B.5) that is composed of a fourth-order polynomial and the transit model $F(t)$ in Equation (7.7). The standard deviation σ is estimated to be 9.17×10^{-4} from the out-of-transit data. This value is about 1.3 times larger than the error recorded in the SAP data.

As the transit of KIC 10403228 is observed just once, we cannot infer the orbital period from the timing of the transit. However, we can infer it from Kepler's law. To achieve the grazing and large transit of KIC 10403228, the geometrical width of the planetary path during the transit should be comparable to the $2R_\star$. So the transit duration T_{tra} is approximately given by

$$T_{\mathrm{tra}} \simeq P \left(\frac{2R_\star}{2\pi a} \right) \frac{\sqrt{1-e^2}}{1+e\sin\omega}, \tag{7.10}$$

where the last factor is a correction term due to an eccentricity e with ω being the argument of periapse. From Kepler's law and Eq (7.10), one obtains

$$P \simeq 450 \text{ years} \left(\frac{\rho_\star}{12.6 \text{ g cm}^{-3}} \right) \left(\frac{T_{\mathrm{tra}}}{2 \text{ days}} \right)^3 \left(\frac{1+e\sin\omega}{\sqrt{1-e^2}} \right)^3. \tag{7.11}$$

We obtain $P \simeq 450$ years if we adopt $e = 0$, $T_{\mathrm{tra}} = 2$ days for the transit duration of KIC 10403228, and the stellar density $\rho_\star = 12.6 \pm 6.0$ g cm^{-3} from Wang et al. (2015). The stellar density in Wang et al. (2015) is adopted from Dressing & Charbonneau (2013), who estimated the stellar properties by comparing the observed colors taken in 2MASS and SDSS with the Dartmouth model (Dotter et al. 2008).

Before fitting, we examine how often we expect to see a transit of a planet with $P \simeq 450$ years. Assuming that all the stars host planets with $P \simeq 450$ years, the expected number of transit detections, which corresponds to the upper limit of the number from the assumption, is given by

$$n_{\rm tra} = 0.045 \left(\frac{N_{\rm target}}{150,000} \right) \left(\frac{t_{\rm obs,dur}/P}{4 \text{ years}/450 \text{ years}} \right) \left(\frac{R_\star/a}{1/250,00} \right), \qquad (7.12)$$

where $a/R_\star = 25000$ is the fiducial value estimated from equation (7.10), $t_{\rm obs,dur}$ is a observational period, and $N_{\rm target}$ is the number of target stars. The adopted values of $t_{\rm obs,dur}$ and $N_{\rm target}$ are the typical values of *Kepler*. The estimated $n_{\rm tra}$ is not big, but not so unlikely. Apart from the tiny ring-like feature, the overall shape of the signal is clearly due to the transiting or eclipsing event, and it is very difficult to explain the feature from the stellar activities.

We would like to comment on the reliability of $P \simeq 450$ years. The key parameters are $\rho_\star$ and the eccentricity in Eq (7.11). For example, if the system is a giant star rather than a M dwarf, the density and the period would be small. In this sense, to specify the correct stellar density, we would need a follow-up observation. Moreover, the eccentricity can also change the estimated period in Eq (7.11). If $e = 0.6$, the period can be changed by the factor of $(1/8.0) \sim 8.0$, and if $e = 0.9$, the factor of change is within $(1/82.82) \sim 82.82$ (or 5 years $<$ P $<$ 34,000 years). Thus, the planet with a relatively short period and a large eccentricity can also explain the data. Although the period is uncertain, the different period does not change the fitting results, so we adopt $P = 450$ years for the fiducial value for the time being.

For fitting, we adopt $P = 450$ years, and q_1 and q_2 from the official catalog of *Kepler*. In summary, there are nine free parameters, $t_0, R_{\rm p}/R_\star, b, a/R_\star$, and $c_i (i = 0 \sim 4)$ for the model without the ring, and five additional parameters $\theta, \phi, r_{\rm in/p}, r_{\rm out/in}$ and T for the model with ring. We set the initial values of $c_i (i = 0 \sim 4)$ to those obtained from a polynomial curve fitting for the out-of-transit data.

First, we fit the planet alone model to the data. The blue line in Figure 7.8 is the best-fit model without the ring. The best-fit parameters are listed in Table 7.3. The residuals from the fit clearly have some systematic features, and the planet alone model fails to fully explain the light curve, in particular, around 745.8 day (BKJD) in Figure 7.8. Therefore, we attempt to interpret the data with the ringed planet model. After trying a lot of initial values for fitting, we finally find two solutions, which give at least local minimums of χ^2 in Equation (B.4). Figure 7.8 shows the fitting results of both fitting in the red and green lines. The best-fit parameters are shown in Table 7.3. The geometrical configurations for both solutions are shown in Figure 7.9. Clearly, models with the ring significantly improve the fit without ring.

In Table 7.3, values of R_p, $R_{\rm in}$, and $R_{\rm out}$ are calculated on the assumption of $R_\star = 0.33 \pm 0.05\,R_\odot$ (Wang et al. 2015). It turns out that the resulting ratio of ring and planet radii is similar to that of Saturn: $R_{\rm in} \simeq 1.5 R_{\rm p}$ and $R_{\rm out} \simeq 2.0 R_{\rm p}$.
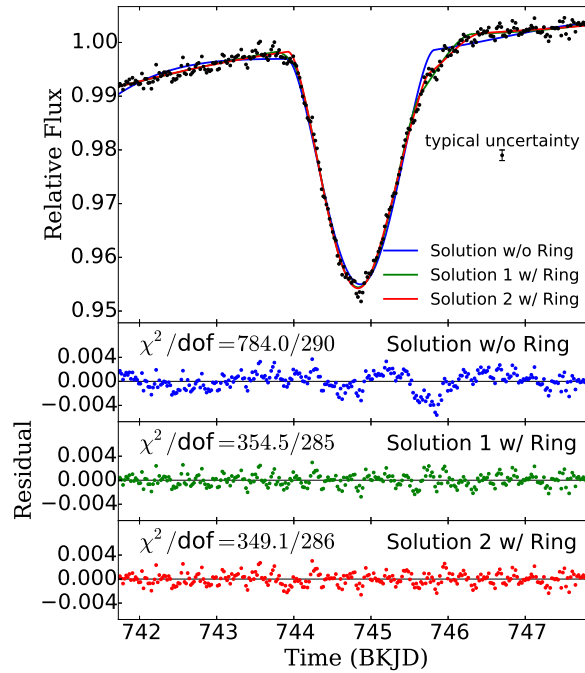
Figure 7.8: Comparison of the light curve of KIC 10403228 (black data) with the models with ring (red line & green line) and without ring (blue line). We found different configurations for the model with ring. While the model without ring cannot explain the data around 745.8 day (BKJD), the ringed planet model fits the data well. Residuals and χ^2 of fit are shown in each panel.
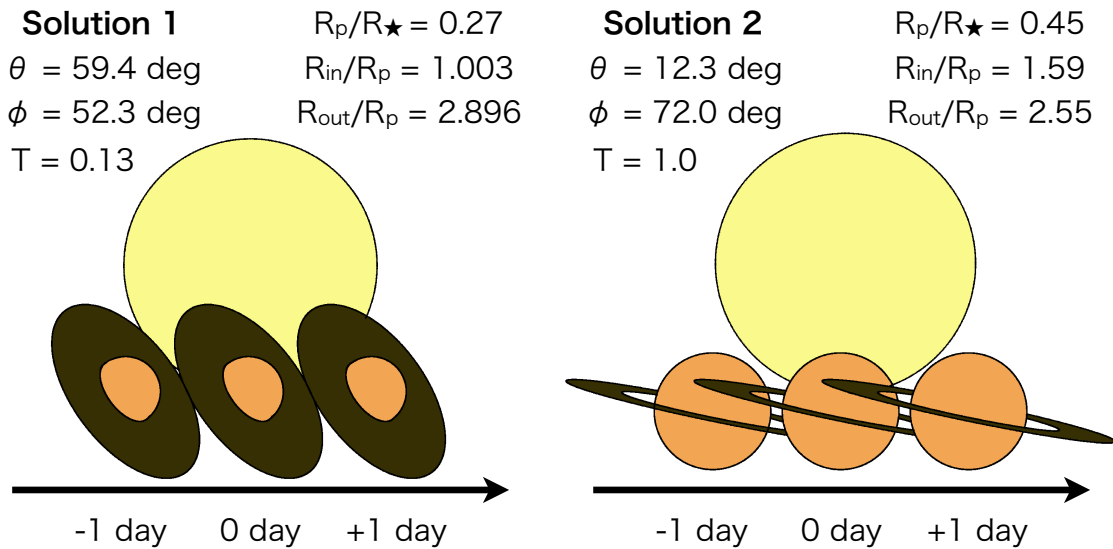
Figure 7.9: Schematic illustration of the ringed planet models for the two best-fit solutions. Positions of the planet are shown at $-1, 0, +1$ day from the central time of the transit of the planet. Note that the occultation of the star due to the ring continues even after the transit of the planet is completed.

Table 7.3: Best fit parameters for the transit of KIC 10403228

	Single planet	Ringed planet (solution 1)	Ringed planet (solution 2)
Fixed parameters			
P (years)	450	450	450
q_1	0.6737	0.6737	0.6737
q_2	0.0767	0.0767	0.0767
Variables			
t_0 (day)	0.065 ± 0.0021	0.017 ± 0.016	0.0386 ± 0.0052
$R_p/R_\star$	0.46 ± 9.09	0.27 ± 0.33	0.45 ± 0.05
$b(= a\cos i/R_\star)$	1.16 ± 10.6	0.99 ± 0.44	1.14 ± 0.06
$a/R_\star$	24275.0 ± 31617.1	25394.5 ± 765.0	25743.9 ± 215.6
T	·	0.13 ± 0.07	1.0 (converged to upper bound)
θ (deg)	·	59.4 ± 45.0	12.3 ± 4.0
ϕ (deg)	·	52.3 ± 24.9	72.0 ± 4.5
R_{in}/R_p	·	1.003 ± 2.95	1.59 ± 0.42
R_{out}/R_{in}	·	2.89 ± 8.0	1.61 ± 0.59
c_0	0.9972 ± 0.0002	1.00023 ± 0.00034	0.9999 ± 0.0003
c_1	0.00066 ± 0.00008	0.0014 ± 0.0001	0.0015 ± 0.0001
c_2	0.00067 ± 0.00011	-0.00047 ± 0.00015	-0.00030 ± 0.00013
c_3	0.000158 ± 0.000013	0.000053 ± 0.000015	0.000038 ± 0.000015
c_4	-0.000072 ± 0.000011	0.000021 ± 0.000014	0.000005 ± 0.000012
(Given $R_\star = 0.33 \pm 0.05\ R_\odot$)			
$R_{\rm p}$ $(R_J$ [a]$)$	1.48 [b]	0.88 ± 1.07	1.44 ± 0.27
$R_{\rm in}$ $(R_J$ [a]$)$	·	0.89 ± 2.65	2.29 ± 0.72
$R_{\rm out}$ $(R_J$ [a]$)$	·	2.56 ± 1.36	3.69 ± 0.23
(Statistical values)			
$\chi^2_{\rm red}$ $(=\chi^2/{\rm dof})$	2.70 $(=784.0/290)$	1.24 $(=354.5/285)$	1.23 $(=349.1/286$ [c]$)$

[a] R_J is the radius of Jupiter.
[b] $R_{\rm p}/R_\star = 0.46$ and $R_\star = 0.33 R_\odot$ are assumed.
[c] T is converged to the upper bound, so dof $= 286 = 285 + 1$.

7.6.2   Implication of the fitted model for KIC 10403228

The radiative equilibrium temperature of the ring particle is given by

$$T_{\mathrm{eq}} \simeq 15.1\,\mathrm{K} \left(\frac{25000}{a/R_\star}\right)^{0.5} \left(\frac{T_\star}{3386\,\mathrm{K}}\right) \left(\frac{1-A}{1-0.5}\right)^{0.25}, \qquad (7.13)$$

where we fiducially adopt the Bond albedo of the ring particle A of 0.5. The stellar effective temperature $T_\star = 3386$ K of KIC 10403228 is taken from Wang et al. (2015). Since the equilibrium temperature expected from the model is much lower than the temperature 170 K at the snow line (Hayashi 1981), icy particles around the planet can survive against the radiation of the host star.

The best-fit values of $\theta = 59.4°$ for solution 1 implies a significantly tilted ring with respect to the orbital plane, and $\theta = 12.3°$ for solution 2 implies a slightly tilted ring. We examine the stability of those tilted rings on the basis of a simple tidal theory. Under the assumption that the ring axis is aligned with the planetary spin, the damping timescale of the ring axis is equal to that for the orbital and equatorial planes of the planet to be coplanar. This time-scale is given by a tidal theory (e.g. Santos et al. 2015):

$$\tau_{\mathrm{tidal}} = \frac{P_{\mathrm{orb}}Q}{9\pi k_2}\frac{\rho_p}{\rho_s}\left(\frac{a_p}{R_\star}\right)^3 \simeq \frac{GP_{\mathrm{orb}}^3 Q}{27\pi^2 k_2}\rho_p$$

$$= 6.94 \times 10^{16}\,\mathrm{yr}\left(\frac{P_{\mathrm{orb}}}{450\,\mathrm{years}}\right)^3 \left(\frac{2.3\times10^{-4}}{k_2/Q}\right) \left(\frac{\rho_p}{0.70\ \mathrm{g\,cm}^{-3}}\right), \quad (7.14)$$

where P_{orb} is an orbital period, Q is a dissipation factor, and k_2 is the second Love number. If we adopt $k_2/Q = 2.3 \times 10^{-4}$ (Lainey et al. 2012) and $\rho_p = 0.70$ gcm^{-3} (Cox 2000) of Saturn, the damping timescale is sufficiently long. Thus, the best-fit configurations are consistent with the spin damping theory even under the assumption that the equatorial plane of the planet is coplanar with the ring plane. Thus, the tilted rings of our best-fits also imply the non-vanishing obliquity of the planet.

7.6.3   Possibilities other than a ringed object

We have to admit that it is very difficult to prove the existence of ring merely from our current model fit. Nevertheless it is difficult to explain the feature from other models. In this section, we examine various possibilities that may potentially account for the light curve of KIC 10403228 without the presence of a ring assuming that the main signal comes from the planetary transit as we stated in Section 7.6.1.

Oblate planet

A significant oblateness of a single planet may mimic a ring-like anomaly during a transit. Indeed our model reduces to an oblate planet if we set $R_{\mathrm{p}} = 0$, $R_{\mathrm{in}} = 0$, and $T = 1.0$ with an appropriate choice of θ and ϕ. We attempt the fit of this oblate planet

model to the light curve, and obtain the best-fit with $\chi^2/\mathrm{dof} = 492.4/288$. This value is much larger than the best-fit value $\chi^2/\mathrm{dof} = 349.1/286$ with the model with ring. Furthermore, the best-fit oblate planet model requires the projected ellipticity of the planet to be $f = (a - b)/a = 0.79$, where a is the major axis, and b is the minor axis. This solution is an unstable configuration; the rotating object will break up due to the centrifugal force when $a \geq 1.5b$ (Equation (2.14) in Maeder (2009)). Thus, we conclude that the oblateness of the planet is unlikely to explain the observed anomaly.

Exomoon

A transit of an exomoon or a binary planet is yet another possibility for the peculiar light curve of KIC 10043228. However, this possibility is ruled out by the shape of the anomaly.

As shown in Figure 7.8, the anomaly in the light curve is significant only in the latter half. Motivated by this fact, we fit the light curve using the planet-alone model, masking the latter half of the transit and adopting the same baseline as obtained in Table 7.3 (solution 2); the difference between this model and the observed light curve would represent the anomalous contributions from anything other than the main transiting planet. The result in Figure 7.10 clearly shows that the anomaly consists of a short rise in the flux followed by a more significant dip. Such a feature is clearly inconsistent with the transit of an exomoon.
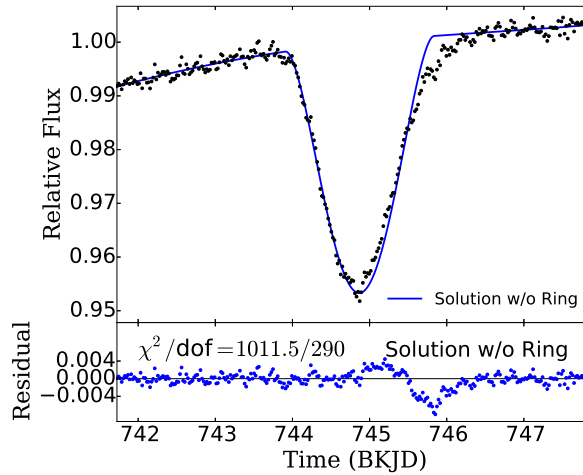
Figure 7.10: Planet-alone fit to only the first half of the transit light curve. The baseline polynomial is the same as that in solution 1 in Table 7.3. The anomaly consists of a rise followed by a dip.

Anomalies specific to in-transit data

There exist anomalies specific to in-transit data; spot crossing and gravity darkening. If the planet crosses spots on the stellar surface, the light curve is deformed (e.g. Sanchis-Ojeda et al. 2011). In general, however, spots are dark, so spot-crossing causes

a bump in the light curve. The observed anomaly in the bottom panel of Figure 7.10 is inconsistent with a single bump, so the spot is unlikely to cause the anomaly. Gravity darkening makes the light curve asymmetric (e.g. Barnes et al. 2011; Masuda 2015). In Section 7.5.3, we identify the target star as the slow-rotating star, and the gravity darkening is negligible. In conclusion, these mechanisms are unlikely to explain the ring-like signal in the light curve.

Stellar noise

The ring-like structure in the light curve shows up only for a short duration. Thus, the short-term stellar noise might mimic the ring-like anomaly just by chance. To discuss this possibility, we investigate the statistical property of the stellar activity of KIC 10403228. Specifically, we consider how frequently one encounters stellar noises comparable to the anomalous in-transit residuals in out-of-transit data. As will be shown, we find it difficult to reproduce the feature with stellar activities of KIC 10403228. In principle we could check to see if the similar feature arises in stars other than KIC 10403228 more generally, but it is a separate question and does not answer if the signal for the particular star is due to that stellar activity. Therefore we analyze the light curve of KIC 10403228 alone in this section.

To focus on the short-term noises, we remove the long-term variations by dividing the light curves into short segments and fitting each of them with polynomials. The more specific procedure is as follows. We exclude in-transit data as well as data around gaps in the light curve. From the remaining data, we pick up a segment of 6.18-day long light curve centered around a randomly chosen time and fit it with a quartic polynomial to remove the variation within the segment. Actually, one could use different functions (e.g. a spline function) or different time-window for detrending, but in any case the finals results are insensitive to these choices. For consistency, we adopt the same condition as that in Section 7.6.1.

We iterate "picking up a segment" and "detrending" procedures 1000 times and obtain 1000 segments of detrended light curves, whose centers are randomly distributed over the whole observing duration. We note that the total number of points in the detrended segments is $1000 \times 300 = 3.0 \times 10^5$, which is sufficiently large to sample all the original data points ($N = 10,000$). By averaging the 1000 detrended light curves at each time, we obtain one light curve. This averaging operation suppresses the dependence on the choice of the central time of each segment. Figure 7.11 shows the resulting detrended light curve (bottom) along with the light curve before detrending (top).

Now we move on to the comparison of the statistical property of stellar activities and the residuals of fit in Figure 7.8. Let us define $F_{\text{data}}(t)$ as the flux ratio of the detrended light curve with respect to the mean. To investigate the short-term correlation of stellar activities, we divide the light curves into continuously brightening events ($F_{\text{data}}(t) > 1$) and fading events ($F_{\text{data}}(t) < 1$). Then, we compute the duration and amplitude (average of the deviation from the mean $|F_{\text{data}}(t) - 1|$) for each event. For comparison, we also calculate the duration and average relative flux for events in residuals in Figure
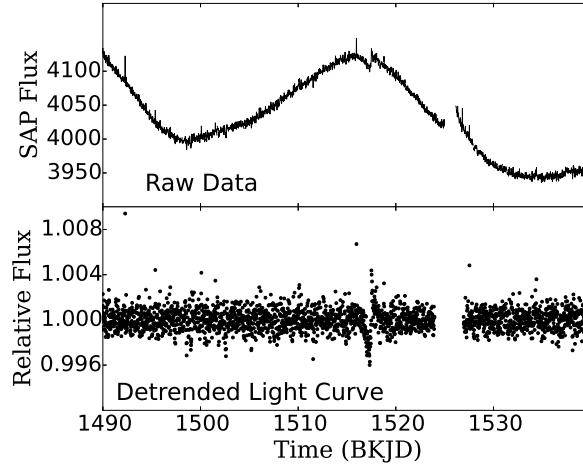
Figure 7.11: An example of a detrended light curve of KIC 10403228. The flare-like events are visible at several epochs. To create this curve, we generate 1000 light curves as described in the main text.

7.8. The left panel in Figure 7.12 is the scatter plot of the duration and average relative flux of events for three groups;

(a) all events out of the transit (the black data in Figure 7.11).

(b) residuals from fit of the ringed planet model (the red line in Figure 7.8).

(c) residuals from fit of the single planet model (the blue line in Figure 7.8).

The right panel in Figure 7.12 shows the distributions of duration of three groups. In each duration bin, the vertical axis shows the total number of points in all events with that duration. The distribution of (a) is normalized to give the same number of events as (b) and (c). The quoted error-bars are simply computed from Poisson statistics of the number of each event. Figure 7.12 shows that the distribution (b) is closer to (a) than (c). Thus, the ringed planet model is better than the planet model in terms of property of the correlated noise.

So far, we have shown that the ring-like anomaly cannot be explained statistically. We further consider whether the stellar noise can mimic the light-curve shape itself. We examine this hypothesis by focusing on the most significant fading event in the out-of-transit data; see the left panel of Figure 7.12. The light curve of this event is shown in Figure 7.13. We would like to see if the combination of the planet model and this event can reproduce the ringed-planet like feature. To do this, we appropriately embed the transit of the planet into the light curve around the fading event. Here, the parameters of the planet are the same in Table 7.3. Then we fit the two models with and without ring to those data, as shown in Figure 7.13 (b). As a result, we obtain the difference in χ^2 of two models with and without ring as 157.9, which is smaller than 434.9 obtained in Section 7.6.1 for solution 2. Thus, we conclude that it is difficult to reproduce the ring candidate by combining the stellar activities and the transit of the planet.
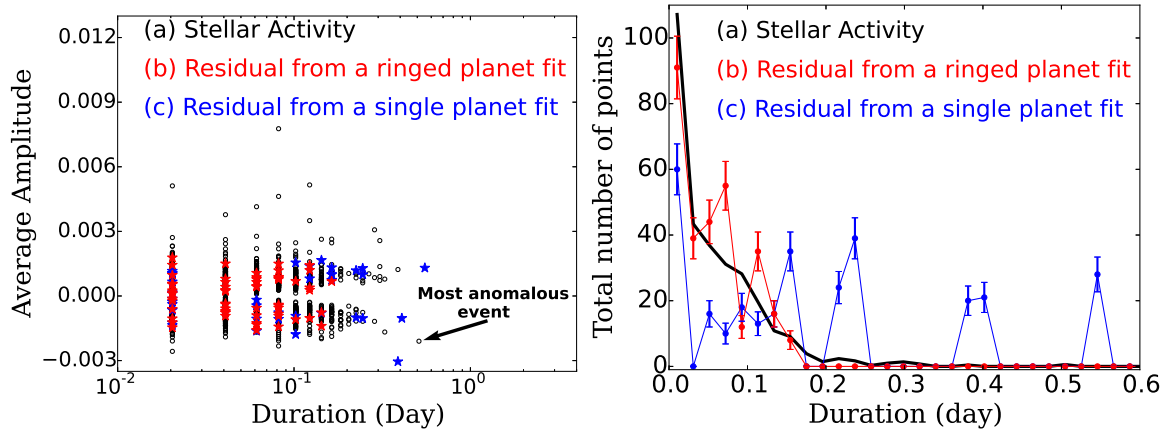
Figure 7.12: Statistical property of stellar activities of KIC10403228 and the residuals in Figure 7.8. (Left) Duration and average amplitude of continuously brighting ($F(t) > 1$) and fading ($F(t) < 1$) events are plotted. The black points are plotted from the stellar activities in Figure 7.11, and red points and blue points are plotted from the residuals of a ringed planet and a single planet model fitting in Figure 7.8 respectively. (Right) Histogram of duration. The color has the same meaning as in the left panel.
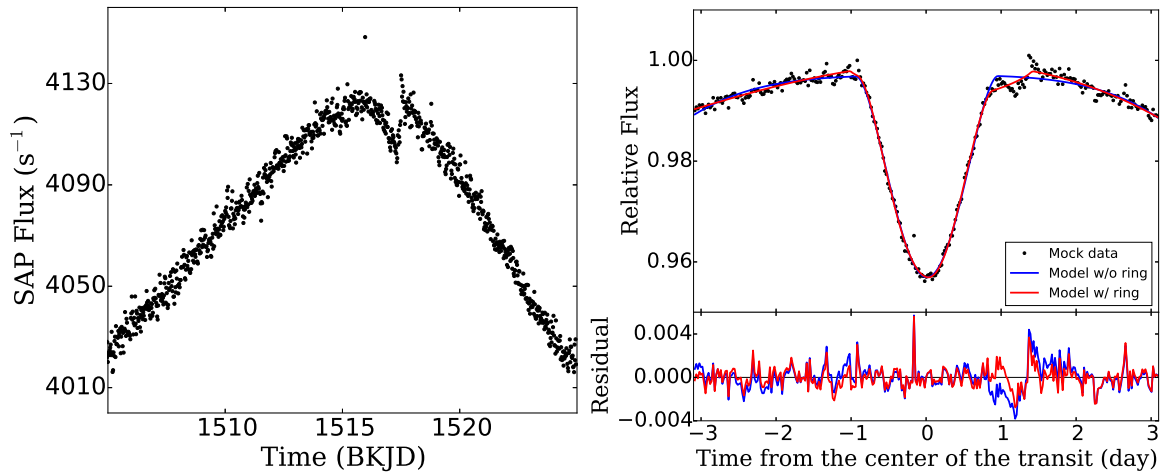
Figure 7.13: Testing the model of a transit of a planet with the stellar activities. (left) The most significant anomaly in KIC 10403228 as indicated with an arrow in the left panel of Figure 7.12. (right) The light curve of the transit of the planet embedded into the event in the left figure. The data are fitted with the ringed planet model (red) and the planet alone model (blue). The results show $\Delta\chi^2 \simeq 157.9$, which is smaller than the real value $\Delta\chi^2 = 434.8$ in Section 7.6.1.

Combination of the above mechanisms

In principle, a combination of the mechanisms discussed above could be invoked to reproduce the observed anomaly. In Figure 7.10, for example, the bump and dip in the residual might be explained separately by the spot crossing and the exomoon. However, such a probability is a priori very low, and so we do not discuss those possibilities any further.

7.6.4 Test of validity of the planetary hypothesis with VESPA

So far, we assume that the main transit signal comes from a planet. However, the V-shape of the transit (Figure 7.8) is also a typical feature of the eclipsing binary, and the estimated period ~ 450 yrs may be too long to be detected in four years of *Kepler*'s observation (Equation (7.12)). Therefore, we would like to compare the plausibilities of the eclipsing-binary and planet scenarios using the public code VESPA (Validation of Exoplanet Signals using a Probabilistic Algorithm) (Morton 2012, 2015). To be more specific, we compare the likelihoods of the following four scenarios; "HEBs (Hierarchical Eclipsing Binaries)", "EBs (Eclipsing Binaries)", "BEBs (Background Eclipsing Binaries)", and "Planets" (Transiting Planets) adopting a variety of different periods.

We adopt JHK-magnitudes from 2MASS (J-mag = 13.429 ± 0.028, H-mag = 12.793 ± 0.03, and K-mag = 12.518 ± 0.027), (RA, Dec) = ($19^{\mathrm{h}}\,24^{\mathrm{m}}\,54.413^{\mathrm{s}}$, $+47° \, 32' \, 57.5''$), maxrad = 3.0 arcsec (angular radius of the simulated region), Kepmag = 16.064, and $R_{\mathrm{p}}/R_{\star} = 0.3$. In reality, those observed colors might be contaminated by the nearby star discussed in Section 7.5.3, but we assume that the contamination is sufficiently small in the present analysis. Given these inputs, VESPA calculates the star populations and the probability distribution of transit shape parameters for the above four scenarios. For our adopted set of input parameters, VESPA identifies the primary star as an M dwarf, consistently with the classification of Dressing & Charbonneau (2013). We repeat the simulation ten times with different initial random numbers according to the prescription of VESPA.

Figure 7.14 shows the relative probability of each scenario for different assumed periods. We define the relative probability as the product of the "prior" and "likelihood" computed by VESPA, multiplied by 1000 days/P. The last factor 1000 days/P corrects for the probability that a long-period transit is observed in a given observing duration much shorter than the orbital period, which is not taken into account in the "prior" of VESPA. The plot shows the medians and the standard deviations of the probabilities computed from 10 sets of simulations. While the binary scenarios are more likely than the planet scenario for the shortest and the longest periods investigated here, Planets scenario is the most preferred in the intermediate region (10 years $\lesssim P \lesssim 100$ years). The result suggests that the planetary interpretation of the light curve is not so unlikely, although there is a fair amount of probability that this is a false positive. Another important implication of Figure 7.14 is that the likelihood of orbital periods in Planets scenario is much broader than what we intuitively thought
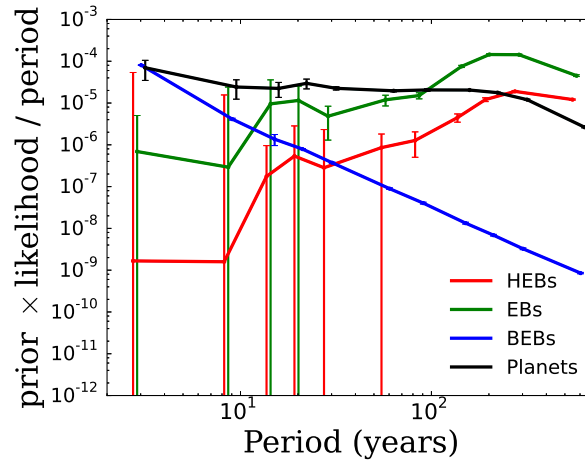
Figure 7.14: Relative probability of different models against adopted periods. The values in the vertical axis include the prior and likelihood factors, and the observational probability. Each point is slightly offset for visibility.

before, and not sharply peaked around 450 years.

While Figure 7.14 represents our final result from VESPA, we point out two additional factors that may be of importance for more detailed arguments.

First, the period distribution and the overall fraction of long-period planets and binaries have not been taken into account. Occurrence rate of giant planets around M dwarfs is given by Clanton & Gaudi (2016). They estimated the frequency of the planets with $10^2 M_\oplus < M_\mathrm{p} < 10^3 M_\oplus$ to be $0.039^{+0.042}_{-0.025}$ for 10^3 days $< P < 10^4$ days and $0.013^{+0.025}_{-0.010}$ for 10^4 days $< P < 10^5$ days. On the other hand, Janson et al. (2012b) estimated the multiplicity distribution of the binaries in 3–227 AU and found the overall occurrence rate 0.27 ± 0.03 peaked around 10 AU. These results imply that planets around M dwarfs is rarer than its stellar companion smaller by one or two orders of magnitude. This difference in the overall frequency may further increase the relative plausibility of the EB scenario compared to the Planets scenario.

Second, what also matters in reality is the frequency of the sources that produce the observed anomaly in addition to the transit signal. For example, while we consider a planetary ring as such a source in the Planets scenario, structures like a circumstellar disk would also produce a similar feature in the binary scenarios as well. It is, however, far beyond our current knowledge to estimate these factors rigorously. Given these difficulties, follow-up spectroscopy or high-resolution imaging would be more feasible to distinguish the two scenarios (EBs and Planets).

Chapter 8

Conclusion and Future prospects

Findings of exomoons and exoplanetary rings have been still attracting and also challenging goals in the field of planetary sciences. In the current situation, while the exomoons are systematically surveyed by several groups (e.g Hippke 2015; Kipping et al. 2012), the exoplanetary rings are explored by only one group, which focused on hot planets (Heising et al. 2015). The noteworthy fact is that the cold exoplanets like Saturn have not been investigated in the context of planetary rings.

In this thesis, we review some basics for searching for rings, present a methodology to detect exoplanetary rings and apply it to the 89 *long-period* planet candidates in the *Kepler* sample for the first time. After fitting a single planet model to light curves of target objects, we classify them into four groups depending on the observed anomalies and model predictions. Assuming grazing ringed planet planets, we obtain upper limits on $R_{\rm out}/R_{\rm p}$ for 12 planet candidates, and we find $R_{\rm out}/R_{\rm p} < 1.5$ for six of them. While we select five preliminary ringed planet candidates using the results of classification, four of them turn out to be false positives, but KIC 10403228 still remains as a possible ringed-planet system.

The estimated period of KIC 10403228 is long, P=450 years, and therefore the expected number of the transit for us to encounter during the 4 year mission of *Kepler* is 0.045. The interpretation of the number is complicated; it is true that this is not big, but not unlikely to be observed by chance. Therefore we perform further detailed analysis to examine the reality of the hypothesis fully assuming the signal is originated from the planetary transit. We fit the ringed planet model to the light curve of KIC 10403228, and find two consistent solutions with the tilted ring. We also consider in detail several possibilities other than the ringed planet hypothesis, including contamination from the nearby star, the oblateness of the planet, temporal stellar activities, spot-crossing, and gravity darkening. We find that none of these hypotheses is able to explain the ring-like anomaly better than the ringed-planet prediction. Therefore we conclude that the ringed planet is the most likely explanation to account for the observed anomaly of the transiting light curve of KIC 10403228 at this point. In the above discussions, however, we assume that the signals come from the planetary transit, so we also test this hypothesis using VESPA (Morton 2012, 2015). According to the VESPA result, "Planet" and "EB" scenarios are equally possible, and it is hard to

distinguish one theoretically. Therefore, we plan to attempt the follow-up observation instead.

　　The current research can be improved in several different ways. We can enlarge the sample of target objects towards those with shorter orbital periods. The interpretation of KIC 10403228 is fundamentally limited by the fact that it exhibits the transit only once. Obviously the credibility significantly increases if a system exhibits a robust ring-like anomaly repeatedly in the transits at different epochs. Our current methodology puts equal weights on the light curve over the entire transit duration. Since the signature of a ring is particularly strong around the ingress and egress phases as shown in Section 7.3, more useful information on $R_{\mathrm{out}}/R_{\mathrm{p}}$ would be obtained with more focused analysis of the features around those epochs. We plan to improve our methodology, and attempt to apply it to a broader sample of transiting planets in due course. Especially, as seen in Chapter 6, the hot planets have potentially harbor the rock rings, and their detections would give an impact on the field of planetary rings. Through these researches, we do hope that we will be able to affirmatively answer a fundamental question "Are planetary rings common in the world?".

Acknowledgments

First of all, I would like express my gratitude and respect to my supervisor, Yasushi Suto. After the discussions with him, my manuscripts and ideas are always improved dramatically. In addition, I am always deeply impressed by his positive attitude to everything including science.

I would like to show my gratitude to Kento Masuda, who gladly took time to discuss with me and generously shared his clever ideas. I have learned a lot of important things including the attitude to science from him. I am also grateful to Hajime Kawahara, who is one of my collaborators and occasionally comes to my desk to discuss recent topics. His aggressiveness toward science and broad knowledge of planetary sciences always stimulated me.

I thank Masamune Oguri, Daichi Suto, Shoya Kamiaka, and Taizo Okabe for attending my seminar and giving insightful comments to me. I also express my gratitude to all of the members in the theoretical astrophysics (UTAP) group for making a comfortable environment for research. In addition, I would like to give the special thanks to Souichiro Morisaki, Takahiro Kato, and Hiroaki Tahara. Thanks to them, I truly enjoyed my research life when I was a first-year graduate student.

Finally, I would like to thank my family, who always respect my decisions and support me in various ways.

Appendix A

Numerical integration in Equation (7.7)

We present a formulation for fast and accurate numerical integration of Equation (7.7). In addition to (x, y) coordinates defined in Section 7.2, we also introduce the cylindrical coordinates (r, θ), whose origin is at the center of the star. The ranges of (r, θ) integration are $0 < r < R_\star$ and $0 \le \theta < 2\pi$. We integrate Equation (7.7) by dividing the total range of integration into several pieces as follows:

$$
\int I(x, y) D(x, y) dS = \int_0^{R_\star} \int_0^{2\pi} I(\sqrt{1 - (r/R_\star)^2}) D(r, \theta) r dr d\theta
$$

$$
= \sum_i \sum_l D_{i,l} \int_{r_i}^{r_{i+1}} \int_{\theta_{i,l}(r)}^{\theta_{i,l+1}(r)} I(\sqrt{1 - (r/R_\star)^2}) r dr d\theta
$$

$$
= \sum_i \sum_l D_{i,l} \int_{r_i}^{r_{i+1}} (\theta_{i,l+1}(r) - \theta_{i,l}(r)) I(\sqrt{1 - (r/R_\star)^2}) r dr. \tag{A.1}
$$

The intervals of integration are specified by r_i and $\theta_{i,j}(r)$. We will define them in the following, and the corresponding schematic illustration is depicted in Figure A.1.

The number of the intersection points between a circle with the radius r and the ringed planet depends on the value of r; there exists boundary values r for the number of intersection points. We define r_i as the i-th boundary value, and we arrange a set of r_i in ascending order. If we have elements $r_i > R_\star$, we insert $R_\star$ into the set of r_i, and exclude elements that satisfy $r_i > R_\star$.

Next, let us suppose $r_i < r < r_{i+1}$, where the number of intersections remains the same. In this range, we define $\theta_{i,j}(r)$ to be the j-th value of θ of the intersection points between a ringed planet and a circle with the radius r. A set of $\theta_{i,j}(r)$ is also rearranged in ascending order, and we add $0, 2\pi$ before and behind the set of $\theta_{i,j}(r)$. We define $D_{i,l}$ to be the values of $D(r, \theta, t)$ for $\theta_{i,l}(r) < \theta < \theta_{i,l+1}(r)$ and $r_i < r < r_{i+1}$. We will derive the equations for r_i and $\theta_{i,j}(r)$ in the rest of appendix.

72
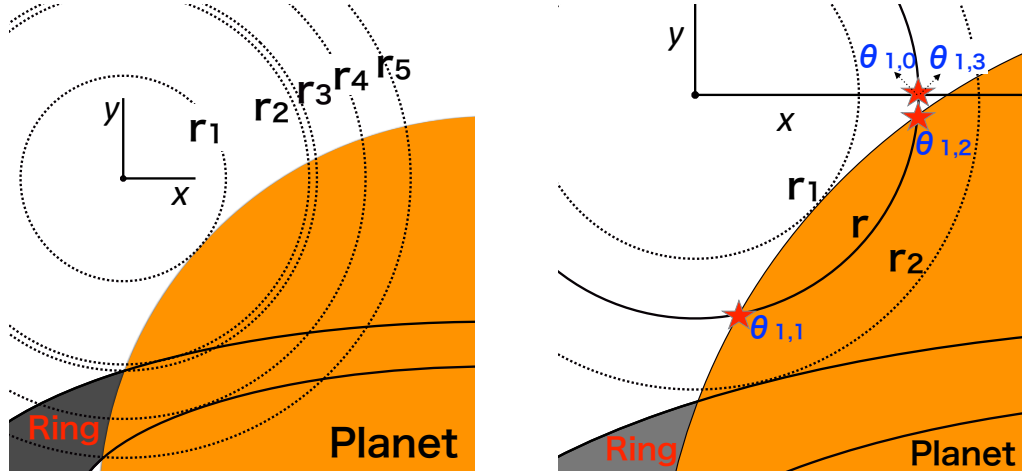
Figure A.1: Illustrations of r_i (left) and $\theta_{i,j}(r)$ (right). A ringed planet is depicted with colors. In the figure, the boundary lines of rings behind the planet are expressed for clarity.

A.1 Derivation of r_i

Conditions for possible values of r_i are divided into the following three cases:

(a) Intersections of the edge of the planet (circle) and the edge of the ring (ellipse).

(b) Extreme points of the distance function from the center of the star to the edge of the planet (circle).

(c) Extreme points of the distance function from the center of the star to the edge of the ring (ellipse).

The number of r_i is at most eight for (a), two for (b), and two for (c). (a) and (b) are reduced to quadratic equations, which can be easily solved. The last case can be reduced to quartic equations. Here, we derive the quartic equations using the method of Lagrange multiplier. Let the length of the major axis be $2R$ and that of the minor axis be $2R(1 - f)$, where f is the oblateness. We set the center of the ellipse to be at $(x_\mathrm{p}, y_\mathrm{p})$. For (x, y) on the edge of the ellipse, we define the following function:

$$A(x, y, \lambda) = x^2 + y^2 + \lambda \left[\left(\frac{x - x_\mathrm{p}}{R} \right)^2 + \left(\frac{y - y_\mathrm{p}}{R(1 - f)} \right)^2 - 1 \right].f \tag{A.2}$$

From the condition, we need

$$\frac{\partial A}{\partial x} = 2x + \frac{2(x - x_p)\lambda}{R^2} = 0 \tag{A.3}$$

$$\frac{\partial A}{\partial y} = 2y + \frac{2(y - y_p)\lambda}{(1 - f)^2 R^2} = 0 \tag{A.4}$$

$$\frac{\partial A}{\partial \lambda} = \left(\frac{x}{R} \right)^2 + \left(\frac{y}{R - Rf} \right)^2 - 1 = 0 \tag{A.5}$$

We reduce the above three equations to the following:

$$\frac{\lambda^4}{(1-f)^4 R^8} + \frac{2\lambda^3}{(1-f)^2 R^4}\left[\frac{1}{R^2} + \frac{1}{(1-f)^2 R^2}\right]$$
$$+ \lambda^2 \left[\frac{1}{R^4} + \frac{4}{(1-f)^2 R^4} + \frac{1}{(1-f)^4 R^4} - \frac{x_\mathrm{p}^2}{(1-f)^4 R^6} - \frac{y_\mathrm{p}^2}{(1-f)^2 R^6}\right]$$
$$+ \lambda \left[\frac{2}{R^2} + \frac{2}{(1-f)^2 R^2} - \frac{x_\mathrm{p}^2 + y_\mathrm{p}^2}{(1-f)^2 R^4}\right] + 1 - \frac{x_\mathrm{p}^2}{R^2} - \frac{y_\mathrm{p}^2}{(1-f)^2 R^2} = 0. \qquad (A.6)$$

In general, quartic equations are analytically solved, but we compute the solutions for the equation using a root-finding algorithm, because of complexity of the analytic solution. x and y are calculated from derived λ as follows:

$$x = \frac{-x_\mathrm{p}}{1 + (\lambda/R^2)} + x_\mathrm{p}, \; y = \frac{-y_\mathrm{p}}{1 + (\lambda/((1-f)R)^2)} + y_\mathrm{p}. \qquad (A.7)$$

The number of solutions for (x, y) is at most four. We exclude the solutions including complex numbers and/or (x, y) not on the ellipse. Equation (A.7) gives the singular solutions when

$$\lambda = -R^2, \; -(1-f)^2 R^2. \qquad (A.8)$$

Inserting the above values into Equation (A.3) or (A.4), we find $x_\mathrm{p} = 0$ or $y_\mathrm{p} = 0$. In this case, we cannot use Equation (A.7), but the conditions are reduced to the quadratic equations, which can be easily solved.

A.2   Derivation of $\theta_{i,l}(r)$

To derive $\theta_{i,l}(r)$, we calculate the intersections of a circle, centered at $(0, 0)$, with the radius r, and a transiting object, composed of the circle (planet) and two ellipses (rings). The center of the ring system is $(x_\mathrm{p}, y_\mathrm{p})$. The intersections of two circles are easily computed and the number of the intersection points is two at most. Here, we derive the equations for intersection points of a circle and an ellipse. Let the radius of the circle be r. We select the same ellipse as before. For simplicity, we introduce the following parameters:

$$A = 1 - (1-f)^2, \; B = 2x_\mathrm{p}(1-f)^2,$$
$$C = (1-f)^2 R^2 - r^2 - (1-f)^2 x_\mathrm{p}^2 - y_\mathrm{p}^2, \; D = -2y_\mathrm{p}. \qquad (A.9)$$

Then, an equation for x, the x-coordinate of intersections, is given by:

$$A^2 x^4 + 2AB x^3 + (2AC + B^2 + D^2)x^2 + 2BC x + C^2 - D^2 r^2 = 0, \qquad (A.10)$$

Equation (A.10) is a quartic equation, which is analytically solved. We solve this equation with the root-finding method in the same way as before. The number of the solutions for this equation is four at most. In total, there are up to 10 possible solutions for $\theta_{i,l}(r)$.

A.3   Precision and computational time

To test the precision and the computational time in our scheme, we simulate a transit of a Saturn-like planet with $R_{\mathrm{p}}/R_{\star} = 0.083667$, $R_{\mathrm{in/p}} = 1.5$, $R_{\mathrm{out/p}} = 2.0$, $\theta = \pi/3$, $\phi = \pi/3$, $T = 1.0$. We take $P = 10759.3$ days, $a/R_{\star} = 2049.89$, $b = 0.5$, $q_1 = 0.49$, and $q_2 = 0.34$ for orbital parameters and stellar parameters. For comparison, we prepare another integration scheme, which adopts pixel-by-pixel integration around the planetary center (e.g. Ohta et al. 2009).

First, we check the precision of the integration of our proposed method by comparing the precision of the pixel-by-pixel integration methods with 5000×5000 pixels. As a result, two methods are in agreement to the extent of 10^{-7}. Thus, our proposed method achieves the numerical error less than 10^{-7}, which is much smaller than the typical noise in the *Kepler* data 10^{-4}.

Second, we check the computational time of our template. Our proposed method typically takes 3.0 ms for calculating one point and 200 s in fitting in Section 6.1. For comparison, we also check the computational time of the planetary transit using PyTransit package (Parviainen 2015), and we find that it takes 0.3 ms to computes all the 300 data points and 0.3 s in fitting in Section 7.6.1.

Finally, we compare our method with the pixel-by-pixel integration. If we set the pixel sizes to satisfy the same computational time as that of our method, the precision of the integration becomes 10^{-5} in the fiducial configurations. This precision depends on the configurations; it becomes 10^{-4} for if we adopt "$R_{\mathrm{p}} = 0.17$ and $b = 0.8$" and 3×10^{-6} for "$R_{\mathrm{p}} = 0.042$ and $b = 0.3$". In summary, when we need a high-precision model, one should use our proposed method, and, if not, one may use the pixel-by-pixel integration to save the amount of calculation.

Incidentally, in a practical case of fitting with the Levenberg-Marquardt algorithm, our method is useful in a sense that gives the smooth value of χ^2. This is because the smoothness is needed to calculate the differential values for χ^2 in LM method.

Appendix B

Method of target classification in Section 7.3

B.1 Concept

As we demonstrated in the main text, signatures of a ringed planet can be detected by searching for any deviation from the model light curve assuming a ringless planet. The deviation is, however, often very tiny and comparable to the noise level, and so careful quantitative arguments are required to discuss the presence or absence of the ring in a given light curve. In the following, we present a procedure to evaluate the detectability of a ring based on the comparison between the residual from the "planet-alone" model fit and the noise level in the light curve.

Let us denote one light curve including a transit by I_i ($i = 0, 1, \cdot, N_{\mathrm{data}}$), where N_{data} is the number of data points. We also define δ_i as the residual of fitting I_i with the planet-alone model. As a quantitative measure of this residual signal δ_i relative to the noise level, we introduce the following signal-to-noise ratio:

$$S/N = \frac{\sum_i \delta_i^2}{\sigma^2} = \frac{\sum_i \delta_i^2}{N_{\mathrm{data}}} \frac{N_{\mathrm{data}}}{\sigma^2} = \Delta^2 \frac{1}{(\sigma/\sqrt{N_{\mathrm{data}}})^2} \qquad \left(\Delta^2 \equiv \frac{\sum_i \delta_i^2}{N_{\mathrm{data}}}\right). \qquad (\mathrm{B.1})$$

In the last equality, we further define Δ^2 as the variance of the residual time series, and σ is evaluated as the standard deviation of the out-of-transit light curve. We use the subscript "obs" to specify the above quantities obtained by fitting the planet-alone model to the real observed data: $\delta_{i,\,\mathrm{obs}}$, S/N_{obs}, and Δ^2_{obs}.

On the other hand, we can also compute the corresponding values of δ_i, S/N, and Δ, by fitting the *simulated* light curve of a ringed planet with the planet-alone model. We denote these values as $\delta^2_{i,\,\mathrm{sim}}(p)$, $S/N_{\mathrm{sim}}(p)$, and $\Delta^2_{\mathrm{sim}}(p)$, where p represents the set of parameters of the ringed-planet model. If these values are sufficiently large compared to the noise variance (see Δ^2_{thr} below), the signal of the ringed planet is distinguishable from the noise. In addition, comparing these theoretically expected residual levels with observed ones, we can relate the observed residuals to the parameters of the ringed model, even in the absence of clear anomalies.

To simplify the following arguments, we mainly use Δ^2 instead of S/N to evaluate the significance of the anomaly (see also Section B.3 for detailed reason). Practically, conversion from one to the other is rather simple, as the conversion factor $\sigma/\sqrt{N_{\mathrm{data}}}$ is well determined from the observed data alone; given a transit light curve, the transit duration T_{dur} and the bin size t_{bin} give the number of data points $N_{\mathrm{data}} = T_{\mathrm{dur}}/t_{\mathrm{bin}}$, and the standard deviation σ can also be inferred from the out-of-transit flux.

For a given region of parameter space p, $\Delta^2_{\mathrm{sim}}(p)$ has the maximum value $\Delta^2_{\mathrm{max,sim}}$. If $\Delta^2_{\mathrm{max,sim}}$ is smaller than some threshold value Δ^2_{thr} determined by the noise level in the light curve, the ringed-planets with the corresponding value of p, even if they exist, cannot be detected in the system. Then, the comparison of Δ^2_{obs}, $\Delta^2_{\mathrm{max,sim}}$, and Δ^2_{thr} allows for classification into four categories schematically illustrated in Figure B.1:

(A) : $\Delta^2_{\mathrm{max,sim}} < \Delta^2_{\mathrm{thr}}$
The expected signal from the ring is so small compared to the noise level that we cannot discuss its detectability.

(B) : $\Delta^2_{\mathrm{obs}} < \Delta^2_{\mathrm{thr}} < \Delta^2_{\mathrm{max,sim}}$
Although the rings with $\Delta^2_{\mathrm{thr}} < \Delta^2_{\mathrm{sim}}(p)$ could have been detected, no significant anomaly is observed ($\Delta_{\mathrm{obs}} < \Delta_{\mathrm{thr}}$) in reality. Thus, the parameter region that gives $\Delta^2_{\mathrm{thr}} < \Delta^2_{\mathrm{sim}}(p)$ is excluded.

(C) : $\Delta^2_{\mathrm{thr}} < \Delta^2_{\mathrm{max,sim}} < \Delta^2_{\mathrm{obs}}$
A significant anomaly is detected, but its amplitude is too large to be explained by the ringed-planet model with the given range of p.

(D) : $\Delta^2_{\mathrm{thr}} < \Delta^2_{\mathrm{obs}} < \Delta^2_{\mathrm{max,sim}}$
A significant anomaly is detected, and its amplitude is compatible with the ring model. In this case, we may find the ring parameters consistent with the observed anomaly.

The value of Δ^2_{thr} is arbitrary. In this thesis, we choose Δ^2_{thr} so that it corresponds to $S/N = 10$ in Equation (B.1):

$$\Delta^2_{\mathrm{thr}} = \frac{10\,\sigma^2}{N_{\mathrm{data}}}, \tag{B.2}$$

where σ and N_{data} are calculated from the observed data. The methods to calculate the other variances, Δ^2_{obs}, $\Delta^2_{\mathrm{sim}}(p)$, and $\Delta^2_{\mathrm{max,sim}}$ will be presented in the following subsections.

Before proceeding further, let us consider the orbital period dependence of $N_{\mathrm{data}} = T_{\mathrm{dur}}/t_{\mathrm{bin}}$ in Equation (B.1). From Kepler's third law, $T_{\mathrm{dur}} \propto P\,(R_\star/a) \propto P^{1/3}$. For the short-period planets, $t_{\mathrm{bin}} \propto P$ because the number of folded transits is proportional to $1/P$. Thus, the number of the data $T_{\mathrm{dur}}/t_{\mathrm{bin}}$ is proportional to $P^{-2/3}$. This means that the detectability of rings (S/N) is higher for the shorter-period planets for a given value of Δ^2. This explains the strong constraints on the ring parameters obtained by Heising et al. (2015) for hot Jupiters.
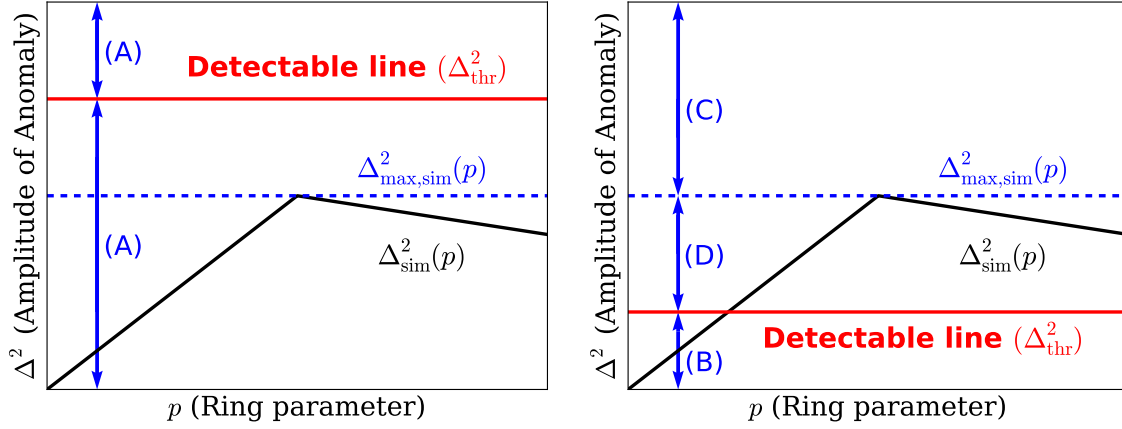
Figure B.1: Classification using $\Delta_{\mathrm{thr}}^2, \Delta_{\mathrm{obs}}^2$, and $\Delta_{\mathrm{sim}}^2(p)$. Candidates are classified into (A)~(D) depending on the value of Δ_{obs}^2. (Left) $\Delta_{\mathrm{max,sim}}^2 < \Delta_{\mathrm{thr}}^2$. The detectability of rings is small. (Right) $\Delta_{\mathrm{thr}}^2 < \Delta_{\mathrm{max,sim}}^2$. The detectability of rings is large.

B.2 Calculation of Δ_{obs}^2

B.2.1 Definition

The residual $\delta_{i,\mathrm{obs}}$ is obtained by fitting the planet-alone model to the data. If the ring does not exist, the value of S/N_{obs} in Equation (B.1), which is formally equivalent to the chi-squared, is expected to be close to the degree of freedom DOF_{obs}. In contrary, if the ring does not exist, $S/N_{\mathrm{sim}}(p)$ is equal to zero. This mean that $S/N_{\mathrm{obs}} - S/N_{\mathrm{sim}}(p) \simeq DOF_{\mathrm{obs}}$ in the limit of the non-ring system. Thus, for comparison of $\Delta_{\mathrm{sim}}^2(p)$ and Δ_{obs}^2, the value of $(S/N - DOF_{\mathrm{obs}})$ serves as a good estimator of the observed anomaly rather than S/N. We thus slightly modify Equation (B.1) to define Δ_{obs}^2 so that it corresponds to $(S/N - DOF_{\mathrm{obs}})$:

$$\Delta_{\mathrm{obs}}^2 = \left(\chi^2 - DOF_{\mathrm{obs}} \right) \frac{1}{(\sigma/\sqrt{N_{\mathrm{data}}})^2}, \tag{B.3}$$

where

$$\chi^2 = \sum_i \left(\frac{\delta_{i,\mathrm{obs}}}{\sigma} \right)^2. \tag{B.4}$$

The residual $\delta_{i,\mathrm{obs}}$ is defined for the best-fit planet-alone model obtained by minimizing χ^2 as described in Section B.2.2 below. The value of χ^2 is computed using the data just around the transit (within $0.6\,T_{\mathrm{dur}}$ from the transit center) so that the value is not strongly affected by the out-of-transit data. We assume $DOF_{\mathrm{obs}} = N_{\mathrm{data}} - N_{\mathrm{para}} - 1$, where N_{para} is the number of fitted parameters.

B.2.2   Detail of fitting

In fitting, we minimize χ^2 using the Levenberg-Marquardt algorithm by implementing cmpfit (Markwardt 2009). The adopted model $M(t)$ is composed of a fourth-order polynomial and a transit model $F(t)$:

$$M(t) = F(t)[c_0 + c_1(t - T_0) + c_2(t - T_0)^2 + c_3(t - T_0)^3 + c_4(t - T_0)^4], \qquad (\mathrm{B.5})$$

where c_i are coefficients of polynomials, and T_0 is a time offset. The polynomials are used to remove the long-term flux variations in the light curve. The transit model $F(t)$ is implemented by the PyTransit package (Parviainen 2015). PyTransit generates the light curves based on the model of Mandel & Agol (2002) with the quadratic limb darkening law.

The above model $M(t)$ includes 12 parameters, $t_0, R_{\mathrm{p}}/R_\star, b, a/R_\star, P, q_1, q_2,$ and $c_i \, (i = 0 \sim 4)$. For KOIs, the initial values of $a/R_\star, R_{\mathrm{p}}/R_\star,$ and b for fitting are taken from the KOI catalog. The initial values of the limb darkening parameters are taken from the *Kepler* Input Catalog. For a single transit event, where we cannot estimate the orbital period from the transit interval, we choose P, instead of $a/R_\star$, as a fitting parameter and estimate $a/R_\star$ from P using Kepler's third law and the mean stellar density given in the catalog.

In fitting, we remove outliers iteratively to correctly evaluate χ^2. We first fit all the data with the model $M(t)$, and flag the points that deviate more than 5σ from the best model. We then refit only the non-flagged data using the same model, and update the flags of *all* the original data points, including the ones classified as outliers before, on the basis of the new best model and the same 5σ criterion. We iterate this procedure until the flagged data are converged. While this process gives a more robust evaluation of χ^2, it may also erase the signature of the ringed planet; thus we visually check all the light curves in any case not to miss the real ringed planets.

The noise variance σ^2 is estimated for each transit light curve by fitting the out-of-transit light curve with a fourth-order polynomial, and calculating the variance of the residuals. Flare-like events are excluded from the estimation of the noise variance.

B.3   Calculation of $\Delta^2_{\mathrm{sim}}(p)$ and $\Delta^2_{\mathrm{sim,max}}$

Since the parameter space p for a ringed planet is very vast, we wish to reduce the volume we need to search with simulations as much as possible. First we show that $\Delta^2_{\mathrm{sim}}(p)$ does not depend on P and $a/R_\star$ with other parameters fixed including limb darkening parameters q_1, q_2, the transit impact parameter b, planet-to-star radius ratio $R_{\mathrm{p}}/R_\star$, inner and outer ring radii relative to the planetary radius $r_{\mathrm{in/p}}$ and $r_{\mathrm{out/p}}$, , the direction of the ring (θ, ϕ), and a shading parameter T. This property becomes apparent by rewriting $\Delta^2_{\mathrm{sim}}(p)$ into the following integral form approximately, assuming

that the sampling rate (t_{bin}) is sufficiently small compared to the duration T_{dur}:

$$\Delta^2_{\mathrm{sim}}(p) \simeq \frac{\int_{-T_{\mathrm{dur}}/2}^{T_{\mathrm{dur}}/2} \delta^2_{\mathrm{sim}}(t, p)dt}{\int_{-T_{\mathrm{dur}}/2}^{T_{\mathrm{dur}}/2} dt} = \frac{\int_{-1/2}^{1/2} \delta^2_{\mathrm{sim}}(T_{\mathrm{dur}}t', p)dt'}{\int_{-1/2}^{1/2} dt'} = \int_{-1/2}^{1/2} \bar{\delta}^2_{\mathrm{sim}}(t', p)dt', \quad \text{(B.6)}$$

where

$$\bar{\delta}_{\mathrm{sim}}(t, p) \equiv \delta_{\mathrm{sim}}(T_{\mathrm{dur}}t, p) \tag{B.7}$$

and the origin of time is shifted to the transit center. Assuming that the values of q_1, q_2, b, $R_{\mathrm{p}}/R_\star$, $r_{\mathrm{out/p}}$, $r_{\mathrm{in/p}}$, θ, ϕ, and T are fixed, $\bar{\delta}(t, p)$ defined above does not depend on T_{dur} explicitly. Therefore, $\Delta^2_{\mathrm{sim}}(p)$ given by Equation (B.6) does not depend on the time scale of the transit T_{dur}, which is determined by P and $a/R_\star$, and we do not need to simulate the dependence of $\Delta^2_{\mathrm{sim}}(p)$ on these two parmeters.

To constrain the parameter space further, we use the observed transit depth. This is because there is a significant correlation between the transit depth and Δ^2 as discussed in Appendix D. Here we also assume that the values of q_1, q_2, b, T, $r_{\mathrm{in/p}}$, and the ring direction are fixed and that $R_{\mathrm{p}}/R_\star$ and $r_{\mathrm{out/p}}$ are the only free parameters. Then, the constraint on the observed transit depth leaves only one degree of freedom, specified by contours in the $R_{\mathrm{p}}/R_\star$-$r_{\mathrm{out/p}}$ plane; henceforth we rewrite $\Delta^2_{\mathrm{sim}}(p)$ as $\Delta^2_{\mathrm{sim}}(r_{\mathrm{out/p}})$ to explicitly show this dependence.

To compute the relation $\Delta^2_{\mathrm{sim}}(r_{\mathrm{out/p}})$ for a given transit depth, we first calculate the value of Δ^2_{sim} and the transit depths for a sufficient number of points in the $(r_{\mathrm{out/p}}, R_{\mathrm{p}}/R_\star)$ plane. The necessary number of points depends on the fiducial model, and, in our simulation, we prepare about two hundred points for each model in Table 7.1. For any $r_{\mathrm{out/p}}$, the observed transit depth uniquely translates into $R_{\mathrm{p}}/R_\star$ by the interpolation in the $R_{\mathrm{p}}/R_\star$-transit depth plane, because the transit depth is a monotonically increasing function of the $R_{\mathrm{p}}/R_\star$. Thus, the given value of $r_{\mathrm{out/p}}$ is uniquely related to Δ^2_{sim} given the transit depth. By repeating this procedure for many different values of $r_{\mathrm{out/p}}$, we can compute the relation $\Delta^2_{\mathrm{sim}}(r_{\mathrm{out/p}})$. We note that once a sufficient number of interpolated lines are prepared, one transit depth determines the relation $\Delta^2_{\mathrm{sim}}(r_{\mathrm{out/p}})$ without additional calculation.

Figure B.2 shows $\Delta^2_{\mathrm{sim}}(r_{\mathrm{out/p}})$ curves created in this way, for $4 \times 4 = 16$ different sets of impact parameters, ring directions, and transit depths. The four sets of p adopted here (model I $\sim$ model IV) are summarized in Table 7.1, and four transit depths are chosen to be 0.001, 0.005, 0.01, and 0.05. We fix $T = 1$ and $r_{\mathrm{in/p}} = 1$ in all of these simulations.

Here we simulate $\Delta^2_{\mathrm{sim}}(r_{\mathrm{out/p}})$ only for $1 \leq r_{\mathrm{out/p}} \leq r_{\mathrm{eq}}$, where r_{eq} is the value of $r_{\mathrm{out/p}}$ for which the minor axis of the sky-projected outer ring is equal to the planetary radius, computed for each model. This is because the value of $\Delta^2_{\mathrm{sim}}(r_{\mathrm{out/p}})$ shows no $R_{\mathrm{p}}/R_\star$ dependence beyond r_{eq}, when $T = 1$ and $r_{\mathrm{in/p}} = 1$ are adopted; if this is the case, the planetary disk is within the outer disk and the transit depth is solely determined by the latter.

In this thesis, we only use the observed constraint on the transit depth. However, this is just for simplicity and we can certainly take into account the constraints on

other parameters including b, q_1, and q_2 from the morphology of the observed transit light curve (e.g. egress and ingress durations). Such constraints further restrict the ring models that could be consistent with the observed light curve and thus help more elaborate discussions on the ring parameters, which we leave to future works.
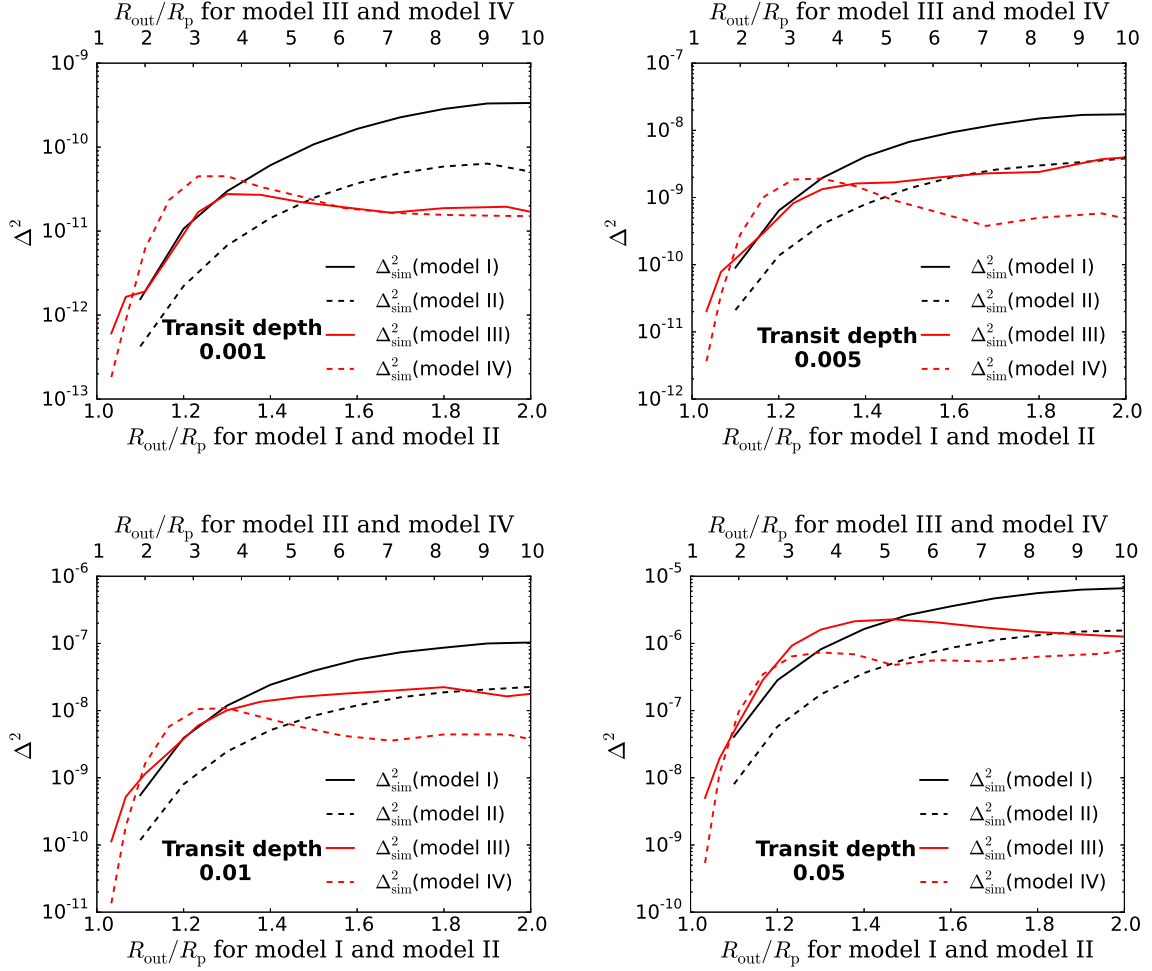
Figure B.2: The value of $\Delta^2_{\mathrm{sim}}(p)$ as a function of $r_{\mathrm{out/p}}$ for four different transit depths. The four lines in each panel correspond to four different sets of parameters (model I $\sim$ model IV) summarized in Table 7.1.

Appendix C

Derivation of the upper limit of $r_{\mathrm{out/p}}$: case of KOI-1466.01

If a system is classified into group (B), the ring models with $\Delta^2_{\mathrm{thr}} < \Delta^2_{\mathrm{sim}}(r_{\mathrm{out/p}})$ are excluded. The upper limits of $r_{\mathrm{out/p}}$ thus obtained are summarized in Sections 4 and 5. Here we describe how the limit is derived using the relation $\Delta^2_{\mathrm{sim}}(r_{\mathrm{out/p}})$, taking KOI-1466.01 for example.

The black and red lines in Figure C.1 are theoretically expected signals from the ringed planets (i.e., $\Delta^2_{\mathrm{sim}}(r_{\mathrm{out/p}})$) for model I $\sim$ model IV and for the transit depth of 0.0202 inferred from the observed data. The green line shows the threshold value of Δ^2_{thr} that satisfies $S/N = 10$, and the blue line shows the observed residual level Δ^2_{obs} obtained by fitting the planet-alone model to the data. Here $\Delta^2_{\mathrm{obs}} < \Delta^2_{\mathrm{thr}}$, which means that no significant deviation from the planet-alone model is detected. In this case, we can in turn exclude the models above the green line, because any anomaly above this level should have been detected if present. In the case of the black solid line (model I), for example, the ring with $r_{\mathrm{out/p}} > 1.5$ would have produced the anomaly with $S/N > 10$, which is not detected in reality. Thus, we can set the upper limit of $r_{\mathrm{out/p}} < 1.5$ for model I. Note that the upper limits depend on the adopted parameter set; this situation is clearly illustrated in Figure C.1, where similar limits cannot be derived for the other models.
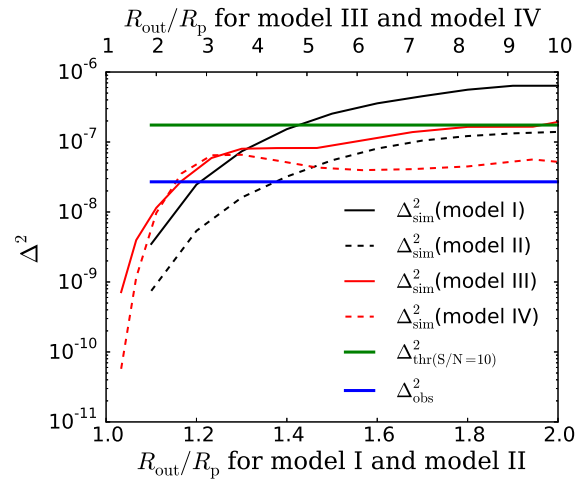
Figure C.1: Derivation of the upper limit of $r_{\mathrm{out/p}}$ in the case of KOI-1466.01. The observed signature of the ring in the blue line is small compared with the detectability of the ring shown in the green line. The red and black lines are the theoretically expected values of Δ^2 for models I-IV in Table 7.1. Assuming model I (black solid line), for example, the region with $1.5 < r_{\mathrm{out/p}}$ (i.e. a part of the line above the green line) is inconsistent with the non-detection of the anomaly and thus excluded.

Appendix D

General property of signal of transiting ringed planet

In this section, we show two important properties of signals of rings. One is the strong correlation between the signals and the size of the systems. The other is the concentration of the signals around the edge of the transits.

To reveal these general properties, we prepare a sufficient number of sets of parameters as shown in Table D.1; we change four parameters $R_{\rm p}, b, \theta, \phi$ with other parameters fixed, and there are 625 combinations in total. For all sets of parameters in Table D.1, we make the light curves and fit the ringless model to these mock data to calculate the signals. In fitting, we free $R_{\rm p}, b, a/R_\star, q_1, q_2, t_0$, and we use Levenberg-Marquardt Method. To obtain the nearly optimal solution, we iterate fitting processes 200 times using the randomly chosen initial parameters considering the fact that 100 iterations are enough to estimate the optimal solution. After obtaining the best model, we calculate the averaged squared sum of the residuals Δ^2 defined in Equation (B.1), and use it as the signals of rings.

Table D.1: Parameters for simulation

Parameters	Values	Meaning
(Fixed parameters)		
P(day)	10759.304	Period
u_1	0.2925	Limb darkening parameter
u_2	0.475	Limb darkening parameter
t_0(day)	0	Time of a transit center of a planet
T	1.0	Shading coefficient
$R_{\rm in}/R_{\rm p}$	1.5	Ratio of $R_{\rm in}$ to $R_{\rm p}$
$R_{\rm out}/R_{\rm in}$	1.3333	Ratio of $R_{\rm out}$ to $R_{\rm in}$
(Variable parameters)		
$R_{\rm p}/R_\star$	$0.08366(=R_{\rm J}/R_\odot) \times X$	Planet to star radius ratio
X	0.3, 0.6, 1.0, 1.5, 2.0	
$b(= a\cos i/R_\star)$	0.1, 0.3, 0.5, 0.7, 0.9	Impact parameter of the transit when $e = 0$
θ (deg)	18, 24.75, 31.5, 38.25, 45	Angle between Y-axis and axis of the ring
ϕ (deg)	0, 11.25, 22.5, 33.75, 45	Angle between Z-axis and ring-axis projected onto (Z, X)-plane

First, we investigate the relation between Δ^2 and parameters. Figure D.1 and D.2

show the plot of Δ^2 and one of parameters (X, b, θ, ϕ). For example, the left in Figure D.1 shows the plot of Δ^2 and X. In the plot, we can see the scattering of Δ^2 at a fixed X, and this comes from the various combinations of other parameters (b, θ, ϕ). Among these four plots, we clearly find the significant correlation between Δ^2 and X. The relation Δ^2 and X can be explained as follows. First let us remind that the signals of rings are arising from the difference between the assumed ringed planet and the corresponding best fit non-ringed planet. Then, if we assume the large ringed planet, the corresponding planet obtained from fitting also becomes large, and the difference between them becomes also large. The difference between them is exactly the signals of rings, so the large size of the system leads to the large anomalies from rings. In this way, the size of the system is very correlated with the evidence of rings. Here, we only consider the dependence on $R_{\mathrm{p}}/R_{\star}$, but we also confirm that $R_{\mathrm{out/in}}$ and $R_{\mathrm{in/p}}$, that determines the size, is also strongly correlated with Δ^2 like $R_{\mathrm{p}}/R_{\star}$. We finally note that we cannot ignore the large variance due to different combinations of (b, θ, ϕ) in spite of the strong correlation between Δ^2 and X, and the more discussion about Δ^2 is needed to fully understand its feature.

Second, we investigate to what extent the signals are concentrated around the edge of the transit. For this purpose, we calculate the sum of the residuals around the transit edge, and then we compare it with the total anomalies in the light curve. For clarity, we define the former value as $\sum \delta_{\mathrm{edge}}^2$ and the latter as $\sum \delta_{\mathrm{tot}}^2$. The detailed procedure of calculation of these values is as follows. First, we divide the light curve during the transit into the edge of transit (ingress and egress) and the other part. The edge is defined as the duration when the planet crosses the limb of the star. The assumed planet here has the parameters from each fitting to the mock data of ringed planets. Then, we compute the sum of residuals $\sum \delta_{\mathrm{edge}}^2$ around the edge to compare it with the sum of them during the full transit $\sum \delta_{\mathrm{tot}}^2$. In addition to residuals, we also record the durations for both cases as T_{edge} and T_{full}.

After the analysis, we obtain $\sum \delta_{\mathrm{edge}}^2$, $\sum \delta_{\mathrm{tot}}^2$, T_{edge}, and T_{full} for all sets of parameters in Table D.1. To show the extent of the concentration, we plot $T_{\mathrm{edge}}/T_{\mathrm{full}}$ versus $\sum \delta_{\mathrm{edge}}^2 / \sum \delta_{\mathrm{tot}}^2$ in Figure D.1. In the upper left region in the plot, $T_{\mathrm{edge}}/T_{\mathrm{full}}$ is small and $\sum \delta_{\mathrm{edge}}^2 / \sum \delta_{\mathrm{tot}}^2$ is large, and the signals are highly concentrated around the edge. Especially, some cases show $\sum \delta_{\mathrm{edge}}^2 / \sum \delta_{\mathrm{tot}}^2 \simeq 1.0$ and $T_{\mathrm{edge}}/T_{\mathrm{full}} \simeq 0.0$. Thus, the signals can be significantly concentrated around the edge of the non-grazing transit. On the other hand, when $T_{\mathrm{edge}}/T_{\mathrm{full}} \simeq 1.0$, or the transit is grazing, the value of $\sum \delta_{\mathrm{edge}}^2 / \sum \delta_{\mathrm{tot}}^2$ is close to 1 because the edge cover most of the transit. In summary, when the transit is grazing, we may use the $\sum \delta_{\mathrm{tot}}^2$, and when the transit is non-grazing, we may use $\sum \delta_{\mathrm{edge}}^2$ to evade the unnecessary noises during the transit.
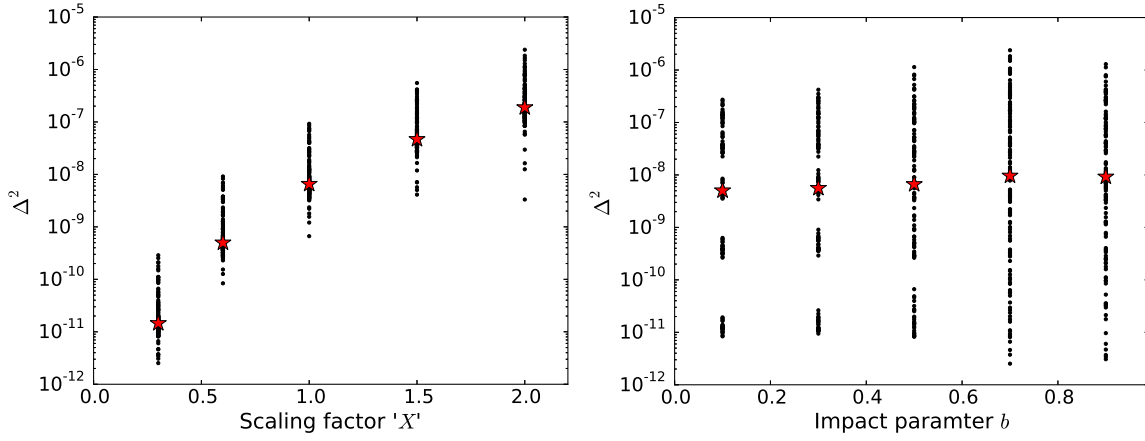
Figure D.1: (Left) Plot of scaling factor X versus Δ^2. In each bin of X, one point corresponds to one combination of (θ, ϕ, b), rhe red star shows a position of the median. (Right) Plot of scaling factor X versus b.
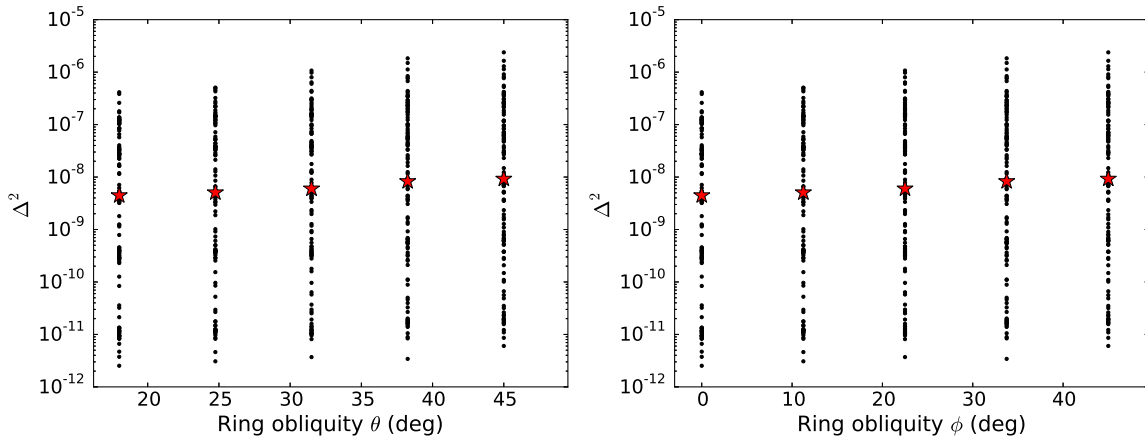
Figure D.2: (Left) Plot of scaling factor θ versus Δ^2. (Right) Plot of scaling factor ϕ versus Δ^2. The format is the same as that of Figure D.1.
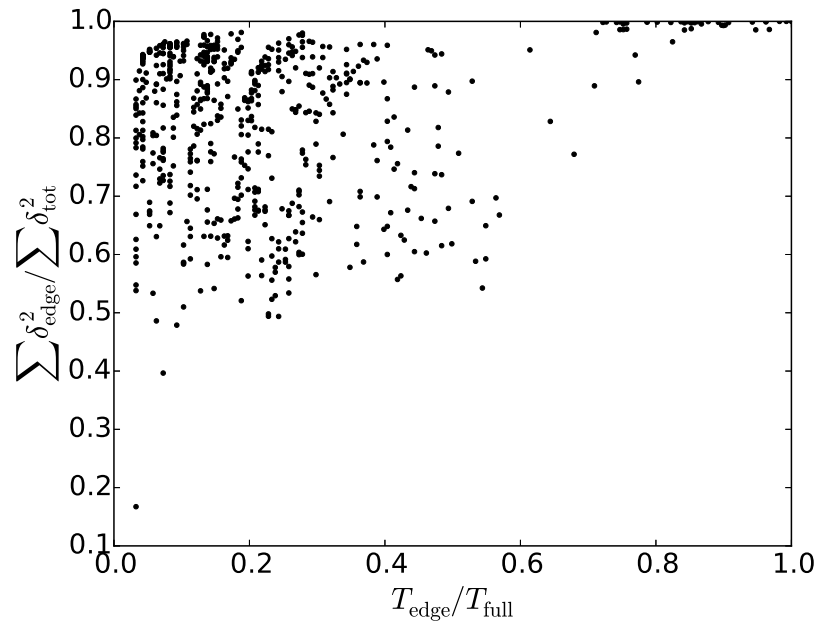
Figure D.3: Extent of concentration of ring signals around transit edge. The x-axis shows (edge duration)/(total duration) of the transit, and the y-axis shows (sum of residuals around edge)/(sum of residuals in transit).

Appendix E

Time-integration effect on signals of rings in transit photometry

Kepler has two modes; long-cadence mode (LC mode; 29.4 mins) and short-cadence mode (SC mode; 1 min). In these modes, the light curves are integrated for 29.4 mins or 1min, and they differ from the idealistic light curves without time integration (e.g. Kipping 2010). Indeed, the light curves taken in SC mode will be unaffected because almost all planetary transits last for at least several hours $\gg$ 1min in SC mode. However, there are only 500 stars monitored by *Kepler* in SC mode, and almost all stars are observed in LC mode. Therefore, to fully exploit the *Kepler* data for a ring search, we need to evaluate the degradation of the ring signals in LC mode – to what extent can we accept 30 mins integration for a search for rings? This is a question that we want to clarify in the following.

Hereafter, we adopt the same model as that used in Chapter 7. For the fiducial parameters, we adopt those of Saturn in Table E.1. In the simulation, we vary orbital period P, the size of the system $R_{\rm p}/R_{\star}$, and impact parameter b. For convenient, we adopt $R_{\rm p}/R_{\star} = X(R_{\rm J}/R_{\odot})$, where X is defined as a scaling factor. We also vary $a/R_{\star}$ along with the change of P through the Kepler law adopting the stellar density of the Sun $\rho_{\star} = 1.411$ gcm^{-3}. To simulate the data taken in LC mode, we integrate light curves for 29.4 mins.

Given the above setups, we create "time-integrated" and "non-time-integrated" light curves for a transit of a ringed planet. Then, we fit the non-ringed planet model to the simulated data to derive the signals of rings. In fitting, we use the "non-time-integrated" ringless model for the data simulated by "non-time-integrated" ringed planet model, and the other is in the same way. For comparison, we take signals of rings to be the sum of the residuals $\sum_i \delta_i^2$ in fitting defined in Section B.1. Using this specific value, we define Bin(p) as the ratio of the values of $\sum_i \delta_i^2$ obtained in integration and non-integration simulations with a set of parameters p:

$$\text{Bin}(p) = \frac{\int (y_{\text{ring, 29.4mins}}(t) - y_{\text{pla, fit, 29.4mins}}(t))^2 dt}{\int (y_{\text{ring,non}}(t) - y_{\text{pla,fit,non}}(t))^2 dt} \simeq \frac{\sum_i \delta_{i,\text{29.4 mins}}^2}{\sum_i \delta_{i,\text{ non}}^2}, \qquad \text{(E.1)}$$

where $y_{\text{ring, 29.4mins}}(t)$ is the timed integrated light curve for a ringed planet, $y_{\text{pla, fit, 29.4mins}}(t)$

is the best fitting time integrated light curve of a planetary transit for $y_{\text{ring, 29.4mins}}(t)$. $y_{\text{ring,non}}(t)$ and $y_{\text{pla,fit,non}}(t)$ are non-integrated light curves corresponding to $y_{\text{ring, 29.4mins}}(t)$ and $y_{\text{pla, fit, 29.4mins}}(t)$. The value of $\text{Bin}(p)$ is a good estimate of the time-integration effect on the ring signals. In fitting, we free all the planetary parameters and limb darkening parameters q_1 and q_2 except for the period. For the search for the solution, we minimize the squared sum of the residuals using the Levenberg-Marquardt algorithm by implementing cmpfit (Markwardt 2009).

Table E.1: Fiducial parameters

Parameters	Values	Meaning
(Fixed parameters)		
q_1	0.49	Limb darkening parameter
q_2	0.34	Limb darkening parameter
$t_0(\text{day})$	0	Time of a transit center of a planet
T	1.0	Shading coefficient
θ	0.438	Angle between Y-axis and axis of the ring
ϕ	1.0	Angle between Z-axis and ring-axis projected onto (Z, X)-plane
$R_{\text{in}}/R_{\text{p}}$	1.5	Ratio of R_{in} to R_{p}
$R_{\text{out}}/R_{\text{in}}$	1.3333	Ratio of R_{out} to R_{in}
(Variable parameters)		
$P(\text{day})$	1.0, 10.0, 30.0, 60.0, 100.0, 300.0, 1000.0, 3000.0, 10000.0	Period
$R_{\text{p}}/R_{\star}$	$0.08366(=R_{\text{J}}/R_{\odot}) \times X$	Planet to star radius ratio
X	0.1, 0.3, 0.6, 1.0, 2.0	Scaling factor for $R_{\text{p}}/R_{\star}$
$b(= a\cos i/R_{\star})$	0.1, 0.7	Impact parameter of the transit when $e = 0$
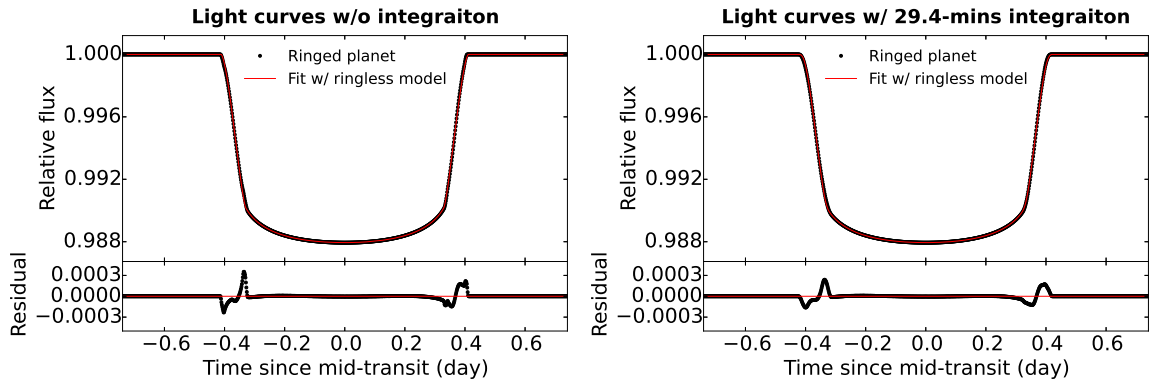
Figure E.1: Example of time-integration effect with $P = 3000$ days and $X = 1.0$. The right takes into account the 29.4-mins integration while the left does not. In the upper side, a light curve of a ringed planet during the transit (black) and its best-fit model with a ringless model (red) are shown. In the bottom, the residuals from fitting are shown.

First, we set $b = 0.1$ and change the values of P and $R_{\text{p}}/R_{\star}$. Figure E.1 shows one example of the integrated and non-integrated light curves of a ringed planet with $P = 3000$ days and $X = 1.0$. The bottom in the figure shows the residuals from
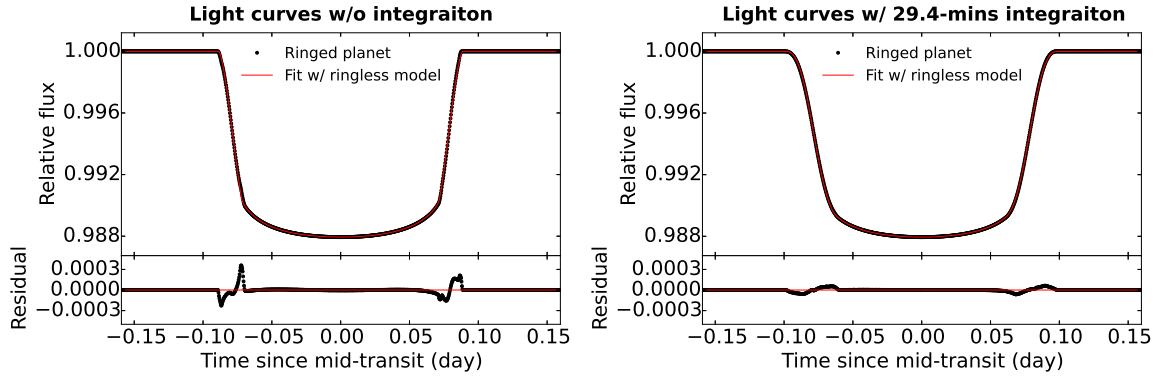
Figure E.2: The same figure as Figure E.1 except for $P = 30$. In the right panel, the residuals are very small. This is because the 29.4-mins integration smears out the evidence of rings.
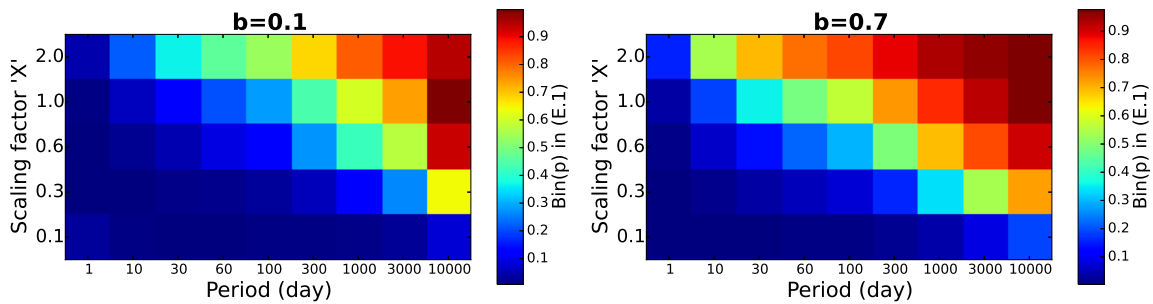
Figure E.3: Effect of 29.4-mins integration on signals of rings with various P and a scaling factor X. Colors show $\mathrm{Bin}(p)$ in Eq.(E.1), which is an indicator of the integration effect. (Left) $b = 0.1$. (Right) $b = 0.7$.
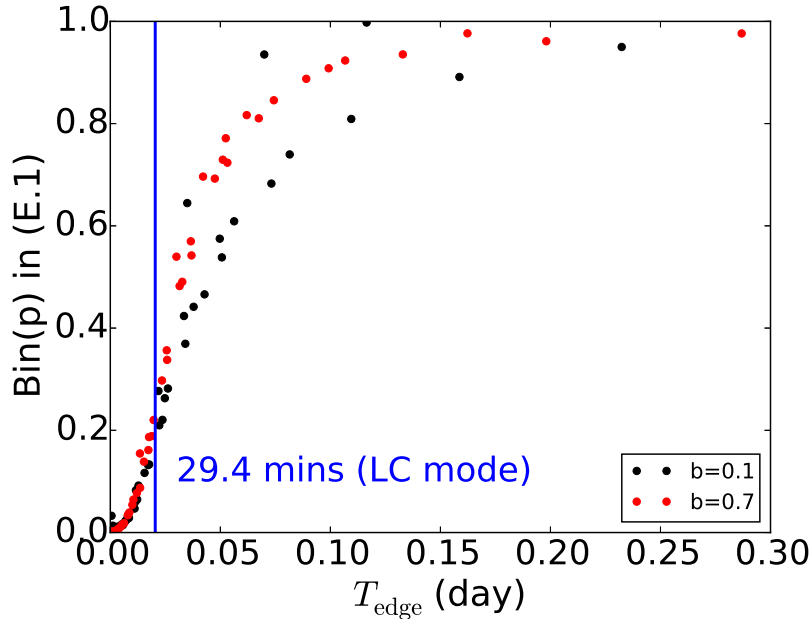
Figure E.4: Time-integration effect and duration around transit edge. The blue line shows 29.4 mins, which corresponds to the integration time in LC mode. The black and red points are results with $b = 0.1$ and $b = 0.7$, respectively.

fitting with a ringless model. These two cases shows little difference. On the other hand, Figure E.2 is the same figure as Figure E.1 except $P = 30$ days. In this case, the residuals in the integrated light curve are relatively small. This is because the change of P from 3000 to 30 days make the transit duration so short that we cannot neglect the integrated effect in the light curve. In addition to P, we also find that if we increase the scale of the system, the signals become large due to the long duration of transit. We summarize the relation of the ring signals ratio and (P, X) in the Figure E.3. In the figure, as we go to the upper right side, the values of P and X become large, and the ring signal ratio tends to be large due to the long duration.

To evaluate the time integration effect in a quantitative way, or to induce the criteria of selecting the suitable targets for the search, we focus on the duration of the transits around edge. Figure E.1 and E.2 show that the signals are concentrated around the edge, and this is generally true in other cases as discussed in Section D. The signals show up-down motion, so the integration operation would smear out these signals. Thus, we naturally expect that when the duration around the edge is relatively long compared with the integration time, the smearing effect would be small. To confirm this, we plot the relation between the duration around the edge and the ring signals ratio in Figure E.4 using the sets of parameters in Table E.1. The blue line in the plot corresponds to the integration time in the long-cadence mode of *Kepler*. We see a clear dependence of signals on the duration around the edge. For example, when the duration around the edge is roughly equal to 29.4 mins, $\text{Bin}(p) \simeq 0.2$. Thus, when the duration around the edge is too short, we cannot detect rings even if there are rings

around the planet. Instead, if the duration around the edge is several times longer than the integration time, the signals of rings would not be erased. So, the duration around the edge is the important criteria for selecting the target objects for the search for rings in LC data.

Bibliography

Arnold, L., & Schneider, J. 2004, A&A, 420, 1153

Ballard, S., Fabrycky, D., Fressin, F., et al. 2011, The Astrophysical Journal, 743, 200

Barnes, J. W., & Fortney, J. J. 2004, ApJ, 616, 1193

Barnes, J. W., Linscott, E., & Shporer, A. 2011, ApJS, 197, 10

Benomar, O., Masuda, K., Shibahashi, H., & Suto, Y. 2014, PASJ, 66, 94

Bond, I. A., Udalski, A., Jaroszyński, M., et al. 2004, The Astrophysical Journal Letters, 606, L155

Borucki, W. J., Koch, D., Basri, G., et al. 2010, Science, 327, 977

Boyajian, T., LaCourse, D., Rappaport, S., et al. 2016, Monthly Notices of the Royal Astronomical Society, 457, 3988

Brogi, M., de Kok, R. J., Albrecht, S., et al. 2016, ApJ, 817, 106

Brown, T. M., Charbonneau, D., Gilliland, R. L., Noyes, R. W., & Burrows, A. 2001, ApJ, 552, 699

Burns, J. A., Lamy, P. L., & Soter, S. 1979, Icarus, 40, 1

Burns, J. A., Showalter, M. R., Hamilton, D. P., et al. 1999, Science, 284, 1146

Butters, O., West, R. G., Anderson, D., et al. 2010, Astronomy & Astrophysics, 520, L10

Cabrera, J., Csizmadia, S., Lehmann, H., et al. 2013, The Astrophysical Journal, 781, 18

Carter, J. A., & Winn, J. N. 2010, ApJ, 716, 850

Catanzarite, J., & Shao, M. 2011, The Astrophysical Journal, 738, 151

Clanton, C., & Gaudi, B. S. 2016, The Astrophysical Journal, 819, 125

Correia, A. C., & Laskar, J. 2009, Icarus, 201, 1

Coughlin, J. L., Mullally, F., Thompson, S. E., et al. 2016, ApJS, 224, 12

Cox, A. N. 2000, Allen's astrophysical quantities

Currie, T., Debes, J., Rodigas, T. J., et al. 2012, The Astrophysical Journal Letters, 760, L32

Cuzzi, J. N., Whizin, A., Hogan, R., et al. 2014, Icarus, 232, 157

Dotter, A., Chaboyer, B., Jevremović, D., et al. 2008, The Astrophysical Journal Supplement Series, 178, 89

Dougherty, M., Esposito, L., & Krimigis, S. 2009, Saturn from Cassini-Huygens (Springer Science & Business Media)

Doyle, L. R., Carter, J. A., Fabrycky, D. C., et al. 2011, Science, 333, 1602

Dressing, C. D., & Charbonneau, D. 2013, The Astrophysical Journal, 767, 95

Dyudina, U. A., Sackett, P. D., Bayliss, D. D. R., et al. 2005, ApJ, 618, 973

Elliot, J. L., Dunham, E., & Mink, D. 1977, Nature

Esposito, L. W. 2002, Reports on Progress in Physics, 65, 1741

Esteves, L. J., De Mooij, E. J., & Jayawardhana, R. 2015, The Astrophysical Journal, 804, 150

Faramaz, V. 2015, arXiv preprint arXiv:1510.03832

Fillius, R. W., McIlwain, C. E., & Mogro-Campero, A. 1975, Science, 188, 465

Gaudi, B. S., Chang, H.-Y., & Han, C. 2003, The Astrophysical Journal, 586, 527

Gehrels, T., Baker, L., Beshore, E., et al. 1980, Science, 207, 434

Hayashi, C. 1981, Progress of Theoretical Physics Supplement, 70, 35

Heising, M. Z., Marcy, G. W., & Schlichting, H. E. 2015, ApJ, 814, 81

Heller, R. 2014, The Astrophysical Journal, 787, 14

Hippke, M. 2015, The Astrophysical Journal, 806, 51

Holman, M. J., Fabrycky, D. C., Ragozzine, D., et al. 2010, science, 330, 51

Huber, D., Chaplin, W. J., Christensen-Dalsgaard, J., et al. 2013, ApJ, 767, 127

Hundertmark, M., Hessman, F., & Dreizler, S. 2009, Astronomy & Astrophysics, 500, 929

Janson, M., Carson, J. C., Lafrenière, D., et al. 2012a, the Astrophysical Journal, 747, 116

Janson, M., Hormuth, F., Bergfors, C., et al. 2012b, The Astrophysical Journal, 754, 44

Kalas, P., Graham, J. R., Fitzgerald, M. P., & Clampin, M. 2013, The Astrophysical Journal, 775, 56

Kalas, P., Graham, J. R., Chiang, E., et al. 2008, Science, 322, 1345

Kenworthy, M., Lacour, S., Kraus, A., et al. 2015, Monthly Notices of the Royal Astronomical Society, 446, 411

Kenworthy, M. A., & Mamajek, E. E. 2015, The Astrophysical Journal, 800, 126

Kenworthy, M. A., & Mamajek, E. E. 2015, ApJ, 800, 126

Kipping, D. M. 2010, MNRAS, 408, 1758

Kipping, D. M. 2010, Monthly Notices of the Royal Astronomical Society, 408, 1758

Kipping, D. M. 2013, MNRAS, 435, 2152

Kipping, D. M. 2014, Monthly Notices of the Royal Astronomical Society, 440, 2164

Kipping, D. M., Bakos, G. Á., Buchhave, L., Nesvornỳ, D., & Schmitt, A. 2012, The Astrophysical Journal, 750, 115

Kipping, D. M., Forgan, D., Hartman, J., et al. 2013a, The Astrophysical Journal, 777, 134

Kipping, D. M., Hartman, J., Buchhave, L. A., et al. 2013b, The Astrophysical Journal, 770, 101

Kipping, D. M., Huang, X., Nesvornỳ, D., et al. 2015a, The Astrophysical Journal Letters, 799, L14

Kipping, D. M., Nesvornỳ, D., Buchhave, L. A., et al. 2014, The Astrophysical Journal, 784, 28

Kipping, D. M., Schmitt, A. R., Huang, X., et al. 2015b, The Astrophysical Journal, 813, 14

Lainey, V., Karatekin, Ö., Desmars, J., et al. 2012, ApJ, 752, 14

Levrard, B., Correia, A., Chabrier, G., et al. 2007, Astronomy & Astrophysics, 462, L5

Lissauer, J. J., Fabrycky, D. C., Ford, E. B., et al. 2011, Nature, 470, 53

Maeder, A. 2009, Physics, Formation and Evolution of Rotating Stars, doi:10.1007/978-3-540-76949-1

Mamajek, E. E., Quillen, A. C., Pecaut, M. J., et al. 2012, The Astronomical Journal, 143, 72

Mandel, K., & Agol, E. 2002, ApJ, 580, L171

Markwardt, C. B. 2009, in Astronomical Society of the Pacific Conference Series, Vol. 411, Astronomical Data Analysis Software and Systems XVIII, ed. D. A. Bohlender, D. Durand, & P. Dowler, 251

Martins, J., Santos, N., Figueira, P., et al. 2015, Astronomy & Astrophysics, 576, A134

Masuda, K. 2014, The Astrophysical Journal, 783, 53

Masuda, K. 2015, ApJ, 805, 28

Mayor, M., & Queloz, D. 1995, A Jupiter-mass companion to a solar-type star

McLaughlin, D. 1924, The Astrophysical Journal, 60

Millholland, S., Wang, S., & Laughlin, G. 2016, The Astrophysical Journal Letters, 823, L7

Morais, M. H., & Correia, A. 2008, Astronomy & Astrophysics, 491, 899

Morton, T. D. 2012, ApJ, 761, 6

—. 2015, VESPA: False positive probabilities calculator, Astrophysics Source Code Library, ascl:1503.011

Murray, C. D., & Correia, A. C. 2010, Exoplanets, 1, 15

Nesvornỳ, D., Kipping, D. M., Buchhave, L. A., et al. 2012, Science, 336, 1133

Ohta, Y., Taruya, A., & Suto, Y. 2005, ApJ, 622, 1118

—. 2009, ApJ, 690, 1

Orosz, J. A., Welsh, W. F., Carter, J. A., et al. 2012, Science, 337, 1511

Owen, T., Danielson, G. E., Cook, A. F., et al. 1979, Nature, 281, 442

Parviainen, H. 2015, MNRAS, 450, 3233

Pojmanski, G. 2002, Acta Astronomica, 52, 397

Queloz, D., Eggenberger, A., Mayor, M., et al. 2000, A&A, 359, L13

Quintana, E. V., Barclay, T., Raymond, S. N., et al. 2014, Science, 344, 277

Rappaport, S., Levine, A., Chiang, E., et al. 2012, The Astrophysical Journal, 752, 1

Rappaport, S., Swift, J., Levine, A., et al. 2014, ApJ, 788, 114

Rieder, S., & Kenworthy, M. A. 2016, arXiv preprint arXiv:1609.08485

Rossiter, R. 1924, The Astrophysical Journal, 60, 15

Sanchis-Ojeda, R., Winn, J. N., Holman, M. J., et al. 2011, ApJ, 733, 127

Santos, N., Martins, J., Boué, G., et al. 2015, Astronomy & Astrophysics, 583, A50

Santos, N. C., Martins, J. H. C., Boué, G., et al. 2015, A&A, 583, A50

Schlichting, H. E., & Chang, P. 2011, ApJ, 734, 117

Schneider, J. 1999, Academie des Sciences Paris Comptes Rendus Serie B Sciences Physiques, 327, 621

Schwarz, H., Ginski, C., de Kok, R. J., et al. 2016, ArXiv e-prints, arXiv:1607.00012

Seager, S., & Mallen-Ornelas, G. 2003, The Astrophysical Journal, 585, 1038

Snellen, I. A. G., Brandl, B. R., de Kok, R. J., et al. 2014, Nature, 509, 63

Uehara, S., Kawahara, H., Masuda, K., Yamada, S., & Aizawa, M. 2016, ApJ, 822, 2

van Werkhoven, T., Kenworthy, M., & Mamajek, E. 2014, Monthly Notices of the Royal Astronomical Society, 441, 2845

Verbiscer, A. J., Skrutskie, M. F., & Hamilton, D. P. 2009, Nature, 461, 1098

Wang, J., Fischer, D. A., Barclay, T., et al. 2015, ApJ, 815, 127

Winn, J. N. 2010, arXiv preprint arXiv:1001.2010

Zhou, Y., Apai, D., Schneider, G. H., Marley, M. S., & Showman, A. P. 2016, ApJ, 818, 176

Zuluaga, J. I., Kipping, D. M., Sucerquia, M., & Alvarado, J. A. 2015, ApJ, 803, L14

Zuluaga, J. I., Kipping, D. M., Sucerquia, M., & Alvarado, J. A. 2015, The Astrophysical Journal Letters, 803, L14